ABSTRACT

Title of Dissertation: ENGINEERING NANOPARTICLES FOR IMPROVED LYMPHATIC DELIVERY AND ELUCIDATING MECHANISMS REGULATING NANOPARTICLE TRANSPORT INTO LYMPHATICS

Jacob McCright
Doctor of Philosophy, 2023

Dissertation Directed by: Assistant Professor Katharina Maisel
Department of Bioengineering

Immune modulatory therapies usually need to be effectively delivered to lymph nodes to enhance therapeutic effectiveness. Lymphatic vessels exist throughout the body and can transport 10 – 250 nm therapeutic nanoparticles to lymph nodes, however, nanoparticle formulations required to maximize this transport, and the mechanisms governing this transport are poorly understood. Here, we probed the effect of surface charge, surface poly(ethylene glycol) (PEG) density, shape, and size on nanoparticle transport across LECs (LECs) and lymph node delivery. Using an established *in-vitro* lymphatic transport model, we found PEGylation improved the transport of 100 and 40 nm nanoparticles across LECs 50-fold compared to non-PEGylated nanoparticles and that transport is maximized when the PEG is in a dense brush conformation corresponding to a high grafting density (Rf/D = 4.9). PEGylating 40 nm nanoparticles improved transport efficiency across LECs 68-fold compared to

unmodified nanoparticles, demonstrating that the addition of PEG improves transport in a size-independent manner. We injected these nanoparticle formulations intradermally into C57Bl/6J mice and found that PEGylated 100 nm and 40 nm nanoparticles accumulate in lymph nodes within 4 hours, while unmodified nanoparticles accumulated minimally. Densely PEGylated nanoparticles also traveled furthest from the injection site. In this thesis, we also determined that nanoparticles are transported via both paracellular and transcellular mechanisms, and that both PEG conformation and nanoparticle size and shape modulates the cellular transport mechanisms. We also expanded our in-vitro lymphatic transport model to model important physiological conditions including transmural flow and found that the presence of this flow increased transport across lymphatic barriers in a shape and mechanism-dependent manner. To further investigate the mechanisms regulating nanoparticle transport, we generated a computational kinetic transport model that was able to quantify the contributions of both paracellular and transcellular transport mechanisms, as well as predict transport efficiency as a function of nanoparticle characteristics including size and surface chemistry. Using transport inhibitors, we can expand our system of equations to describe precise uptake and transport mechanisms, and the relation between nanoparticle formulation and mechanism. This computational model is one of the first to describe transport across lymphatic vessels, and offers some of the first definitions for coefficients used to quantitatively describe nanoparticles transport across LECs (i.e., permeability). Our computational, *in-vitro*, and *in-vivo* results indicate that nanoparticle surface charge, PEG conformation, and size are key criteria for nanoparticle design for effective lymphatic delivery with a dense, neutrally charged coating of PEG maximizing transport across LEC barriers and transport to lymph nodes. Optimizing nanoparticle formulation and surface characteristics, including PEG density, has the potential to enhance immunotherapeutic and vaccine outcomes.

ENGINEERING NANOPARTICLES FOR IMPROVED LYMPHATIC DELIVERY AND ELUCIDATING MECHANISMS REGULATING NANOPARTICLE TRANSPORT INTO LYMPHATICS

By

Jacob Connor McCright

Dissertation submitted to the Faculty of the Graduate School of the
University of Maryland, College Park, in partial fulfillment
of the requirements for the degree of
Doctor of Philosophy
2023

Advisory Committee:
Assistant Professor Katharina Maisel, Chair
Professor Shawn He
Associate Professor Kimberly Stroka
Assistant Professor Margaret Scull
Professor Reza Ghodssi, Dean's Representative

Acknowledgements

I would like to thank the entirety of the mucosal associated immune system engineering and lymphatics lab. I am incredibly grateful for the opportunity to have worked with such a brilliant team of scientists and engineers. I would like to especially thank my advisor, Dr. Katharina Maisel, who has been an incredible mentor, teacher, and advocate over the past years. I am extremely grateful for her guidance, and I am incredibly honored to be the first Ph.D. student to have worked in her lab. I would also like to thank my committee. Their support and insight were invaluable to the development of my thesis work and my development as a scientist.

Table of Contents

List of Figures

1 Introduction

Therapeutic treatments targeting the immune system are becoming more and more prevalent. These treatments include classic vaccines as well as caner immunotherapies. Recently, lymphatic vessels have received significant attention as a potential drug delivery target for immunotherapies. Lymphatics form the body's natural conduit between peripheral tissues and the local draining lymph nodes (**Fig. 1**), where the adaptive immune response is shaped. Delivery of these treatments to the draining lymph nodes, where adaptive immunity is formed, amplifies their efficacy, thus potentially improving their clinical outcomes. Lymph nodes can be indirectly targeted via lymphatic vessels, which exist throughout the entire body and are mainly appreciated for transporting cells, fluid, and particulates from peripheral tissues to the local lymph nodes. Research has shown that lymphatics preferentially transport small particulates between 10 – 200 nm [1-3], the size range of many therapeutically explored nanocarriers, but several key questions remain unanswered: *how do material properties, like shape and surface characteristics, affect trans-endothelial transport of nanoparticles and what are the mechanisms involved in this transport?* When studying lymphatic transport, a unique feature of lymphatic physiology needs to be considered: lymphatic capillaries, where most of the transport from peripheral tissue into lymphatic circulation occurs, are collapsed under steady-state conditions. During movement (homeostasis) and inflammatory processes, interstitial fluid flow pushes fluid into the vessels, effectively expanding them and driving molecules and particulates into the vessel (**Fig. 1** top).

1.1 Approach and Innovation

Lymphatics are largely underappreciated in the field of drug delivery. Growing interest in reaching lymph nodes with immunotherapies has sparked interest in targeting lymphatics with

nanoparticles, but the mechanisms that lymphatics use to transport nanoparticles has remained largely unknown. Additionally, there exists little research on the nanoparticle properties required to cross the lymphatics. The research in this dissertation is some of the first to use rational material design approaches to engineer nanoparticles for improved lymphatic delivery. This research lays the foundation to explore the connection between improved lymphatic transport-mediated lymph node delivery and improved vaccine efficacy.

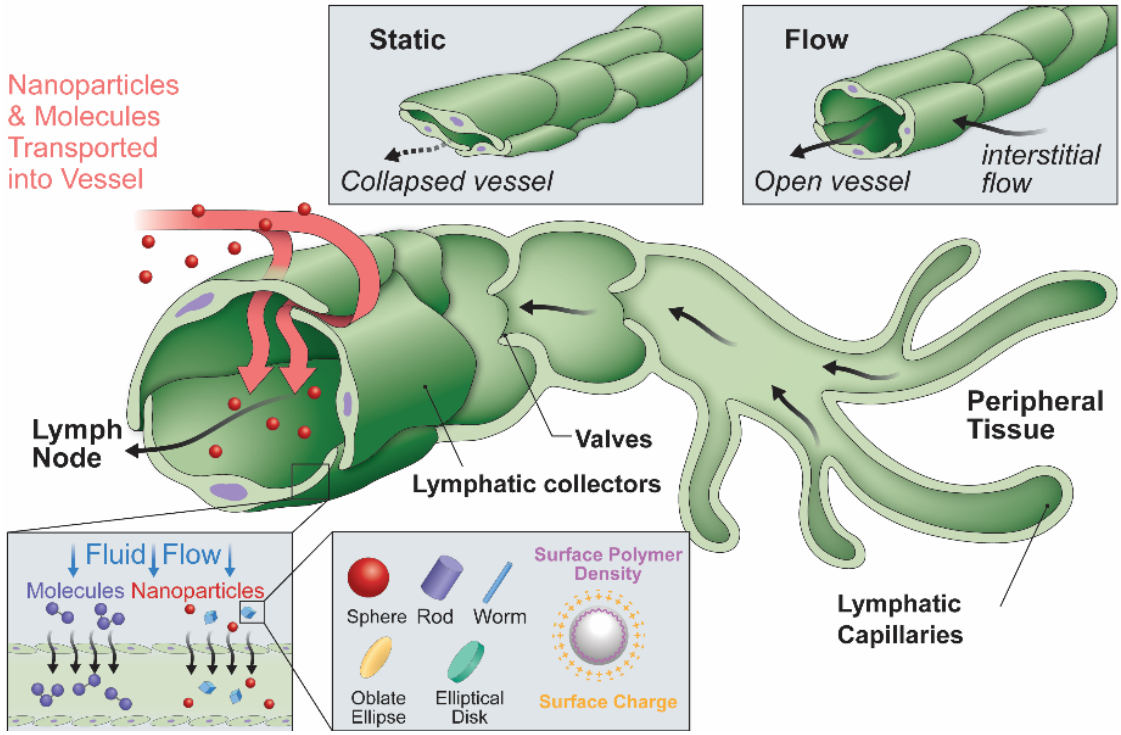

Figure 1 Lymphatics expand from collapsed state due to interstitial flow (top). Lymphatics transport materials from peripheral tissues via capillaries and collecting vessels to the lymph nodes (center). Lymphatics transport materials across the vessel wall via paracellular and transcellular transport routes (bottom).

In this work we explore how parameters such as nanoparticle size, shape, surface charge, and surface polymer density affect transport into lymphatic vessels for lymph node delivery. In this work we used an in-vitro model of lymphatics to probe the effect that these parameters had on crossing lymphatic barriers, and the mechanism that governed transport across these cellular barriers. To better recapitulate in-vivo conditions, features like transmural flow were introduced to the model. We implemented a computational framework to quantitatively describe the kinetics of this transport. With an understanding of nanoparticle formulation required for lymphatic entry, we administered these particles in-vivo to probe if this engineering approach ultimately resulted in improved delivery to lymph node.

1.2 Summary and Dissertation Outline

This dissertation is organized as follows: Chapter 2 provides a literature review on the lymphatic system and lymphatic vessels. This chapter focuses on the transport functions of these vessels and how they have emerged as a promising drug delivery target for improving immunotherapy delivery to lymph nodes. In this chapter I highlight current nanoparticle-based delivery strategies for reaching lymph nodes through lymphatic vessels, as well as ways that lymphatic endothelial cells (LECs) can be utilized as therapeutic targets. Chapter 3 contains a study on formulation strategies to effectively cross lymphatic barriers to reach lymph nodes and reveals the mechanisms governing nanoparticle entry into lymphatic vessels. In this chapter we introduce a nanoparticle system where we can tune the conformation of polyethylene glycol (PEG) on the surface of nanoparticles to probe how surface chemistry affects entry into lymphatics. Using these tools, we were able to demonstrate that a dense coating of PEG was required for entry into lymphatics and delivery to lymph nodes. In this chapter we also demonstrated that both transcellular and paracellular transport are required for transport into lymphatics, and that the cellular mechanisms of transport are

dependent on formulation. In chapter 4 we explore the kinetics of nanoparticle transport into lymphatic vessels, investigating how nanoparticle formulation affects transport pathways using a quantitative approach. In this chapter we generated a three-compartment model of the lymphatic endothelium barrier and generated a system of differential equations describing the transport of nanoparticles using both transcellular and paracellular mechanisms. In this chapter we calculate some of the first kinetic data, including rate constants, to describe how lymphatics regulate transport into vessels. Additionally, we also highlighted an interesting phenomenon where nanoparticle transport across lymphatics is characterized by a rapid uptake and release of nanoparticles at the basolateral interface. Chapter 5 further explores parameters regulating lymphatic transport, mainly how the adsorption of protein and transmural flow affect nanoparticle transport into lymphatics. In this chapter we also explored how nanoparticle shape influences transport into lymphatics and the mechanisms that govern transport into lymphatics. In this chapter we were able to generate rod-shaped nanoparticles and impart the densely PEGylated surface chemistry that was identified in Chapter 3 as critical in facilitating transport into lymphatics. Using these rod-shaped nanoparticles, we determined that the presence of modeled transmural flow was key in facilitating the transport of rod nanoparticles across lymphatic barriers. We were also able to show that rod shaped nanoparticles could effectively reach lymph nodes as well as enter the cortex of lymph nodes. Chapter 6 summarizes the conclusions of this dissertation and outlines the ongoing and potential future work on investigating lymphatic drug delivery. In the appendices of this dissertation, I include work on developing gastrointestinal models that incorporate physiological relevant mucus. This work is included in the dissertation as it outlines a promising application for nanoparticles that can effectively enter lymphatics. The GI tract contains a high density of lymphoid tissues in the body and a high density of lymphatic vessels. This fact,

alongside the fact that oral administration is often the most desirable delivery route, makes engineering a nanoparticle that can cross both GI and lymphatic barriers a promising strategy to ultimately producing immunotherapies that are effective and can be taken orally.

Contributions to Engineering

In this thesis we generated 1) a nanoparticle system where we able to tune the surface chemistry precisely to probe lymphatic transport efficiency, 2) incorporated these nanoparticles into a computational model of transport into lymphatic to generate quantitative parameters describing transport efficiency with respect to formulation, and 3) applied successful surface modification parameters to nanoparticles of different shapes and sizes. These engineering advances can lead to improved immunotherapies, where improved lymphatic delivery and delivery to lymph nodes is key in improving outcomes.

Contributions to Science

Completion of this thesis has resulted in the following contributions to science: 1) we identified that a dense, neutral, coating of polyethylene glycol (PEG) optimizes transport into lymphatics, 2) we demonstrated that the cellular mechanisms governing transport into lymphatics are formulation and size dependent, and 3) we identified some of the first quantitative transport parameters to describe nanoparticle entry into lymphatics. We also performed some of the first experiments examining how nanoparticle shape effects transport into lymphatics, and demonstrated that under physiological conditions, rod shaped nanoparticles can effectively reach lymph nodes. Completion of these experiments has helped characterize how the lymphatics serve as a barrier to drug delivery, and identified ways that these can be overcome.

2 Targeting Lymphatics for Nanoparticle Drug Delivery

This Chapter is reproduced with permission from:

McCright, J.; Naiknavare, R.; Yarmovsky, J.; Maisel, K. Targeting Lymphatics for Nanoparticle Drug Delivery. *Frontiers in Pharmacology* 2022, 13

2.1 Introduction

Lymphatic vessels exist throughout the body and are mainly appreciated for transporting extracellular fluid and solutes including antigens, cells, extracellular vesicles, and particulates to draining lymph nodes and eventually into systemic circulation. Lymphatic vessels have traditionally been thought of as passive transporters; however, recent studies have found that lymphatic vessels actively transport materials and also play a key role in modulating immunity. The natural transport functions of lymphatic vessels have been used to deliver immunomodulatory therapies to lymph nodes to shape immune responses. This can be achieved using nanomaterial formulations that preferentially drain into lymphatic vessels. In this review we provide an overview of lymphatic vessel function and physiology, highlight therapeutic formulations developed to target lymphatic vessels, and thus the downstream lymph nodes to enhance immunotherapies, and explore how directly targeting lymphatic immune functions modulate immunity.

2.2 Lymphatic vessel physiology

2.2.1 Initial and collecting lymphatics

Initial lymphatics, also known as lymphatic capillaries, are the entry point for lymph and the initial pathway into the lymphatics system. Made up of vessels ranging from 10-60 μm, initial lymphatics form a network in interstitial spaces of tissues (**Fig 2A [4]**) [5]. The lymphatic capillary walls are made up of single-layered cells that overlap in some areas, giving the appearance of one-way flaps [6], or microvalves [7]. Although initial lymphatics are blind-ended, it is postulated that the microvalves embedded within their capillary walls allow for permeation of larger molecules, such as proteins and particulates [8]. The microvalves of the capillaries connect directly to surrounding tissues via thin, elastic fibers. These fibers only connect to the external wall of the initial lymphatics, leaving the internal surface unattached and flexible [5]. Initial lymphatics transport materials toward collecting lymphatics or collecting vessels. Collecting lymphatics have been classified as two different types: afferent vessels that transport lymph from peripheral tissue to the lymph nodes, and efferent vessels that transport lymph away from the lymph node to systemic circulation (**Fig 2B-C**) [9]. Typically, afferent lymph consists of red blood cells, monocytes, and antigen-presenting dendritic cells [10]. Dendritic cells enter the afferent vessels by leaking through peripheral tissue and blood capillaries into the interstitial space. From there, they can migrate into initial lymphatics. During inflammation, dendritic cells can be recruited to the lymphatic vessels by lymphatic endothelial cells (LECs) through increased production of chemokines including CCL19 [11], CCL21, and CCL22 [12]. These chemokines are ligands for CCR7, which recruits T and dendritic cells to the lymphoid tissue. They are also important in thymocyte development and secondary lymphoid organogenesis [13]. The resulting increase of dendritic cells within the lymph nodes promotes lymph node expansion and additional secretion of chemokines by other

stromal cells recruits lymphocytes to the lymph nodes [12]. Efferent vessels transport lymph from the lymph nodes to the large vessels, which eventually return the lymph back into blood circulation. Efferent lymphatic vessels carry lymphocytes, in particular a high proportion of CD4+ T cells and B cells, compared to CD8+ and γδ T cells [14]. Efferent lymphatic vessels converge and carry material towards the thoracic duct and the right lymphatic trunk, then drain material into venous circulation via four lymphovenous valves where the subclavian and jugular veins meet (**Fig 2D**) [4, 15].

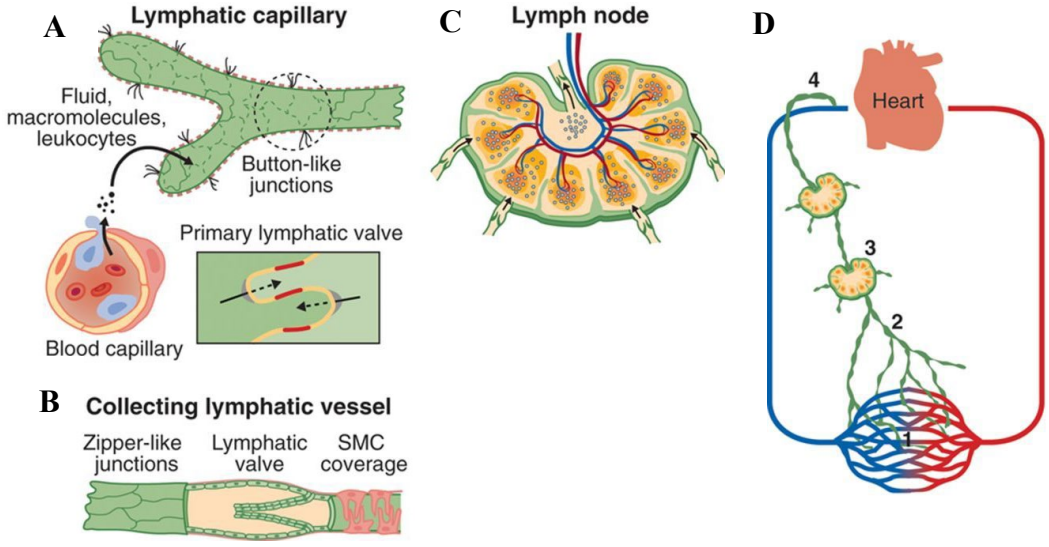

Figure 2 *Schematic of Lymphatic Vessel Transport Properties* **A)** Discontinuous basement membrane (red dashed line) and button junctions (dotted lines) allow for lymphatic capillaries to absorb interstitial solutes, macromolecules, and immune cells. **B)** Collecting vessels contain zipper-like junctions (continuous lines) and unidirectional valves. **C)** Schematic of lymph node with multiple afferent and a single efferent vessel. **D)** Lymphatic vascular system consists of (1) lymphatic capillaries, (2) collecting lymphatic vessels, (3) lymph nodes, and (4) the thoracic duct and right lymphatic trunk. Image adapted from (Aspelund)

2.2.2 Barrier functions of lymphatic vessels

Lymphatic vessels form a barrier between the interstitial space of tissues and lymph within the lumen of the vessels. Lymphatics are semipermeable and only allow unidirectional flow. Initial and collecting lymphatics have different functions, and the unique structures of the vessels enable those functions. Initial lymphatic vessels are composed of LECs surrounded by an incomplete basement membrane [16]. Initial vessels facilitate the formation of lymph, so they require high permeability to allow for the transport of fluid, macromolecules, lipids, and immune cells away from the interstitial space of tissues. Transport into lymphatics occurs when local fluid accumulation and tissue stress result in higher pressure in the interstitial fluid than the lumen of lymphatic vessels. When this occurs, lymph is transported into vessels through paracellular and transcellular routes [17]. Conversely, if pressure is higher inside the lymphatic vessels, endothelial cells adhere more closely, preventing lymph from flowing back into interstitial fluid. Collecting vessels are larger vessels that transport lymph collected form several initial vessels to the lymph node, requiring lower permeability and a stronger barrier to prevent lymph leakage. Collecting vessels are surrounded by a continuous basement membrane and perivascular cells. Shear stress within collecting vessels causes a tightening of the lymphatic endothelial barrier through cell junction stabilization, and thus enhances barrier functions [16, 18]. This is likely part of a mechanism to prevent excessive leakage and optimize lymph flow. While shear stress results in increased barrier function, inflammation generally has the opposite effect. During inflammation, upregulation of inflammatory cytokines can lead to increased LEC permeability within initial lymphatics [19]. This occurs through disruption of cell-cell junctions and contraction of the actin/myosin cytoskeleton within LECs [20]. Impaired lymphatic endothelial barrier function can result in several pathological conditions. For instance, edema develops if gaps between endothelial

cells are too large [5]. Furthermore, in lymphedema, lymphatic vessels experience high levels of shear stress and stretch and adapt to these conditions by increasing transport [21].

2.2.3 Cell-cell junctions

The junctions of lymphatic vessels are largely composed of the adherens junction proteins VE-cadherin, β-catenin and p120-catenin, and the tight junction proteins occludin, claudin-5 and zonulin-1 (ZO-1), junctional adhesion molecule-A (JAM-A), and endothelial cell-selective adhesion molecule (ESAM) [22]. Despite the similarities in composition, junctions in initial and collecting lymphatic vessels differ greatly in morphology and function [23]. Initial lymphatic vessels have discontinuous junctions, also referred to as button-like. Button junctions are characterized by discontinuous segments of VE-cadherin at the border of endothelial cells [6]. They are formed by the overlap of the membranes of endothelial cells, which create flap-like mini-valves [7]. In normal conditions these flaps are closed and prevent flow from the lumen into the interstitial space. The tips of the flaps have filaments that attach the endothelial cells to the extracellular matrix. In the presence of a pressure gradient from the interstitial space to the lumen, these filaments pull on the flaps, creating a separation between the cells that allows fluids and solutes to enter lymphatic vessels [24]. An advantage of this structure is that drainage into lymphatics can occur without the dissolution of endothelial cell junctions, maintaining vessel integrity [10]. Since collecting lymphatic vessels do not exchange materials with surrounding tissue, they have different types of junctions called zipper-like junctions, which provide a strong barrier between the vessel and its surroundings through continuous localization of VE-cadherin at the LEC borders [25]. During inflammation, the alteration of both button- and zipper-like junctions can increase lymphatic permeability [26].

2.2.4 Fluid homeostasis

Regulating fluid balance is crucial in bodily function [27]. Most plasma produced by the body is returned to the bloodstream by veins. However, the excess fluid that is not returned, or leaks through the blood capillaries, remains behind and accumulates in the interstitial spaces between tissues. One of the main roles of the lymphatic system is to maintain balance by absorbing that excess fluid, known as lymph, and returning it back to systemic circulation [28]. Fluid moves unilaterally through the lymphatic system, first absorbed by the initial lymphatics, transported via collecting lymphatics across lymph nodes, and eventually enters either the right lymphatic duct or the thoracic duct, near the base of the neck [29]. Without proper lymphatic drainage, the buildup of fluid in the interstitial spaces can potentially cause life-threatening conditions [30]. One such example is lymphedema, which occurs when excess interstitial fluid builds up in tissues, leading to distension, inflammation, swelling of the limbs, head, and neck, and an increase in fatty tissue significantly affecting quality of life [31-33].

2.3 Targeting lymphatics for drug delivery

Immunotherapies, including vaccines, have been extremely promising for curing diseases including cancer, chronic inflammation, and transplantation. Delivery of these treatments to the draining lymph nodes, where adaptive immunity is formed, amplifies their efficacy, thus potentially improving their clinical outcomes. One strategy to target lymph nodes indirectly from peripheral tissues via, e.g., intramuscular or subcutaneous injection, is to use lymphatic transport functions. Research from the last decade has identified that nanomaterials between 10 – 250 nm in diameter [34], and up to 1 micron in some studies, can also be taken up by LECs through macropinocytosis [35]. In the gastrointestinal tract, lymphatics also play a special role in lipid

absorption: lipids are taken up by lymphatic vessels via chylomicrons, small lipid vesicles into which dietary lipids are packaged by enterocytes. This can be taken advantage of for drug delivery, as targeting gastrointestinal lymphatics circumvents therapeutics from being digested via hepatic first pass metabolism. In this section we describe some of the various nanomaterial-based strategies for targeting lymph nodes via lymphatic vessels, as well as lipid-based strategies to target gastrointestinal lymphatics.

2.3.1 Nanomaterial-based lymphatic targeting

Nanoparticle size was one of the first parameters investigated with respect to optimizing lymphatic drug delivery. A study from the Swartz lab showed that fluorescent 20 – 100 nm, PEG-stabilized poly(propylene sulfide) nanoparticles accumulated within LNs after tail injection. Importantly, they were able to visualize the lymphatic network of the mice using fluorescent nanoparticles [36]. This visualization was also dependent on nanoparticle size, smaller 20 nm nanoparticles were present in higher quantities within lymphatic vessels compared to larger 100 nm nanoparticles. When lymph nodes were recovered, the 20 – 45 nm nanoparticles were found co-localized with $MHCII^+$ antigen-presenting cells. Additionally, when these nanoparticles were conjugated to model antigen ovalbumin, they found that the humoral and cellular immune response in mice was generated in a size-dependent manner. Nakamura et al. also observed a similar phenomenon when subcutaneously injecting pH-sensitive lipid nanoparticles in inguinal regions of mice. They found that the 30 nm formulations were transported into lymph nodes and taken up by $CD8^+$ dendritic cells more effectively than 100 nm and 200 nm formulations of the solid lipid nanoparticles [1]. Recent work by our group has also found that polyethylene glycol (PEG)-coated 40 nm nanoparticles were able to cross lymphatic barriers more efficiently than 100 nm PEG-coated nanoparticles [37].

The size range required for targeting lymphatic vessels is now well-established, so many studies have turned to understanding the surface chemistry requirements necessary for lymphatic targeting. Varypataki compared anionic poly(lactic-co-glycolic) (PLGA) nanoparticles and cationic liposomes [38]. They found that the 180 nm cationic liposome vaccine formulations reached lymph nodes and were more effective in elucidating *in-vivo* immune response after subcutaneous injection compared to the 350 nm PLGA nanoparticles. This improved potency and delivery of cationic liposome vaccines is likely to be at least in part due to the smaller size of the liposome formulations compared to the PLGA formulations. A study from Nishimoto et al. examined the effect that charge had on dendrimer delivery to lymph nodes following intradermal injection [39]. They found that anionic dendrimers accumulated within lymph nodes, with phosphate-terminal dendrimers recognized by the macrophages, dendritic cells, and B cells in the lymph node, whereas other anionic dendrimers were not. However, all formulated dendrimers were <10 nm in diameter, suggesting that they are outside the range of sizes for optimum lymphatic transport [40]. Research from Kaminskas et al. demonstrated that PEGylation of poly-l-lysine dendrimers enhanced their transport to the LNs after subcutaneous injection in murine models [41]. However, similar to the study by Varypataki, there were significant size differences in the compared formulations. Notably, non-PEGylated dendrimers were under 10 nm in size, falling outside of the range identified for optimal lymphatic transport [40].

Early studies from Moghimi et al. demonstrated that coating nanoparticles with polyethylene glycol (PEG)-polypropylene oxide copolymers can enhance LN accumulation of nanoparticles after intradermal administration in mice [42]. De Koker et al. also demonstrated that modifying nanoparticle surface chemistry can be engineered to leverage lymphatic transport [43]. They were able to demonstrate that coating 200 nm mesoporous silica nanoparticles with PEG improved LN

accumulation of nanoparticles after 12 and 48 hours, compared to uncoated 200 nm silica nanoparticles. They were also able to demonstrate that PEG-coated nanoparticles were more effective at priming antigen-specific T cells [43]. Rao et al. also found that 50, 100, and 200 nm PEG-coated nanoparticles accumulated more in the LNs after subcutaneous injection compared to uncoated PLGA nanoparticles of the same size, suggesting that hydrophilicity is crucial to maximize lymphatic transport of nanoparticles [44]. However, in this study, the surface potential of PEGylated nanoparticles was only -36.1 ± 14.6 mV, suggesting that the PEG coating was not very dense. Zhang et al. also demonstrated that the addition of PEG can improve liposome delivery to lymphatic vessels and lymph nodes [45]. They demonstrated that the addition of 2 kDa PEG to the surface of 250 nm DOTAP liposomes expedited lymphatic transport and improved LN retention compared to DOTAP liposomes without PEG. Recent work from our group has closely examined the role that surface chemistry plays in lymphatic permeability and transport. Using model 40 and 100 nm polystyrene-core nanoparticles, we found that the addition of PEG improved lymphatic permeability within a transwell lymphatic model compared to uncoated polystyrene nanoparticles. Additionally, we observed that increasing PEG density on the surface of the nanoparticles optimized transport across LEC barriers. Indeed, densely PEGylated nanoparticles were found to accumulate in draining lymph nodes within 4 hours after intradermal injection. In addition to identifying optimum surface characteristics for lymphatic delivery, we also provided some of the first insight on the transport mechanisms involved in the transport of nanoparticles across lymphatic barriers. We found that both paracellular and transcellular transport mechanisms were key in crossing lymphatic barriers, with LECs relying on clathrin-mediated endocytosis to mediate transport of PEGylated nanoparticles [37].

Other studies have examined how nanoparticle formulation influence where they accumulate within targeted LNs. A study from Zeng et al. demonstrated that positively charged 30 nm polyethyleneimine-stearic acid micelles preferentially accumulated in draining LNs compared to free antigen [46]. They found that the nanoparticles were in the medulla and paracortex of lymph nodes, where T cells reside, following subcutaneous injection. Additionally, immunofluorescence imaging of LN sections showed significant nanoparticle accumulation around the border of the LN, within the subcapsular sinus. This result is consistent with reports that the conduit system within LNs is incapable of transporting material greater than 70 kDa from peripheral regions of the LN to central regions [47]. In addition to demonstrating nanoparticles were able to effectively reach LNs, they also showed that the nanoparticle-based cancer vaccine was more effective in inhibiting tumor growth compared to free antigen.

Work from the Thomas group has provided some of the most cutting-edge technologies for delivering nanoparticles to lymph nodes via lymphatic vessels. Recently Schudel et al. generated a two-stage system inspired by the way particulate antigen is processed by the immune system. An outer stage comprised of F127 pluronic-containing PEG utilizes lymphatic transport to reach draining lymph nodes while protecting the cargo from systemic exposure. The second stage utilizes OND-thiol linkage chemistry programmed to release small molecule cargo when exposed to lymph. They were able to demonstrate that this technology allows for precise delivery of small molecules to lymph node – resident dendritic cells as well as controlled release through tuning of the degradation kinetics of the thiol bond [48]. Additional studies from the group can be highlighted in a recent review from the group [49].

2.3.2 Lipid-Based Targeting of Lymphatics

Lymphatics are the key conduit for transporting dietary lipids from the gut into systemic circulation. Lipids typically enter enterocytes within the gastrointestinal tract through a receptor-mediated endocytosis or micropinocytosis [50, 51]. In the gastrointestinal epithelium, they are packaged into chylomicrons and exocytosed from the basolateral side of the enterocyte cell into the lamina propria, where chylomicrons effectively enter initial lymphatic vessels. Chylomicrons eventually enter systemic circulation through the thoracic duct that drains into the subclavian vein. The chylomicron processing pathway provides multiple unique opportunities for engineering drug delivery strategies as it signifies a route to reach lymph nodes to potentiate immunotherapies, as well as a way to achieve systemic delivery through an orally administered drug while simultaneously bypassing hepatic first pass metabolism.

To best utilize the chylomicron processing pathway for lymphatic delivery, therapeutics can be formulated as a prodrug consisting of a cleavable lipid component that triggers this innate transport pathway. Several groups have published extensively on how triglyceride-, and other fatty acid-, mimicking lipid formulations are able to improve the delivery of a variety of drugs to lymphatic vessels and gut-draining lymph nodes after oral administration [52-55]. Indeed, the researchers' development of a lymphatic-cannulation technique has allowed them to directly observe the transport of lymph from the small intestine through lymphatic vessels and lymph nodes that converge at the superior mesenteric lymph duct [56]. This technique was also applied to examine the fate of subcutaneously administered, high-density lipoprotein nanoparticles (HDLs), finding that HDLs preferentially drained via lymphatic vessels, as opposed to blood vessels, and that LN retention of HDL was positively correlated to increasing the negative charge of HDL [57]. For

more detailed descriptions of such prodrug formulations, we direct readers to this recent review [58].

More recently, several groups have used the chylomicron pathway to delivery particulate cargo to intestinal lymphatics. Mao et al. generated 100-120 nm mesoporous silica nanoparticles that were coated with diglycerides to trigger chylomicron processing [59]. They demonstrated that resident lipases within the gastrointestinal lumen cleaved the fats on the surface of the nanoparticle, prompting uptake and processing into chylomicrons, and further transport into lymphatic vessels. To confirm that the nanoparticles were being processed as chylomicrons, they probed the intracellular pathways using a combination of transport inhibitors and confirmed how chylomicron processing was necessary for transcellular transport of the nanoparticle. They also confirmed that these chylomicron-like nanoparticles were transported to the lymph nodes via lymphatic transport.

The Bae lab has used a similar strategy of promoting epithelial uptake of nanoparticles via bile-acid transporter-mediated cellular uptake, followed by chylomicron formation and transport into intestinal lymphatics. The group showed that 100 nm cationic solid lipid nanoparticles and carboxylate polystyrene nanoparticles coated with bile acids displayed significantly enhanced average oral bioavailability (47%) with sustained absorption in rats compared to uncoated nanoparticles [60-62]. Baek et al. also used a similar strategy to delivery curcumin to the lymphatics [63]. Solid lipid nanoparticles ranging from 150 – 250 nm were loaded with curcumin and administered orally. To prevent encapsulated drug release due to low pH conditions of the stomach, they coated their nanoparticle with chitosan, which also improved nanoparticle uptake into enterocytes. They found that lymphatic uptake and oral bioavailability of chitosan-coated solid lipid nanoparticles was 6.3-fold and 9.5-fold higher than that of curcumin solution, respectively.

A study by Lee et al. also examined how the addition of prodrug on the surface of their orally administered nanoparticle formulation could promote delivery to lymphatic vessels [53]. Using a model lipophilic drug, Orilstat, they formulated emulsions containing medium-chain fatty acids, long-chain fatty acids, or long-chain triglycerides. Orilstat was found in the highest concentration in lymphatic vessels when coated with the long-chain fatty acids compared to the short-chain fatty acids and triglycerides. Drug concentration in the lymph peaked 2-3 hours after oral administration of the drug. Increasing the presence of fatty acids on the surface of the emulsion was also found to improve nanoparticle transport across intestinal epithelial barriers and into lymphatic vessels.

Recently, Kochappan et al. formulated mycophenolic acid (MPA) to be attached to triglycerides. They hypothesized that the attached fatty acid would help the immunomodulatory drug reach lymphatic vessels and lymph nodes through the chylomicron processing pathway [55]. Intraduodenal administration of the MPA-fatty acid conjugate improved drug concentration within lymph compared to MPA and MPA co-delivered (not conjugated). When examining MPA concentration within the lymph nodes, they found that the MPA-fatty acid conjugate resulted in a 20-fold higher concentration compared to MPA delivered alone.

2.4 LECs as therapeutic targets

In addition to transport and fluid regulation functions, the lymphatic endothelium plays a key role in immunity through interactions with immune cells. LECs are located throughout the entire body and produce key chemokines and adhesion molecules that help lymphatic vessels influence immunity.

2.4.1 LEC-mediated immunity

Lymphatics are the highway for immune cells that enter peripheral lymphatic vessels within tissues and migrate to the local lymph nodes. Lymphatic vessels are key for the migration of dendritic cells, neutrophils, monocytes, and lymphocytes, including B and T cells, many of which migrate via the CCL21-CCR7 axis [64, 65]. CCR7 is key in not only facilitating immune cell migration to the lymph nodes, but in directing dendritic cells to other tissues including the lamina propria, lungs, and skin. An interesting effect of CCR7 presence within lymphatic vessels is that CCR7-dependent dendritic cell migration decreases lymphatic permeability, indicating cross talk between the lymphatic network and immune cells [66, 67]. Additionally, dendritic cells preferentially enter lymphatics at sites where the CCL21 gradient is highest, suggesting that CL21 directly regulates entry into lymphatics, a finding that is supported by the fact that intravital microscopy has revealed that CCL21 gradients also enhance dendritic cell migration within lymphatic vessels. CCL21 secreted by LECs also regulates the homing of naïve T cells from distant peripheral tissues to lymph nodes.

While researchers have focused on lymphocyte and antigen presentation cell migration via lymphatics, more recent data demonstrates that neutrophils, one of the first immune cells to be recruited to a site of infection or injury, can also enter lymphatic vessels and migrate to the lymph nodes from these sites of inflammation [68-70]. The significance of this migration is not fully understood. Studies have indicated that there is a correlation between inflammation and neutrophil concentration in afferent lymph. Further discussion on the interplay between migratory immune cells and lymphatic vessels can be found here [66].

In addition to regulating dendritic migration through the CCL21-CCR7 axis, LECs can interact directly with dendritic cells, which can impair dendritic cell maturation. Researchers have found that LECs were able to prevent dendritic cell maturation through ICAM-1/Mac-1 contact-dependent interactions, as well as through anti-inflammatory prostacyclin synthesis and TGF-β secretion [71]. Research has also shown that LECs have a key part in regulating T cell activation through the secretion of nitric oxide within the lymph nodes in the presence of inflammation [72]. One of the more interesting methods in which LECs can modulate immune responses is through the transfer of antigen to professional antigen-presenting cells, CD4+ cells, and CD8+ cells [73]. Indeed, Tamburini et al. demonstrated that LEC proliferation coupled with antigen capture leads to prolonged antigen expression within LECs, increasing IFNγ and IL-2 production, and enhancing protection against infections. While the delivery of MHCI and MHCII-restricted antigens resulted in dysfunctional activation of CD8+ and CD4+ T cell responses, it is unclear what role the contribution of LEC antigen-presentation played.

2.4.2 Targeting Lymphatic Vessels for Immunomodulation

With a key role in immunomodulation, lymphatic vessels themselves have emerged as an attractive therapeutic target. One of the key targets for potentially targeting lymphatic vessels themselves is targeting lymphatic-specific receptors, such as VEGFR-3 or Lyve-1. VEGFR-3 is part of the family of vascular endothelial growth factor receptors and is mainly appreciated for promoting lymphangiogenesis [74]. Lyve-1, or lymphatic vessel endothelial hyaluronan receptor 1, is a common, integral membrane protein used for identifying LECs, but can also be found in liver blood sinusoids, embryonic blood vessels, and certain subsets of macrophages [75-77]. Guo and colleagues targeted LECs via Lyve-1 *in vitro*, by using Lyve-1-binding PEG to ultrasmall superparamagnetic iron oxide nanoparticles as a potential MRI contrast agent [78]. Dashkevich et

al. were able to leverage this VEGFR-3 targeting to prevent cardiac allograft rejection. They demonstrated that inhibition of VEGFR-3 led to reduced CCL21 production [79]. They found that this reduced CCL21 production did not affect lymphangiogenesis within the graft but did result in lower concentrations of CD8+ T cells within the graft. In an additional experiment, they demonstrated that treatment with a neutralizing monoclonal VEGFR-3 antibody reduced arteriosclerosis, the number of activated lymphatic vessels expressing VEGFR-3 and CCL21, and graft-infiltrating CD4+ T cells in chronically rejecting mouse cardiac allografts. Blocking the interaction between VEGFR-3 on lymphatic vessels and VEGF-C produced by tumors can be a form of tumor suppression through prevention of tumor lymphangiogenesis, which contributes to metastasis and tumor growth [80]. Maisel et al. have demonstrated that VEGFR-3 activation in allergic responses can initiate acute inflammatory response and regulate the adaptive immune response. They found that blocking VEGFR-3 leads to less inflammation, reduced innate and T-cell numbers, and reduced inflammatory chemokine levels initially. However, VEGFR-3 blocking also significantly enhanced memory T cell responses to allergens, suggesting that targeting lymphangiogenesis in inflammatory conditions may be a double-edged sword [81]. In cancer, studies have demonstrated that treatment with VEGF-C, the ligand for VEGFR-3, can improve immunotherapy treatments in melanoma [82]. Fankhauser et al. were able to demonstrate that while VEGF-C can promote angiogenesis, and subsequent metastasis, it also potentiates immunotherapy by attracting naïve T cells [83]. The group also demonstrated that positive response to immunotherapy in patients can be correlated with expression of lymphatic-related markers within the tumors, suggesting that lymphatics have a role in enhancing tumor immunotherapies.

2.5 Outlook

Lymphatic vessels have become a tissue of interest in therapeutic design in large part for their role in transport as well as immunomodulation. Lymphatic vessels can effectively transport immunomodulatory therapies after non-invasive oral or intradermal/subcutaneous delivery, which in turn can improve the efficacy of immunomodulatory therapies that need to reach lymph nodes for improved therapeutic efficacy. While we have scratched the surface of how to target lymphatic transport, we still have an incomplete understanding of lymphatic functions. Continued exploration of how targeting lymphatic functions can serve as a therapeutic target will lead to new discoveries and advances that can further enhance immune modulatory therapeutics and lead to new treatments.

3 Nanoparticles with Dense Poly(ethylene glycol) Coatings with Near Neutral Charge are Maximally Transported Across Lymphatics and to the Lymph Nodes

Chapter reproduced with permission from:

McCright, J., et al., *Nanoparticles with dense poly(ethylene glycol) coatings with near neutral charge are maximally transported across lymphatics and to the lymph nodes.* Acta Biomaterialia, 2022. **145**: p. 146-158.

3.1 Introduction

Lymphatic vessels exist throughout the entire body and are known for transporting cells, fluid, and particulates from peripheral tissues to the local draining lymph nodes (LNs), where the adaptive immune response is formed [84]. In recent years, lymphatics have received increasing attention as potential drug delivery targets to transport immune modulatory therapies to the LNs without requiring direct injections. Delivering immunotherapies, including vaccines, to the LNs has been shown to potentiate their therapeutic effects, particularly crucial as efficacy of many immunotherapies still requires improvement. Recent studies have demonstrated that nanoparticles between 10 - 250 nm in diameter are transported preferentially via lymphatic vessels from peripheral tissues to LNs, highlighting that the transport functions of lymphatics can be taken advantage of for drug delivery [2, 34, 38, 85].

While the size required for lymphatic entry is well established, conflicting data about the nanoparticle surface chemistry required to maximize lymphatic transport exist. Early studies on how size affects nanoparticle delivery to LNs demonstrated that 20 nm poly(ethylene glycol) (PEG)-stabilized nanoparticles were able to reach, and remain within, lymph node-resident dendritic cells compared to larger 100 nm nanoparticles [2]. Another study on the effects of

nanoparticle size found that large 500 - 2000 nm, virus-like nanoparticles were taken up by skin-resident dendritic cells following intradermal injection, while smaller 50 - 200 nm virus-like nanoparticles were trafficked to the LNs via lymphatic drainage [85]. Combined, these initial studies provide evidence that the optimum nanoparticle size to reach LNs through lymphatic transport is within the 10 - 250 nm range.

Early studies demonstrated that coating nanoparticles with certain poloxamines, PEG-polypropylene oxide copolymers, can enhance LN accumulation of nanoparticles after intradermal administration. It was hypothesized that PEG chain length may contribute to some poloxamines enhancing nanoparticle transport more than others [42]. One study comparing cationic liposomes and anionic poly(lactic-co-glycolic acid) (PLGA) nanoparticles demonstrated that cationic liposomes accumulate to a greater extent in the LN after subcutaneous injection, compared to anionic PLGA nanoparticles [38]. However, there is a large size discrepancy between the two systems: cationic 180 nm liposomes were well within the lymphatic targeting size range, while anionic 350 nm PLGA nanoparticles were likely too large to preferentially enter lymphatic vessels. Another study demonstrated that positively charged 30 nm polyethyleneimine-stearic acid micelles preferentially accumulated in draining LNs compared to free antigen [46]. Another group demonstrated that coating 200 nm poly(methacrylate) nanoparticles with PEG markedly improved LN accumulation of nanoparticles after 12 and 48 hours [43]. Researchers also found that 50, 100, and 200 nm PEG-coated nanoparticles accumulated more in the LNs after subcutaneous injection compared to uncoated PLGA nanoparticles of the same size, suggesting that hydrophilicity is vital to maximize lymphatic transport of nanoparticles [44]. However, in this study, the surface potential of PEGylated nanoparticles was only -36.1 ± 14.6 mV, suggesting that the PEG coating was not very dense, as the methoxy-ended PEG would shield the negative charge of PLGA and reduce the

nanoparticle surface potential. Similarly, researchers reported that PEGylation of poly-l-lysine dendrimers enhanced their transport to the LNs after subcutaneous injection. But it is unclear if the addition of PEG or the increase in size is primarily responsible for the improved LN accumulation, as dendrimers increased from 4 nm to 14 nm in diameter going from out of range to within range of size requirements for preferential transport by lymphatics [41]. Combined, these results suggest that hydrophilicity through addition of PEG, for example, may be beneficial for enhancing nanoparticle transport by lymphatics, but also highlight the importance to more critically assess the effect of surface chemistry, particularly PEG density, on nanoparticle transport by lymphatics.

PEGylating nanoparticles is a strategy that has been used extensively to enhance nanoparticle interactions with biological materials. PEGylation can improve nanoparticle drug delivery by reducing charge interactions with extracellular matrix and by preventing opsonization and phagocytosis by immune cells [86, 87]. Most notably, the chemotherapeutic drug doxorubicin, formulated as PEGylated liposomes, is one of the few FDA-approved nanoparticle treatments. The addition of PEG enhanced the circulation time of the chemotherapeutic, improving the overall efficacy [86-91]. PEG coatings can be optimized by modulating the density and molecular weight (MW) of PEG itself on the surface of nanoparticles. As PEG density on the nanoparticle surface is increased, the conformation of PEG transitions from a "mushroom" conformation that is more self-coiled to a "dense brush" conformation that is more linear, due to steric hindrances [92]. PEG conformation has been shown to be critical in enhancing nanoparticle transport across biological barriers. For example, to cross the mucus barrier, researchers have found that nanoparticles need to be in the "dense brush" conformation [93, 94]. Similarly, researchers have shown that only small (<100 nm) nanoparticles coated with PEG in the dense brush conformation effectively penetrate the

interstitial tissue in the brain [95]. Additionally, tumor interstitial tissue penetration has also been improved by PEGylating nanoparticles: the addition of PEG to the surface of model, 60 nm negatively charged polystyrene (PS) nanoparticles (in an "intermediate brush" conformation) enhanced nanoparticle diffusion through breast cancer xenograft slices ex vivo compared to nanoparticles coated with PEG in the mushroom conformation [96]. These results demonstrate that the conformation of PEG on the surface is a key parameter that can affect nanoparticle delivery across biological barriers. However, how PEG density modulates nanoparticle transport by lymphatic vessels, and thus what the PEG density requirements are to maximize nanoparticle transport to the LNs and the mechanisms used by lymphatics to transport nanoparticles, remain poorly understood.

Here, we investigated the effect of PEG surface density on nanoparticle transport by lymphatic vessels and identified the PEG density required to maximize nanoparticle transport. We generated a library of nanoparticles coated with varying PEG densities, thus different PEG conformations, and tested their transport by LECs (LECs) using an established in vitro lymphatic transport model and in vivo after intradermal injection in mice [17]. Our resulting nanoparticle design criteria maximize nanoparticle transport to the LNs via lymphatic vessels, and therefore may enhance efficacy of immunotherapies and streamline the design of lymphatic targeting nanoparticle formulations.

3.2 Materials and Methods

3.2.1 *Nanoparticle Formulation*

100 nm or 40 nm fluorescent carboxyl (COOH)-modified PS nanoparticles (Thermo Fisher Scientific, F8801) were covalently modified with 5 kDa MW methoxy-PEG-amine (NH_2) (Creative PEGworks), as previously described [95]. Briefly, PS-COOH particles were suspended at 0.1% w/v in 200 mM borate buffer (pH = 8.2). Nanoparticles were generated with the following PEG concentrations: 350 μM (theoretical 100% PEG coverage of COOH groups), 175 μM (50% COOH groups), 87.5 μM (25% COOH groups), and 35 μM (10% COOH groups). PEG was conjugated to nanoparticles using 7 mM N-Hydroxysulfosuccinimide (NHS) (Sigma) and 0.02 mM 1-Ethyl-3-(3-dimethylaminopropyl) carbodiimide (EDC) (Invitrogen). Carboxyl-terminated and amine-terminated 5 kDa PEG was used to generate PEGylated nanoparticles with different surface charges. The reaction was allowed to proceed on a rotary incubator at room temperature for at least 4 hours. Nanoparticles were collected using 100k MWCO centrifugal filters (Amicon Ultra; Millipore) and washed with deionized (DI) water. Nanoparticles were resuspended at 1% w/v in DI water and stored at 4°C.

3.2.2 Nanoparticle Characterization

Dynamic light scattering (DLS) was used to measure the hydrodynamic diameter and polydispersity index (PDI) of nanoparticles. Phase analysis light scattering (PALS) was used for measuring ζ-potential (NanoBrook Omni). Measurements were performed using a scattering angle of 90° at 25°C. Measurements were based on intensity of reflected light from scattered particles.

3.2.3 PEG Density Characterization

PEG density was determined using a previously published method [97]. Briefly, 5kDa PEG-

NH2 (Creative PEGworks) conjugated to fluorescein isothiocyanate (FITC) was conjugated to fluorescent (AlexaFluor®555) 100 nm carboxyl-modified nanoparticles. A FITC-PEG-NH2 standard curve was generated in DI water to calculate the PEG amount on the nanoparticle surface using a plate reader (Tecan Spark Multimode Microplate Reader). From these measurements, PEG grafting distance (D) and PEG density were estimated using the Flory radius of PEG (Rf). The Flory radius of a polymer chain is defined as $Rf \sim \alpha N^{3/5}$, where N is the degree of polymerization, and α is the effective monomer length. An unconstrained 5 kDa PEG chain has a Rf of 5.4 nm and occupies 22.7 nm^2. PEG density and conformation can be correlated to the ratio of Rf/D, with Rf/D < 1-1.5 yielding a mushroom conformation, 1-1.5< Rf/D > 4 yielding a brush conformation, and Rf/D > 4 yielding a dense brush conformation.

Quantification of PEG on the surface of nanoparticles was performed using Fourier-Transform infrared (FTIR) spectroscopy (Vertex – 70 Bruker). PEGylated nanoparticle samples were scanned over a range of 400 – 4000 cm^{-1}. The peak corresponding to the C-O-C ester linkages found in PEG chains was identified at 1083 cm^{-1} [98]. To quantify the amount of PEG on the surface of the nanoparticles, the intensity of the 1083 cm^{-1} peak was measured for known amounts of PEG, and a standard curve was generated. Using the same calculations as above, the R_f/D value, which corresponds to the conformation of the PEG on the surface of a nanoparticle, was determined [98, 99].

3.2.4 Nanoparticle Uptake

Immortalized human LECs (hiLECs, [100]) were seeded at a density of 200,000 cells/cm^2 onto collagen (Corning)- coated plates and cultured in endothelial growth media-2 (EGM2, Lonza) at 37ºC and 5% CO2 overnight. hiLECs were incubated with 0.05% w/v nanoparticles for 3 h and uptake was assessed by flow cytometry or fluorescence microscopy. For fluorescence microscopy,

samples were fixed with 2% paraformaldehyde (PFA, ThermoFisher) and imaged using a Zeiss Axio Observer. For flow cytometry, cells were released from the substrate using Accutase® (Innovative Cell Technologies), fixed with 2% PFA, and flow cytometry was performed using a BD FACSelecta. Data was analyzed using FlowJo software (Tree Star) and FIJI (ImageJ).

3.2.5 Lymphatic Transport Model

Nanoparticle transport across LECs was assessed using an established in vitro model that recapitulates in vivo lymphatic transport [17]. Briefly, primary human dermal LECs (hLECs, Promocell C-12217) were seeded on 1.0 µm pore size, 12 mm transwell inserts (Falcon) at 200,000 cells/cm^2 and cultured in EGM2 (Lonza) at 37ºC and 5% CO2 for 48 h. Cells were pretreated with 1 µm/s transmural flow to simulate the tissue microenvironment. hLECs were treated with 1% w/v nanoparticles on the apical side and the basolateral compartment was sampled every 3 h for up to 24 h. Fluorescence intensity was measured using a plate reader (Tecan) and nanoparticles transported was calculated using a standard curve. Transport experiments were performed in EGM2 without growth factors to avoid the confounding effects of growth factors. To probe the transport mechanism the following transport inhibitors were used: 100 nM Adrenomedullin (Abcam ab276417), 62.5 µM Dynasore (Sigma D7693), or 62.5 µM Amiloride (Sigma A7410). Transport inhibitors were applied 2 hours prior to introduction of nanoparticles. Effective permeability was estimated using the following equation: $P_{eff} = \frac{C_{lower}V_{lower}}{tSC_{initial}}$, where C = concentration, V_{lower} = volume of the basolateral compartment, S = surface area, and t = time. hLEC monolayer integrity was confirmed after experiments using immunofluorescence.

3.2.6 Immunofluorescence Staining

Cells were fixed in 2% PFA for 15 minutes and incubated with mouse anti-human VE-Cadherin (BD Sciences) at 4^{o}C overnight. Secondary antibodies conjugated to Alexa Fluor® 488 or 647 were used for detection (Thermo Fisher). Slides were mounted using DAPI (4',6-diamidino-2-phenylindole)-containing Vectashield (Vector Laboratories Inc., Burlingame, CA) and imaged using a Zeiss Axio Observer. Image processing was performed using FIJI (NIH).

3.2.7 C57Bl/6J Lymphatic Delivery Model

10 μL of 5 mg/mL, fluorescently-labeled nanoparticles was intradermally administered to female C57Bl/6J mice (8-12 weeks old) in their forelimbs. Fluorescence intensity was measured using IVIS Spectrum Fluorescent & Chemiluminescent Imaging System (Caliper Life Sciences) over a 12h time period. Distance of nanoparticle transport was calculated from centroid of injection site to maximally distant pixel of fluorescence signal using ImageJ. This pixel length was then converted to centimeters. Mice were anesthetized with isoflurane prior to nanoparticle injection and during imaging. Mice were euthanized after the final time point (8 or 12 h). Draining LNs were collected and homogenized to quantify the fluorescence signal from nanoparticles using a plate reader (Tecan). LNs were also fixed in 4% PFA for 6 hours and treated with a sucrose gradient. Tissues were then embedded within OCT (ThermoFisher), sectioned, and stained for FITC-B220 (BioLegend). Slides were mounted using DAPI (4',6-diamidino-2- phenylindole)-containing Vectashield (Vector Laboratories Inc., Burlingame, CA) and imaged using a Zeiss Axio Observer. Image processing was performed using FIJI (NIH). All procedures were approved by the University of Maryland, College Park IACUC.

3.2.8 Statistics

Group analysis was performed using a 2-way ANOVA, followed by Tukey's post-test. Unpaired Student's t-test was used to examine differences between only two groups. A value of $p < 0.05$ was considered significant (GraphPad). All data is presented as mean ± standard error of the mean (SEM).

3.3 Results

3.3.1 Increasing PEG density on nanoparticles neutralizes surface ζ-potential

The conformation of PEG on the surface of nanoparticles has been shown to affect how the nanoparticle interacts with surrounding tissues and cells [95, 97, 101]. In this study, we generated differentially PEGylated nanoparticles to determine how tuning PEG grafting density modulated surface PEG conformation and nanoparticle transport by LECs. We generated PS-COOH nanoparticles with varying PEG density, R_f/D of 4.9 ± 0.1, 2.4 ± 0.1, 1.7 ± 0.1, and 1.3 ± 0.1 (**Fig 3A**). These R_f/D values can be correlated to the conformation of PEG on the nanoparticle surface **(Fig 3B**). PEG grafting to the surface of the nanoparticle and R_f/D values were confirmed using FTIR (**Fig 3C-D**). The 1083 cm^{-1} peak corresponds to C-O-C ester linkages characteristic of PEG chains. FTIR spectra of the additional nanoparticle formulations can be seen in the supplemental materials (**S1**). As expected, we found that increasing PEG density on nanoparticles slightly increased their diameter: unmodified PS-COOH nanoparticles had a diameter of 108 ± 1 nm, while addition of PEG increased nanoparticle diameter to 120 – 150 nm (**Fig 3E**). PEGylation also neutralized the negative surface charge of PS-COOH nanoparticles, from a ζ-potential of -22.4 ± 3.3 mV to -2.9 ± 2.5 mV (R_f/D = 4.9), -5.1± 3.5 mV (R_f/D = 2.4), -4.7 ± 2.5 mV (R_f/D = 1.7), and -10.2 ± 6.6 mV (R_f/D = 1.3) (**Fig 3F**). These ζ-potential measurements demonstrate that the addition of any PEG is sufficient to largely shield the negative surface charge of the PS nanoparticles. Neutrally charged PEG was applied to the surface of nanoparticles since neutrally charged nanoparticles were transported most efficiently across LEC barriers *in-vitro* (**S2**). *In* addition, we confirmed stability of PEGylated nanoparticle formulations in EGM-2 media over 24 hours to ensure no aggregation occurred during the experimental time (**S3**).

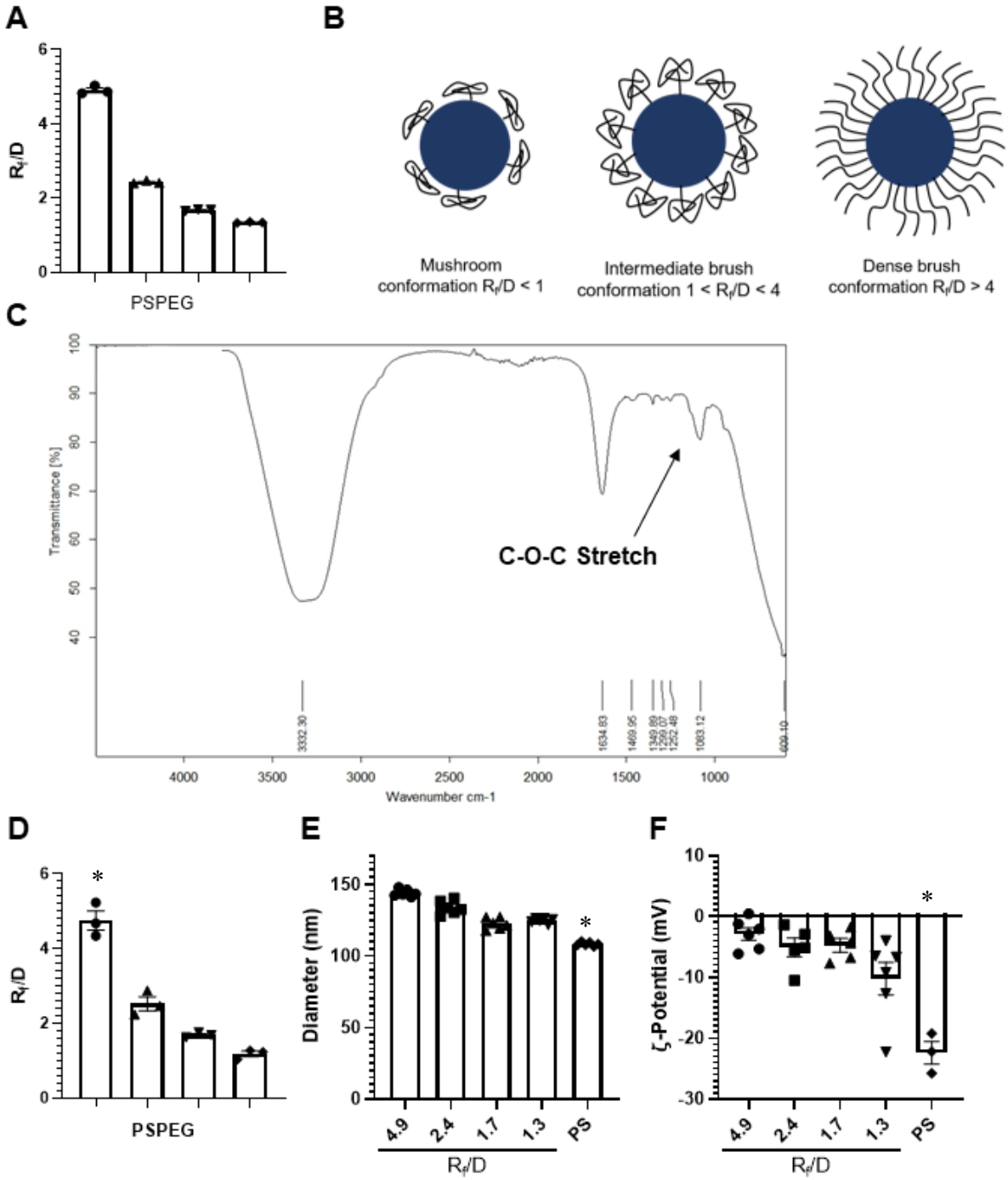

Figure 3 *PEG grafted onto nanoparticles at different densities reduces surface charge.* **A)** Rf/D values of PSPEG measured via fluorescence. **B)** Schematic of PEG conformation on a model solid nanoparticle. **C)** Fourier Transform Infrared (FTIR) spectrum of PEG grafted on the surface of the nanoparticle. **D)** Rf/D analysis as measured with FTIR. **E)** Dynamic Light Scattering (DLS) measurement of PEGylated NP diameter and **F)** Phase Analysis Light Scattering (PALS) measurement of NP ζ – potential. Data shown as mean ± SEM (n = 3 – 6 nanoparticle batches) $p^*<0.05$.

3.3.2 Dense brush PEG coatings on nanoparticles maximize their transport across LECs

We next sought to assess the effect of PEG density on nanoparticle transport by lymphatics. We used an in vitro transendothelial transport model (**Fig 4A**), where a monolayer of primary human LECs was cultured on the bottom of a collagen-coated transwell (**Fig 4B**) to simulate transport from the interstitium into the lymphatic vessel [17]. We found that the unmodified PS-COOH nanoparticles were minimally transported across LECs (0.03 ± 0.03%, **Fig 4B**) while 1.4 ± 0.3 % of densely PEGylated $PSPEG_{Rf/D = 4.9}$ were transported after 6h (**Fig 4B**). By 24h there was a ~90-fold increase in transport, with 4.2 ± 0.7% $PSPEG_{Rf/D = 4.9}$ vs 0.05 ± 0.05% PS-COOH transported (**Fig 4A**). We found that the effective permeability (P_{eff}) of the monolayer to nanoparticles also increased from 0.02 ± 0.02 μL/hr-cm^2 for PS-COOH to 1.9 ± 0.3 μL/hr-cm^2 for $PSPEG_{Rf/D = 4.9,}$ without affecting the endothelial integrity (**Fig 4C-D**). Interestingly, any addition of PEG significantly increased nanoparticle transport by LECs after 24h (**Fig 4C**), but $1 < R_f/D < 3$ led to less transport than $R_f/D = 4.9$ (**Fig 4C**). We also found that both PEGylated and unmodified nanoparticles were internalized by LECs (**Fig 4D**). To further probe if the effects of PEG density on nanoparticle transport across LECs translate across different nanoparticle sizes, we modified 40 nm PS-COOH nanoparticles with PEG (**S4**). We found that higher PEG density on 40 nm nanoparticles ($R_f/D = 4.4$) enhanced nanoparticle transport across LECs compared to lower PEG density ($R_f/D = 0.9$) (**Fig 4E**). Mass balance of nanoparticles in the top and bottom well were confirmed with >95% recovered after 24 hours (**S5**). These results indicate that the addition of PEG enhances the transport of nanoparticles across lymphatics and that “dense brush” PEG coatings maximize this transport.

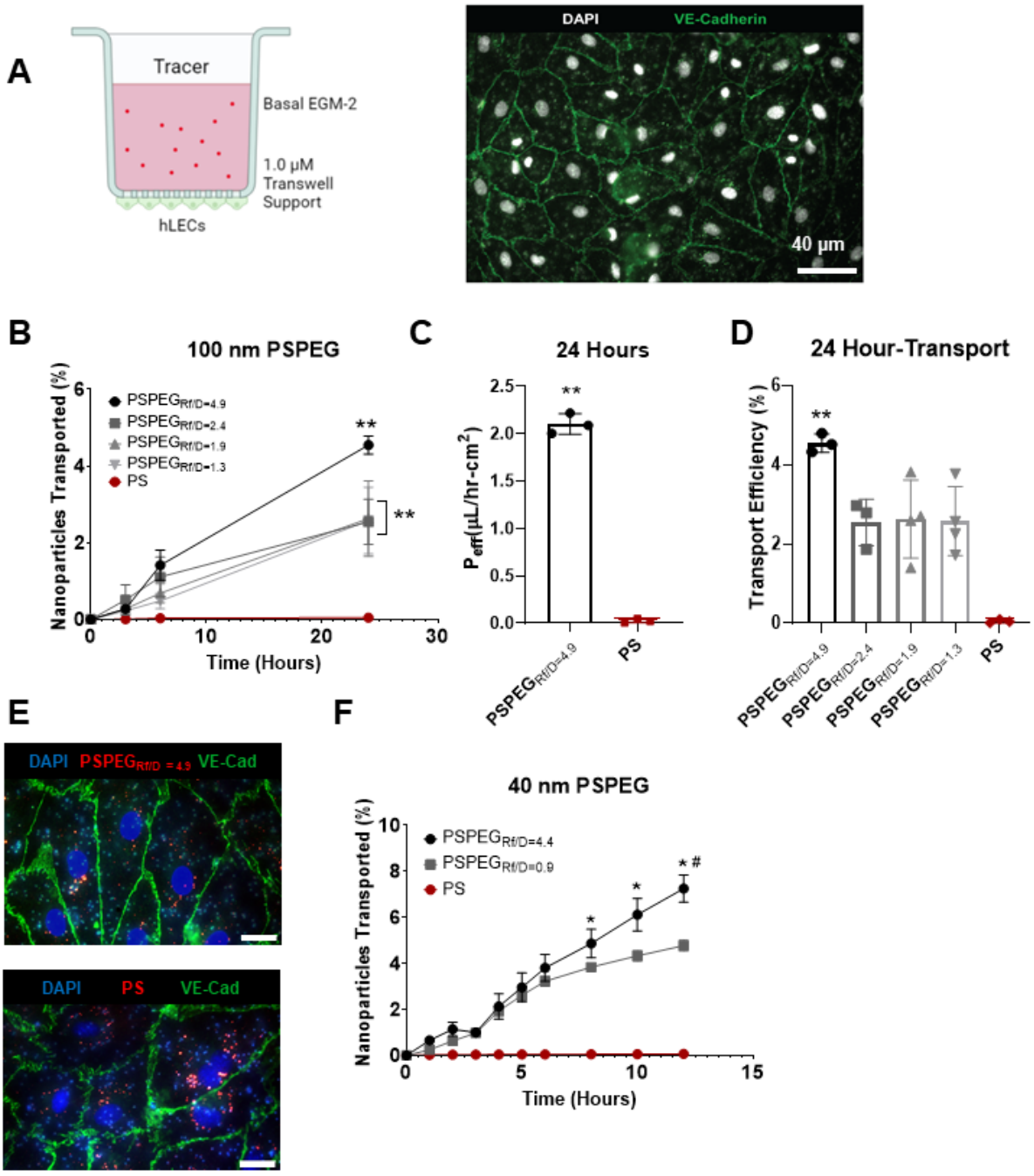

Figure 4 *PEG Coating Improves Transport of 100 nm NP Across LECs.* **A)** Schematic of transport model and representative image showing monolayer of LECs via VE-cadherin (green) and nuclei via DAPI (white). **B)** Representative images of LEC monolayer stained for VE-cadherin (green) and DAPI (blue) **C)** Percent of 100 nm NP transported across LEC monolayer over time. **D)** Measured effective permeability (Peff) of LEC monolayer to NP formulations. Percent of NP transported across LEC monolayer at the 24-hour time point. **E)** Representative images of LEC monolayer stained for VE-cadherin (green) and DAPI (blue) treated with unmodified PS or PSPEG NPs (red). (n = 3-4). F) Percent of 40 nm NP transported across LEC monolayer over time. Data presented as mean ± SEM (*p<0.05; **p<0.01; #p<0.01 comparing PSPEGRf/D=4.4 and PSPEGRf/D=0.9).

3.3.3 PEG density on nanoparticles affects cellular mechanisms used by LECs to transport nanoparticles

To elucidate the mechanisms used by LECs to transport nanoparticles, we first investigated how PEG density on nanoparticles affects their uptake by LECs, as uptake is the first step in transcellular transport of materials. Using fluorescence microscopy and flow cytometry, we found that uptake of all nanoparticles by hiLECs was comparable, as indicated by the similar median fluorescence intensities (MFI) and similar number of cells positive for nanoparticles (> 85% for all nanoparticles, **Table 1**) at 3h, 6h, and 8h. Next, we investigated the cellular mechanisms involved in this transport using small molecule transport inhibitors to block the different cellular mechanisms. Several cellular mechanisms have been shown to be involved in nanoparticle transport across cellular barriers, including macropinocytosis, clathrin and/or caveolin-mediated endocytosis (micropinocytosis), as well as paracellular transport. We used amiloride to block macropinocytosis, adrenomedullin to reduce paracellular transport (by tightening cell-cell junctions, **Fig 5A**), and dynasore to inhibit the dynamin motor required for vesicle-based micropinocytosis. We found that 100 nm $PSPEG_{Rf/D = 4.9}$ were not transported by macropinocytosis (**Fig 5B**). However, both adrenomedullin and Dynasore reduced 100 nm $PSPEG_{Rf/D = 4.9}$ transport (**Fig 5B**), suggesting that both paracellular transport and micropinocytosis mechanisms are involved in nanoparticle transport by lymphatics. We also found that for the low PEG density, 100 nm $PSPEG_{Rf/D=1.3}$ transport was reduced when each pathway was inhibited, suggesting paracellular transport, micropinocytosis, and macropinocytosis are all involved in transport of 100 nm $PSPEG_{Rf/D=1.3}$ across LECs (**Fig 5C**).

Table 1: PEG conformation does not affect nanoparticle (NP) uptake in LECs. Median fluorescence intensity (MFI, imaging, n = 8) and % hiLECs positive for nanoparticles (flow cytometry, n = 3-4) after 3h., 6h, 8h.

	Incubation Time (h):	**3 h**		**6 h**		**8 h**	
NP type	**Rf/D**	**MFI**	**%NP+ LECs**	**MFI**	**%NP+ LECs**	**MFI**	**%NP+ LECs**
PSPEG	4.9 ± 0.1	1.16 ± 0.36	91 ± 1	1.27 ± 0.28	92 ± 1	1.11 ± 0.18	94 ± 1
PSPEG	2.4 ± 0.1	0.93 ± 0.27	86 ± 1	1.02 ± 0.19	89 ± 2	1.05 ± 0.25	92 ± 2
PSPEG	1.7 ± 0.1	0.91 ± 0.23	91 ± 1	0.93 ± 0.31	90 ± 1	1.12 ± 0.35	92 ± 4
PSPEG	1.3 ± 0.1	0.93 ± 0.30	91 ± 1	1.05 ± 0.24	92 ± 1	0.98 ± 0.12	91 ± 2
PS	-	1.15 ± 0.23	91 ± 1	0.98 ± 0.17	91 ± 1	0.95 ± 0.27	89 ± 2

To further probe the mechanisms of transport, and the nanoparticle characteristics regulating lymphatic transport, we used differentially PEGylated 40 nm nanoparticles (**S3**). When 40 nm densely PEGylated nanoparticles ($PSPEG_{Rf/D=4.4}$) were introduced to the transport model, we found that dynasore, adrenomedullin, and amiloride were each able to reduce transport (**Fig 5D**), suggesting that paracellular transport, micropinocytosis, and macropinocytosis are all involved in 40nm $PSPEG_{Rf/D=4.4}$ transport across LECs. The transport of the 40 nm $PSPEG_{Rf/D=0.9}$ was affected by transport inhibitors in a similar fashion as the 100 nm $PSPEG_{Rf/D=4.9}$, with adrenomedullin and Dynasore reducing transport, but amiloride having no significant effect, (**Fig 5E**), suggesting that only micropinocytosis and paracellular transport are involved. To further investigate the specific micropinocytosis mechanisms, we used fluorescent microscopy to determine if nanoparticles colocalized with known endocytosis mediators. We found that 100 nm PEGylated nanoparticles colocalized with clathrin in LECs, suggesting that clathrin-mediated endocytosis is one of the mechanisms involved in 100 nm $PSPEG_{Rf/D=4.9}$ transport by LECs (**Fig 5F, S6(13)**). The central localization of the nanoparticles is indicative of endocytosis, where early endosomes are often trafficked towards the center of cells [102]. The mechanisms by which PEG density modulates nanoparticle transport mechanisms used by LECs are currently under investigation in our lab.

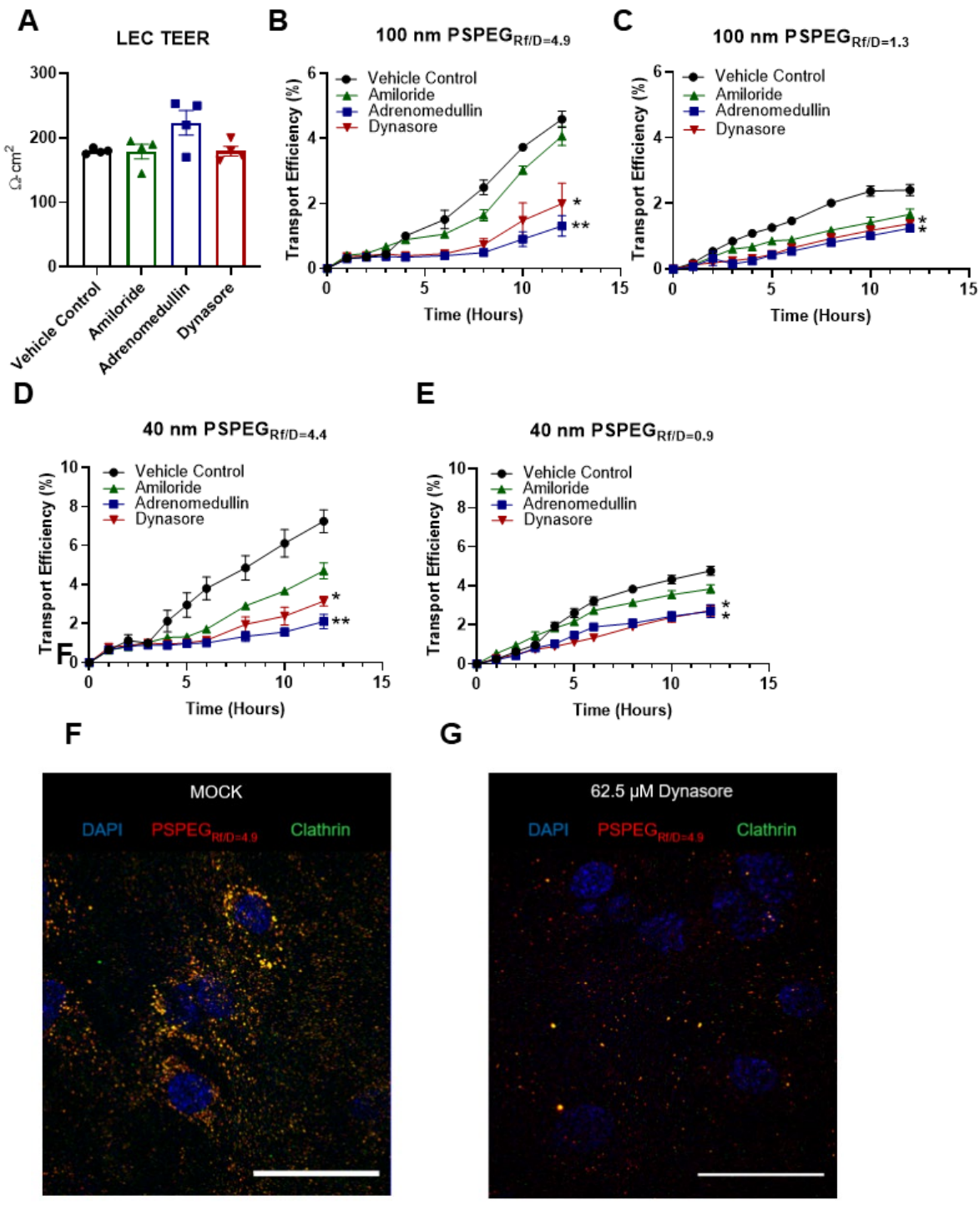
A
LEC TEER
Ω·cm²
300
200
100
0
Vehicle Control
Amiloride
Adrenomedullin
Dynasore
B
100 nm PSPEG Rf/D=4.9
Transport Efficiency (%)
Time (Hours)
Vehicle Control
Amiloride
Adrenomedullin
Dynasore
C
100 nm PSPEG Rf/D=1.3
Transport Efficiency (%)
Time (Hours)
D
40 nm PSPEG Rf/D=4.4
Transport Efficiency (%)
Time (Hours)
E
40 nm PSPEG Rf/D=0.9
Transport Efficiency (%)
Time (Hours)
F
MOCK
DAPI
PSPEG Rf/D=4.9
Clathrin
G
62.5 μM Dynasore
DAPI
PSPEG Rf/D=4.9
Clathrin

Figure 5 *Both paracellular and transcellular transport mechanisms regulate Nanoparticle transport across LECs in-vitro.* **A)** Trans-endothelial electrical resistance (TEER) of the LEC monolayer after treatment with transport inhibitors. **B)** Transport efficiency of 100 nm PSPEGRf/D=4.9 nanoparticle in the presence of transport inhibitors. **C)** Transport efficiency of 100 nm PSPEGRf/D=1.3 NP in the presence of transport inhibitors. **D)** Transport efficiency of 40 nm PSPEGRf/D=4.4 nanoparticle in the presence of transport inhibitors. **E)** Transport efficiency of 40 nm PSPEGRf/D=0.9 nanoparticle in the presence of transport inhibitors. **F)** Confocal fluorescence image of PSPEGRf/D=4.9 within LECs treated with the vehicle control and **G)** confocal fluorescence image of 100 nm PSPEGRf/D=4.9 within LECs treated with Dynasore Scale bar: 30 μm. (n = 3-4) Data presented as mean ± SEM (*p<0.05; **p<0.01).

3.3.4 Densely PEGylated nanoparticles accumulate in the LNs in vivo

To confirm that our in vitro findings are representative of in vivo lymphatic transport, we probed nanoparticle accumulation in the LNs over 12 h after intradermal injection in mice. We found that minimal amounts of 100 nm PS-COOH nanoparticles were transported to the LNs even after 12 h, while 100 nm $PSPEG_{Rf/D = 4.9}$ nanoparticles were transported to the LNs as early as 4 h after injection (**Fig 6A**). We measured the distance from injection site and found that after 12 h, 100 nm PS-COOH beads traveled 0.24 ± 0.04 cm from the injection site, whereas 100 nm $PSPEG_{Rf/D = 1.3}$ traveled 0.61 ± 0.01 cm from the injection site (**Fig 6B**). 100 nm $PSPEG_{Rf/D = 4.9}$ traveled the furthest from the injection site, measuring 0.73 ± 0.04 cm from the nanoparticle injection site. Distance traveled was significantly higher for 100 nm $PSPEG_{Rf/D=4.9}$ at 8 h and 12 h compared to both 100 nm PS-COOH and $PSPEG_{Rf/D=1.3}$. Both PEGylated 100 nm nanoparticle formulations significantly improved distance traveled compared to unmodified 100 nm PS-COOH nanoparticles (**Fig 6B**), further indicating that a dense coating of PEG optimizes transport of nanoparticles to LNs. When we quantified fluorescence in draining LNs, we found that both100 nm $PSPEG_{Rf/D=4.9}$ and $PSPEG_{Rf/D=1.3}$ accumulated in the LN after 8h whereas 100 nm PS-COOH had a significantly reduced signal (**Fig 6C-F**). To examine the size dependence on in-vivo transport we intradermally administered densely PEGylated 40 nm nanoparticles ($PSPEG_{Rf/D=4.4}$), sparsely PEGylated 40 nm

nanoparticles ($PSPEG_{Rf/D=0.9}$), and 40 nm PS-COOH nanoparticles thenmeasured transport to draining LNs via IVIS. Like the 100 nm formulations, PEGylated 40 nm nanoparticles began to appear in draining LNs 4 h after intradermal injection (**Fig 7A**). Similar to our findings with 100 nm nanoparticles, the addition of some PEG increased the distance 40 nm nanoparticles traveled from 0.29 ± 0.05 cm by 40 nm PS-COOH to 0.69 ± 0.09 cm by 40 nm $PSPEG_{Rf/D=0.9}$. 40 nm $PSPEG_{Rf/D=4.4}$ were found to travel furthest from the injection site, with 0.88 ± 0.06 cm after 12h (**Fig 7B**). When we quantified fluorescence in draining LNs, we found that both 40 nm $PSPEG_{Rf/D=4.4}$ and $PSPEG_{Rf/D=0.9}$ accumulated in the LN after 8h whereas 40 nm PS-COOH had a significantly lower signal (**Fig 7D-F**). We then examined nanoparticle localization within draining LNs using IF imaging. IF imaging confirmed IVIS results, with no PS-COOH signal observed in the LNs after 8h. $PSPEG_{Rf/D=4.9}$ was observed within the LN after 8h for both 40 nm and 100 nm nanoparticle sizes. PEGylated formulations appear to be localized within the subcapsular sinus, suggesting that lymphatic drainage through the afferent lymphatic vessels mediated transport to the LN (**Fig 7C, 6C**).

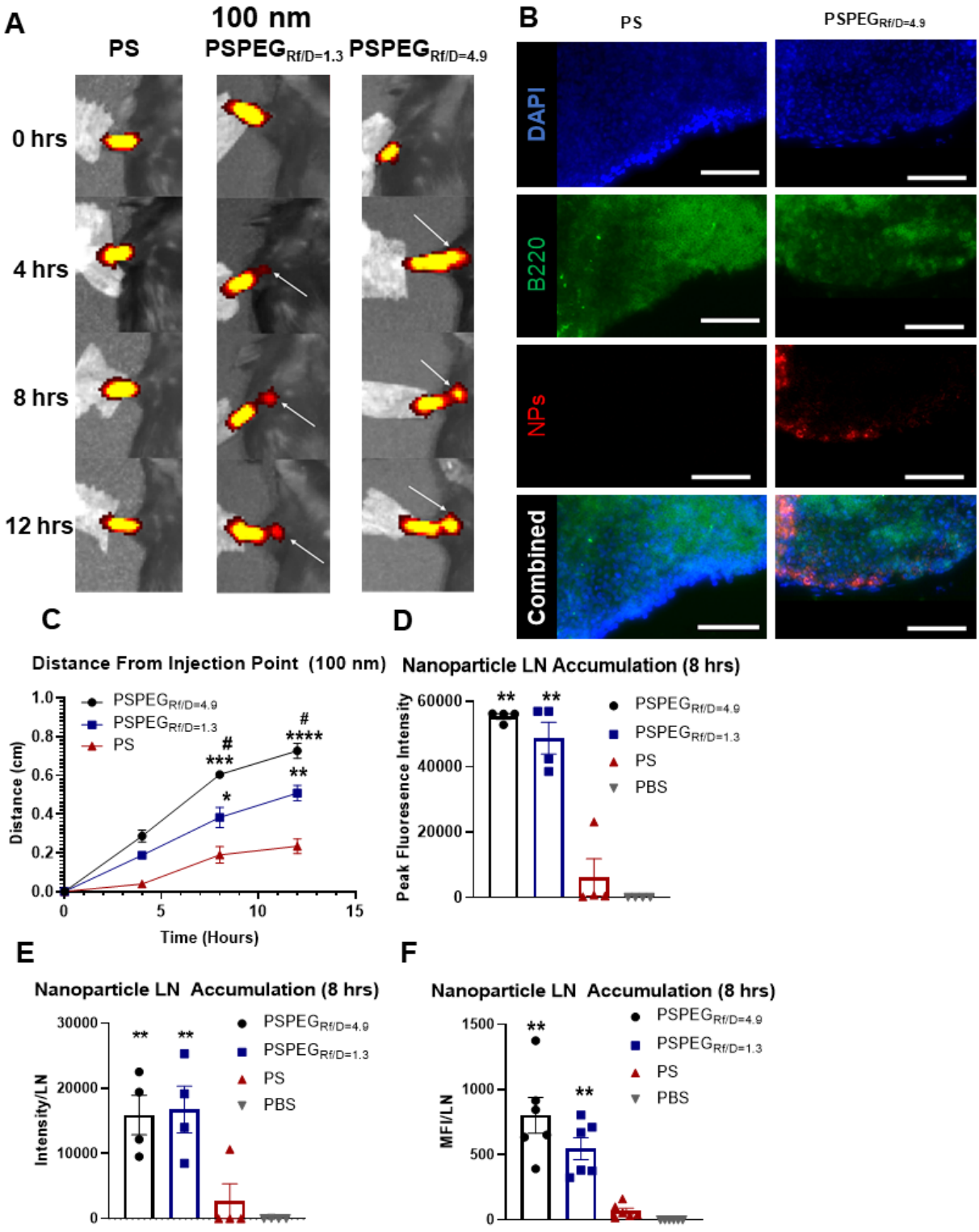
A
100 nm
PS
PSPEG Rf/D=1.3
PSPEG Rf/D=4.9
0 hrs
4 hrs
8 hrs
12 hrs
B
PS
PSPEG Rf/D=4.9
DAPI
B220
NPs
Combined
C
Distance From Injection Point (100 nm)
PSPEG Rf/D=4.9
PSPEG Rf/D=1.3
PS
Distance (cm)
Time (Hours)
D
Nanoparticle LN Accumulation (8 hrs)
Peak Fluoresence Intensity
PSPEG Rf/D=4.9
PSPEG Rf/D=1.3
PS
PBS
E
Nanoparticle LN Accumulation (8 hrs)
Intensity/LN
PSPEG Rf/D=4.9
PSPEG Rf/D=1.3
PS
PBS
F
Nanoparticle LN Accumulation (8 hrs)
MFI/LN
PSPEG Rf/D=4.9
PSPEG Rf/D=1.3
PS
PBS

Figure 6 *Dense-Brush PEG Coating Required for Improved Lymphatic Targeting* In-Vivo. A) Representative images of intradermally injected 100nm Nanoparticles in C57Bl/6J mice up to 12h post injection measured using IVIS. White arrow indicates accumulation within lymph nodes. B) Nanoparticle transport measured as maximal distance of fluorescent signal from injection site. C) Lymph node sections stained for DAPI (nucleus) and B220 (B-cells) after injection of 100 nm PS or PSPEGRf/D=4.9 nanoparticles. D) Nanoparticle accumulation within LN measured as average fluorescence signal over the area of dissected LN (MFI/LN) and as E) Peak fluorescence signal. F) Fluorescence signal of homogenized lymph nodes. (n = 6) Data presented as mean ± SEM (*p<0.05; **p<0.01, *** p<0.001; #p<0.01 comparing PSPEGRf/D=4.9 and PSPEGRf/D=1.3).

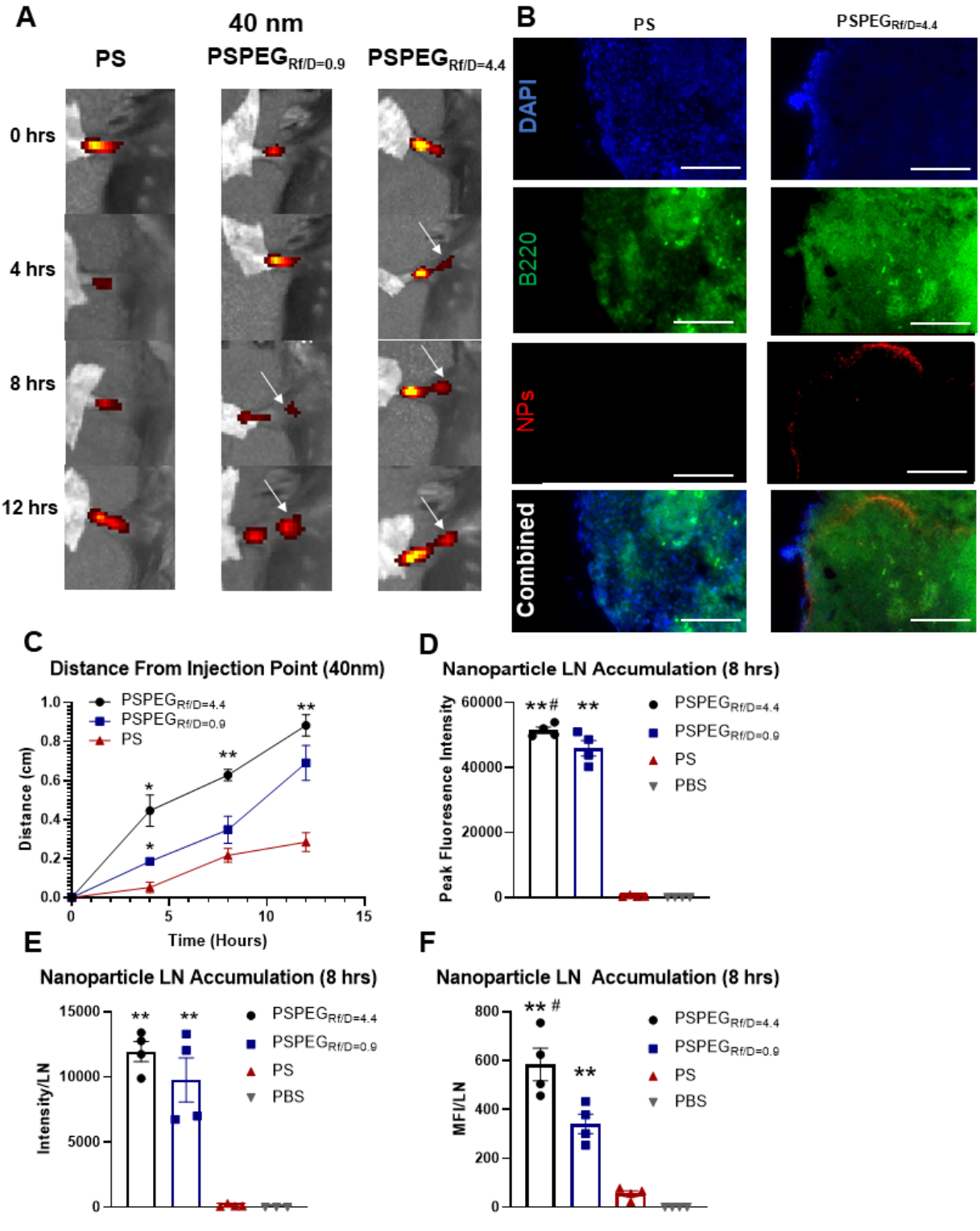
A
40 nm
PS
PSPEG Rf/D=0.9
PSPEG Rf/D=4.4
0 hrs
4 hrs
8 hrs
12 hrs
B
PS
PSPEG Rf/D=4.4
DAPI
B220
NPs
Combined
C
Distance From Injection Point (40nm)
PSPEG Rf/D=4.4
PSPEG Rf/D=0.9
PS
Distance (cm)
Time (Hours)
D
Nanoparticle LN Accumulation (8 hrs)
Peak Fluoresence Intensity
PSPEG Rf/D=4.4
PSPEG Rf/D=0.9
PS
PBS
E
Nanoparticle LN Accumulation (8 hrs)
Intensity/LN
PSPEG Rf/D=4.4
PSPEG Rf/D=0.9
PS
PBS
F
Nanoparticle LN Accumulation (8 hrs)
MFI/LN
PSPEG Rf/D=4.4
PSPEG Rf/D=0.9
PS
PBS

Figure 7 *Dense-Brush PEG Coating Required for Improved Lymphatic Targeting In-Vivo*. **A)** Representative images of fluorescent signal from intradermally injected 40 nm Nanoparticles in C57Bl/6J mice at different times post injection measured using IVIS. White arrow indicates accumulation within lymph nodes. **B)** Transport measured as maximal distance of fluorescent signal from injection site.. **C)** Lymph node sections stained for DAPI (nucleus) and B220 (B-cells) with nanoparticles seen in red for 40 nm PS and PSPEGRf/D=4.4. **D)** Nanoparticle accumulation within LN measured as average fluorescence signal over the area of dissected LN (MFI/LN) and as **E)** peak fluorescence signal. **F)** Fluorescence signal of homogenized lymph nodes. (n = 6) Data presented as mean ± SEM (*p<0.05; **p<0.01; #p<0.01 comparing PSPEGRf/D=4.4 and PSPEGRf/D=0.9).

Supplemental Data Figures

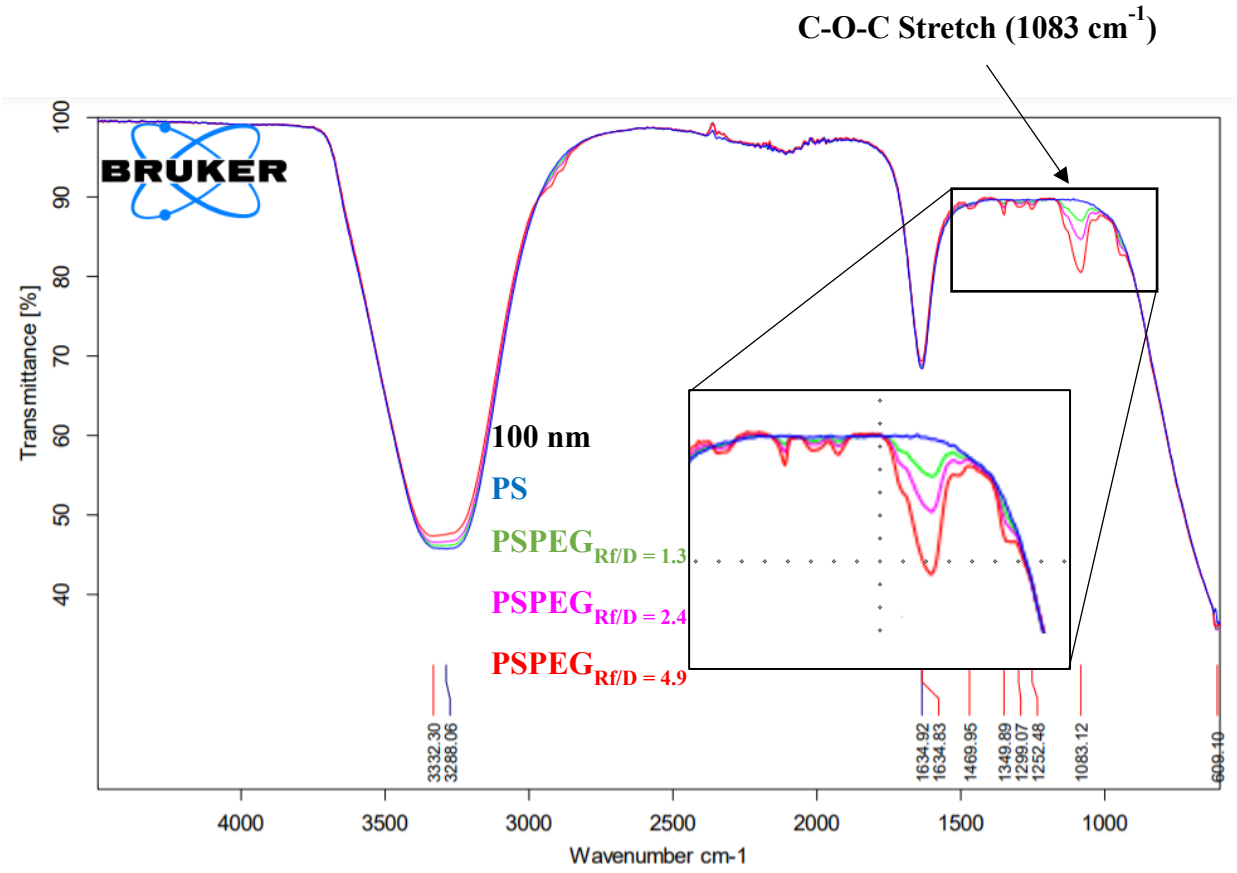

Figure 8 Supplemental Figure 1: FTIR Spectra of 100 nm PSPEG Formulations: Representative spectra of PS, PSPEGRf/D = 1.3, PSPEGRf/D = 2.4, and PSPEGRf/D = 4.9 with ester linkage indicated at 1083 cm-1 peak.

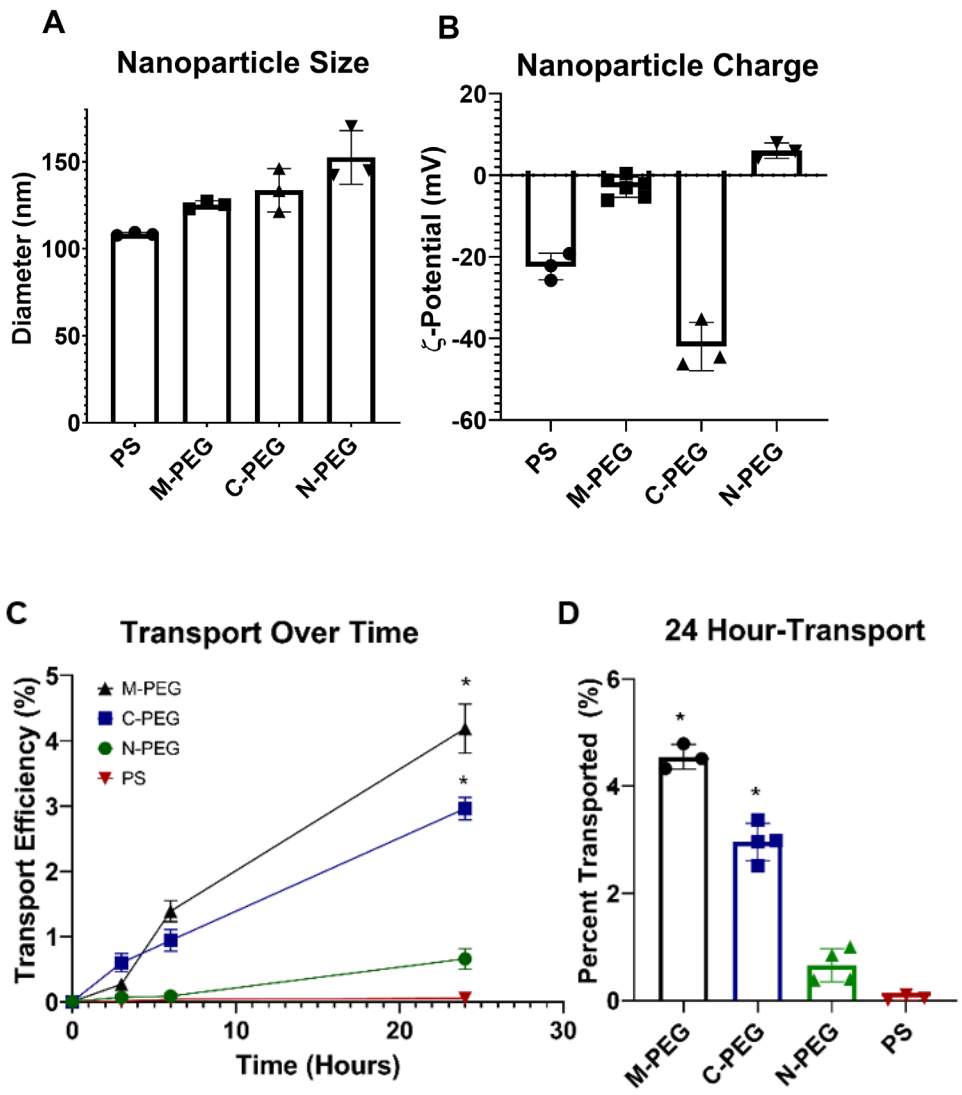

Figure 9 Supplemental Figure 2: *Effect of Nanoparticle Charge on In-Vitro Lymphatic Transport.* PEG-amine polymers with charged terminal groups were grafted to the surface of PS Nanoparticles: C-PEG: Carboxyl-PEG coated nanoparticles, M-PEG: Methoxy-PEG coated nanoparticles, N-PEG: Amine-PEG coated PEG. **A)** DLS measurements of PEGylated nanoparticle diameter. **B)** Phase-Analysis Light Scattering (PALS) measurement of NP zeta-potential. Data shown as mean ± SEM (n = 3-6). The relatively low degree of positive charge on the amine nanoparticles is likely due to the pKa of amines (~11) being further from neutral then the carboxyl pka (~5.0). **C)** Transport efficiency over a 24-hour period. **D)** Transport efficiency at the 24-hour mark (*$p<0.05$, n = 3-6).

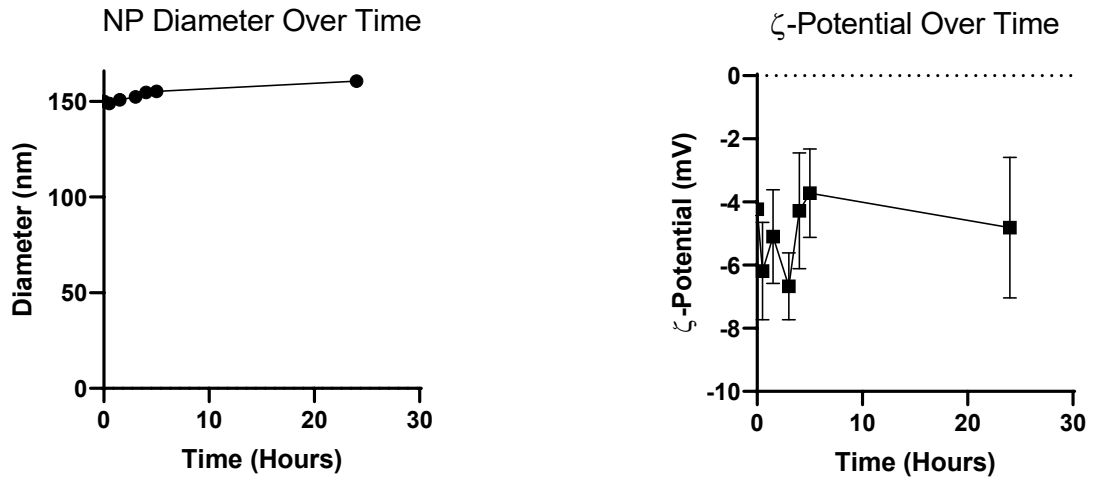

Figure 11 Supplemental Figure 3: *100 nm PSPEGRf/D=4.9 Stability Formulation Stability over Time in EGM-2.* **A)** Dynamic Light Scattering (DLS) measurement of PEGylated NP diameter and **B)** Phase Analysis Light Scattering (PALS) measurement of NP ζ – potential over 24 hours. (n=5)

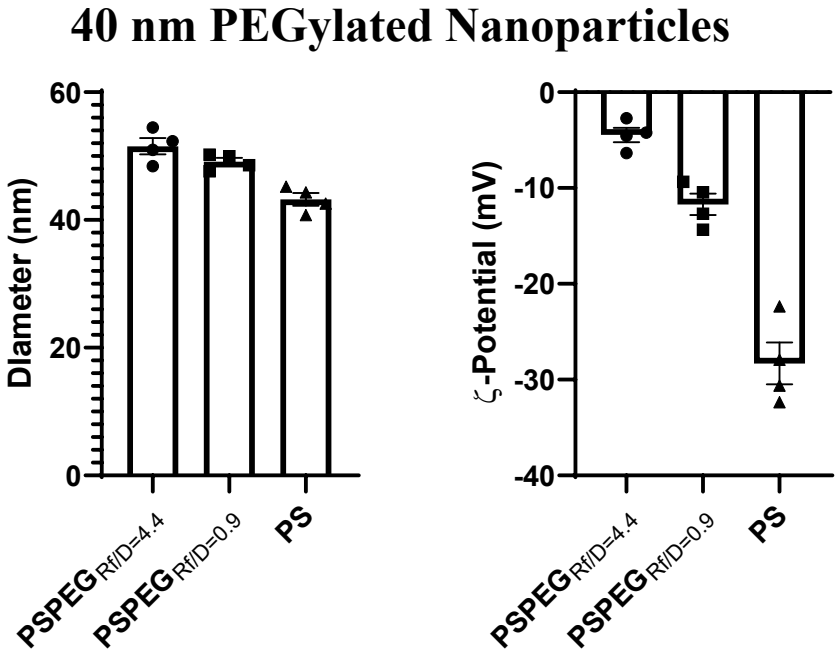

Figure 10 Supplemental Figure 4: 40 nm PSPEG Formulation: **A)** Dynamic Light Scattering (DLS) measurement of PEGylated NP diameter and **B)** Phase Analysis Light Scattering (PALS) measurement of NP ζ – potential. Data shown as mean ± SEM (n = 4)

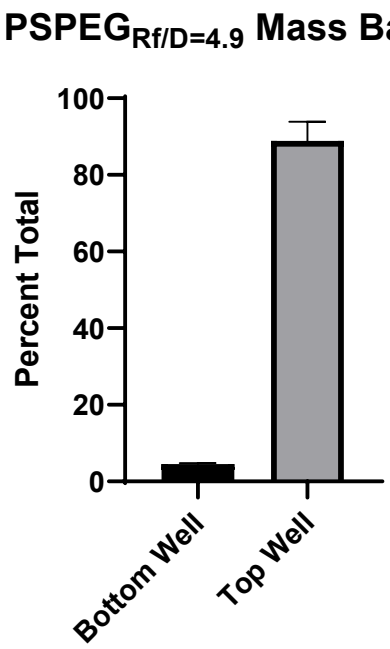

Figure 13 Supplemental Figure 5 Mass balance of nanoparticles in transport assay 24 hrs.

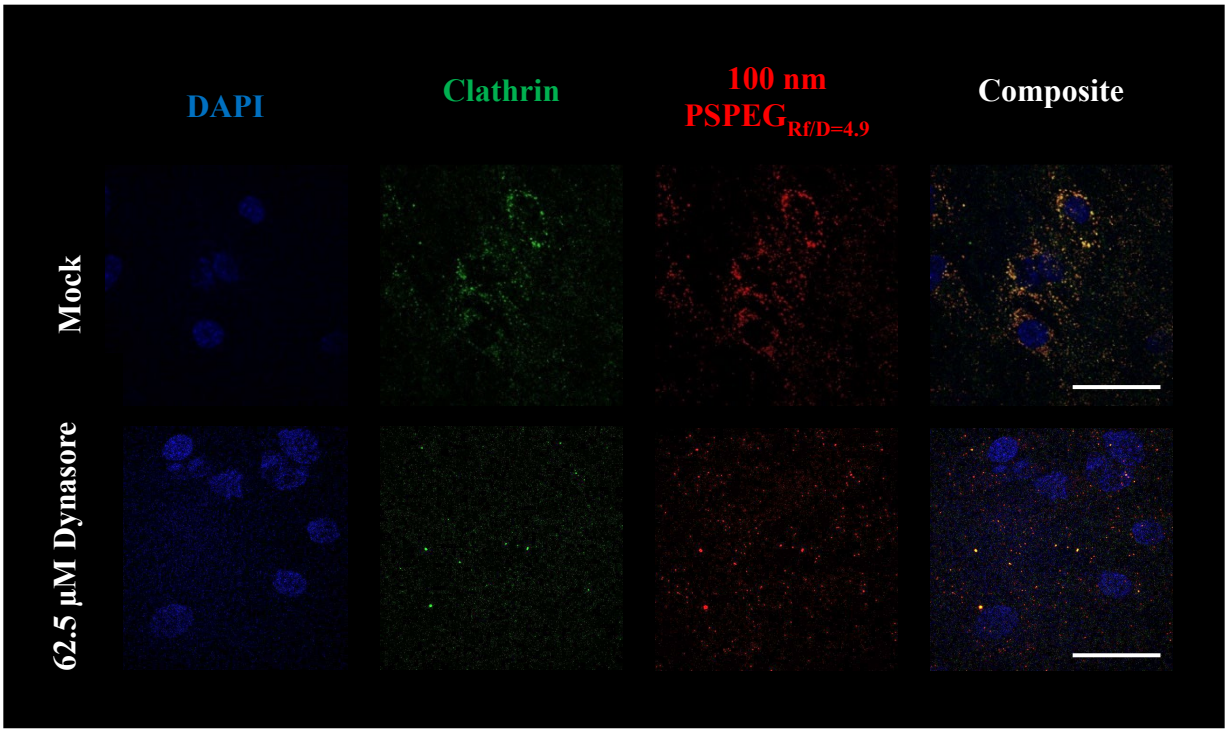

Figure 12 Supplemental Figure 6 Confocal fluorescence image of PSPEGRf/D=4.9 within LECs treated with the vehicle control and of PSPEGRf/D=4.9 within LECs treated with Dynasore. Scale bar: 30 µm. (n = 3-4)

3.4 Discussion

In this work, we investigated the effects of PEG surface density on nanoparticle transport across lymphatics. We found that in vitro, addition of any amount of PEG to nanoparticle surfaces increased their transport across lymphatics compared to hydrophobic nanoparticles, and a "dense brush" of PEG ($R_f/D > 4$) on nanoparticles maximized this transport. Grafting charge-functionalized PEG on the nanoparticle surface, we also identified that neutrally PEGylated nanoparticles were transported most efficiently across LEC barriers compared to negatively charged and positively charged PEGylated nanoparticles. We further found that densely PEGylated nanoparticles were more effectively transported to skin-draining LNs after intradermal injection compared to nanoparticles with lower or no PEG coating. Finally, we found that macropinocytosis, micropinocytosis, and paracellular transport mechanisms mediated transport of PEGylated nanoparticles across lymphatics, but that macropinocytosis did not occur in all PEG conformations. In summary, we identified that "dense brush" PEG coatings maximize nanoparticle transport into the lymphatics and thus the down-stream LNs.

PEG has been used to modulate nanoparticle transport across endothelial barriers, including blood endothelium, lymphatic endothelium, and the blood-brain barrier. Generally, PEG has been shown to enhance systemic circulation and blood endothelium needs to be targeted using additional vectors such as ICAM1 or sugars that target specific ligands on the blood endothelium [103, 104]. This is likely due to the high flow rates in blood vessels that cause nanoparticles not to come into close contact with endothelial cells for long enough to allow uptake and transport across the endothelium [105, 106]. A recent study used 100 nm poly(lactic acid)-PEG nanoparticles with surface PEG ranging from 1 – 10 kDa to probe the effects of PEG MW on transcytosis across brain vascular endothelial monolayers [107]. PEG density on the surface of the nanoparticles was

maintained at 17-20 PEG/100nm^2. It was found that the higher molecular weight PEG polymers displayed improved transport across the monolayers, with 60% translocation efficiency of nanoparticles coated with 5 kDa and 10 kDa MW PEG and only 20% translocation efficiency of nanoparticles coated with 1 kDa PEG. Interestingly, the maintained PEG density translates to $R_f/D > 2$ for nanoparticles coated with 5 kDa and 10 kDa, while $R_f/D < 1$ for 1 kDa coated nanoparticles, indicating that PEG on 1kDa nanoparticles was in mushroom conformation, while PEG was in brush conformation for 5 kDa and 10 kDa nanoparticles. Another study by Rabanel et al suggested that 5kDa PEG coatings increased uptake of nanoparticles into brain endothelial cells, but PEG MW did not have any effect on transport across them [108]. Kim et al demonstrated that PEGylating ionizable lipid nanoparticles reduced their uptake in the liver [109]. They hypothesized that this was due to reduced ApoE protein on the nanoparticle surface, which is one of the key mechanisms that leads to nanoparticle uptake in the liver. Additionally, work by Williams et al showed that PEG enhanced kidney accumulation of nanoparticles and that this was likely due to endocytosis of nanoparticles by the peritubular endothelium [110]. Our findings showed that PEGylation enhances nanoparticle transport across LECs, suggesting that the type of endothelium and other factors such as contact time can affect whether PEG improves transendothelial transport of nanoparticles. For transport into lymphatic vessels, our findings that PEG enhances nanoparticle transport across lymphatics are corroborated by prior work indicating that nanoparticles and liposomes with PEG coatings (with undefined PEG densities) transport effectively to the LNs. Collectively, these results run counter to the traditional motivation of adding PEG to the surface of nanoparticles in that instead of preventing uptake, PEG seems to assist in transcellular transport mechanisms. The mechanism as to why this occurs is being investigated, it is likely that it has to do with PEG effects on the proteins adsorbing on the surface of nanoparticles and the changes in

surface stiffness of PEGylated nanoparticles compared to non-PEGylated nanoparticles. Our work adds an additional layer of understanding that a high PEG density maximizes this transport [38, 41-44, 46].

Surface PEG conformation on nanoparticles has been shown to affect nanoparticle uptake by cells [111]. Several studies have shown that as PEG density increases on nanoparticles, uptake by macrophages and dendritic cells [112-117], as well as cancer cells [112, 118], is reduced. PEGylation appears to have differing results depending on the cell type – PEGylation reduces nanoparticle uptake by macrophages and dendritic cells, as indicated by studies demonstrating that PEG needed to be in a brush conformation to evade uptake and clearance by macrophages [116]. However, addition of PEG to the surface of nanoparticles increased their uptake by neutrophils [97] and several cancer cell types (HeLA, MDA-MB231, VK2) [112, 119]. Interestingly, several studies suggest that changes in protein corona on nanoparticle surface with changing PEG density may in part be responsible for modulating cellular uptake [111, 112, 114, 118]. One study demonstrated that without a protein corona, some PEG, but not high density/MW PEG, could increase uptake by prostate cancer cells compared to no PEG, and without protein, no PEG was optimal [118]. Another study demonstrated that a double layer of PEG, with a second layer having a mushroom conformation (low density of PEG, $R_f/D < 1.5$) reduced protein binding affinity but not total protein binding on the nanoparticle surface. They found that this second layer of PEG reduced nanoparticle uptake by liver sinusoidal endothelial cells [111]. In our studies, we found that PEG density did not affect nanoparticle uptake by LECs, and that it only modulated nanoparticle transport across LECs (**Table 1**). The non-phagocytic nature of LECs may account for some of these differences. Additionally, we are currently investigating effects of the protein

corona on nanoparticle transport across lymphatics, as changes in protein corona appear to be strongly linked with differential uptake and transport of nanoparticles.

Nanoparticle transport across biological barriers, like the endothelium, has been shown to be governed by macro- and micropinocytosis, as well as paracellular transport mechanisms. Studies have shown that larger nanoparticles (>200 nm in size) are transported across cellular barriers via macropinocytosis, while smaller nanoparticles are often transported by various mechanisms of micropinocytosis. Here, we found that densely PEGylated 130 nm nanoparticles are transported via micropinocytosis, likely clathrin-mediated endocytosis, and paracellular transport routes across LECs. This is consistent with prior studies showing that albumin, a 10 nm globular nanoparticle-like protein, is transported across lymphatics via both clathrin- and caveolin-mediated, as well as paracellular transport mechanisms. Additionally, researchers have demonstrated that macro- and micropinocytosis are involved in transport across endothelial cells in tumors and the blood brain barrier [120-126]. Rabanel et al demonstrated that nanoparticles coated with 5 kDa PEG were taken up primarily via macropinocytosis pathways in brain endothelial cells [108]. Tehrani et al found that inhibiting micropinocytosis reduced transcytosis across brain endothelial cells by 60% for 5 kDa PEG-coated nanoparticles, while transcytosis of 2 kDa PEG-coated nanoparticles was reduced only by 25% after inhibiting micropinocytosis [107]. These findings suggest that nanoparticle uptake and transcytosis pathways may differ with different MW and density of PEG, corroborating our findings. A study aiming to improve the circulating time of nanoparticles found that maintaining PEG surface conformation within the intermediate brush domain prevented non-Kupffer cell uptake in the liver. They observed that these intermediately PEGylated nanoparticles were the least preferentially taken up by endothelial cells, accounting for the improved circulation times, and the densely PEGylated nanoparticles were

taken up at higher rates [111]. Additionally, studies have demonstrated that nanoparticle transport across brain microvascular endothelium can be enhanced by taking advantage of existing receptor-mediated transcytosis, such as that of albumin (clathrin/caveolin-dependent) [124, 127-130]. Altogether, a variety of factors appear to influence transendothelial transport mechanisms, and data from the literature and our study suggest that there may be differences in mechanisms depending on the tissue, type of endothelium, and pathological condition [126].

For nanoparticles to reach cells within a tissue, including lymphatic vessels, they need to cross the extracellular matrix (ECM). The ECM forms a hydrogel-like structure composed of fluid, solutes, fibrillar proteins, and proteoglycans, such as collagen. Studies on nanoparticle-ECM interactions have demonstrated that size, shape, and charge are key considerations when designing nanoparticle therapies that need to cross ECM barriers. Large nanoparticles are restricted from crossing the ECM barrier through steric hindrance via the mesh spacing produced by fibers within the ECM. This spacing can become extremely restrictive within tissues. For example, the basement membrane mesh of the subcapsular sinus of the LN forms a tight mesh that prevents molecules larger than 70 kDa from entering the LN via afferent lymphatic vessels [47]. This restrictive barrier can be observed in action in our study here, where IF images of LN slices show nanoparticles sequestered on the edge of the LN, within the subcapsular sinus. One way to overcome this barrier is to utilize multistage and programmable drug delivery platforms. A recent study designed PPS-core nanoparticles coated with PEG that contained tunable thiol-reactive oxanorbornadiene (OND) linked cargo. PEG coating allowed for improved delivery to lymph nodes, while the degradation of the OND-linkages allowed for precise release of cargo within lymph nodes [48]. Restrictive extracellular spacing can be seen in many other tissues, with the spacing often estimated between 20-60 nm in diameter, suggesting that tissues are impermeable to >100 nm sized particles [131].

However, this notion has been challenged recently: Nance et al have demonstrated that particles as large as 114 nm in diameter were able to diffuse within human and rat brain tissue. Indeed, their study highlighted that the pore size within in-vivo ECM is highly heterogenous, with them concluding that within the brain tissue samples, more than one quarter of all pores were >100 nm in diameter [95]. Our studies similarly suggest that skin ECM may be permeable to nanoparticles up to 150 nm in diameter.

Surface chemistry is another key factor affecting nanoparticle transport across ECM barriers. Several studies have demonstrated that nanoparticles with charge opposing that of the fibrous materials of a hydrogel, like ECM, have reduced diffusion within the gel or ECM space [132-136]. Additionally, some studies suggest that repulsive charges can enhance nanoparticle diffusion across ECM barriers compared to attractive charges, but this effect may be minimal [132-136]. Most studies indicate that neutral charge leads to the highest diffusion of nanoparticles across ECM [95, 134, 136], suggesting that PEGylating nanoparticles as we have done in our studies also enhances their transport across ECM. However, fewer studies have assessed how PEG density affects nanoparticle transport across the ECM. One study found that increased PEG density can enhance nanoparticle diffusion through collagen-based ECM materials [137], but this was not recapitulated in matrigel-based gels. Furthermore in this study, PEG density changes are a result of using PEG chains with different molecular weights (MW), which could also affect diffusion, e.g., due to entanglement with ECM chains for larger MWs. Another study has demonstrated that increasing PEG density enhanced liposome diffusion in collagen-based ECM hydrogels [138], and similarly previous work has shown that dense PEG coatings enhanced nanoparticle diffusion through brain ECM [95]. In our studies here, we show that PEG density modulates nanoparticle

transport to the LNs, which may be due to both reduced transport across LECs as well as ECM, based on these existing studies, and is a current topic of investigation in our lab.

In summary, our study demonstrates that the addition of PEG to the surface of hydrophobic nanoparticles, particularly as dense PEG coatings ($R_f/D > 4$), enhances nanoparticle transport into lymphatic vessels. Our results are consistent with prior work demonstrating that PEG enhances uptake and transport across other endothelial barriers as well as the cellular mechanisms involved in this transport. Our study is the first to directly correlate PEG density and efficiency of lymphatic transport of nanoparticles. Additionally, it is the first to demonstrate that densely PEGylated nanoparticles are transported via both micropinocytosis and paracellular transport mechanisms, but not macropinocytosis, by LECs. Furthermore, we demonstrated that PEG density and size can affect the cellular mechanisms used to transport nanoparticles across lymphatic barriers. Thus, our work highlights that dense PEG coatings are the optimal strategy to formulate nanoparticles that maximize transport across lymphatics and to the LNs. Our work also sheds new light onto the effects of PEG density on cellular mechanisms of nanoparticle transport. Our findings are particularly crucial for future development of immune modulatory therapeutic strategies.

4 Para- and transcellular transport kinetics of nanoparticles across LECs

This article is being reviewed for publication:

Jacob McCright, Jenny Yarmovsky, Katharina Maisel, bioRxiv 2023.04.12.536598; doi: https://doi.org/10.1101/2023.04.12.536598

4.1 Introduction

Nanoparticle-based drug delivery has received significant attention in past decades, culminating in the recent COVID-19 lipid nanoparticle-based RNA vaccines. Nanoparticles provide several advantages to free drug formulations: they can increase drug stability [139] and load [140], be targeted to specific tissues or cells [141], and facilitate sustained release of drugs from the nanoparticle core [142]. To enter the relevant cellular compartments, nanoparticles are required to be transported across various biological barriers, including cell monolayers at the intestinal epithelium or blood and lymphatic endothelium, for example. Nanoparticle transport across these cellular barriers occurs via paracellular or transcellular transport mechanisms. Transcellular transport mechanisms include micropinocytosis, macropinocytosis, and/or exocytosis on both sides of the cell layer (**Figure 14A**), often with concentration gradients driving the dominant direction of the transport. Nanoparticle transport across cellular barriers can be modeled using systems of differential equations utilizing kinetic theories also applied to pharmacokinetic models [143]. A complex system of equations can be used to define the contributions of the individual transport mechanism to the overall transport of nanoparticles (**Equations 1-3**), with nanoparticle concentration within model compartments represented by C, and the rate constants associated with different transport mechanisms represented by k. This system of equations can be applied for transport across any system of single cell layers or other three-compartment models. These

equations can be formulated as follows for the system in **Figure 14A** modeling an endothelial cell barrier:

$$(\mathbf{1}) \qquad \frac{\partial C_1}{\partial t} = -(k_1 + k_2 + k_3)C_1 + k_4 C_3 + k_5 C_2$$

$$(\mathbf{2}) \qquad \frac{\partial C_2}{\partial t} = -(k_5 + k_6)C_2 + (k_1 + k_2)C_1 + (k_7 + k_8)C_3$$

$$(\mathbf{3}) \qquad \frac{\partial C_3}{\partial t} = -(k_4 + k_7 + k_8)C_3 + k_6 C_2 + k_3 C_1$$

Lymphatic vessel-targeted drug delivery has received significant attention in recent years, largely owing to the fact that lymphatic vessels transport nanoparticle-sized materials from the peripheral tissue to the draining lymph nodes, where the adaptive immune response is shaped. Delivering therapeutics that modulate the immune response directly to the lymph nodes has been shown to enhance their efficacy. Nanoparticles 10-250 nm in size have been shown to be preferentially transported by lymphatic vessels and will accumulate effectively in the lymph nodes. Recent studies have shown that both transcellular and paracellular mechanisms are key in nanoparticle entry into lymphatic vessels [35, 144, 145]. Research from our group has shown that the specific transport mechanisms used by LECs are dependent on nanoparticle surface chemistry, specifically PEG density [145]. We found that coating 100 nm nanoparticles with hydrophilic, neutrally charged poly(ethylene glycol) (PEG) leads to nanoparticle transport via both micropinocytosis and paracellular transport. Using computational models to study the kinetics behind these findings can aid in our understanding of how nanoparticle surface chemistry affects transcellular processes [146-151] [152]. Here, we sought to model the kinetics of nanoparticle transport across lymphatic vessels. In this paper, we derive the equations and rate coefficients describing transport kinetics of

nanoparticles, taking into account both transcellular and paracellular mechanisms. Additionally, we use transport data collected experimentally and simplify **Equations 1-3** into a four-part problem of endocytosis, exocytosis, and paracellular transport, with the assumption that transport is driven in the direction of the concentration gradient from the interstitial tissue into the lumen of the vessel (**Figure 14B, Equations 4-6**). The resulting mathematical and computational framework can be used to extrapolate transport kinetics across similar cell layer problems and could be integrated with more complex machine learning-based techniques, like artificial neural networks, to predict the contribution of different transport mechanisms.

$$\mathbf{(4)} \quad \frac{\partial C_1}{\partial t} = -(k_1 + k_3)C_1 + k_2 C_2$$

$$\mathbf{(5)} \quad \frac{\partial C_2}{\partial t} = -(k_2 + k_4)C_2 + k_1 C_1$$

$$\mathbf{(6)} \quad \frac{\partial C_3}{\partial t} = k_3 C_1 + k_4 C_2$$

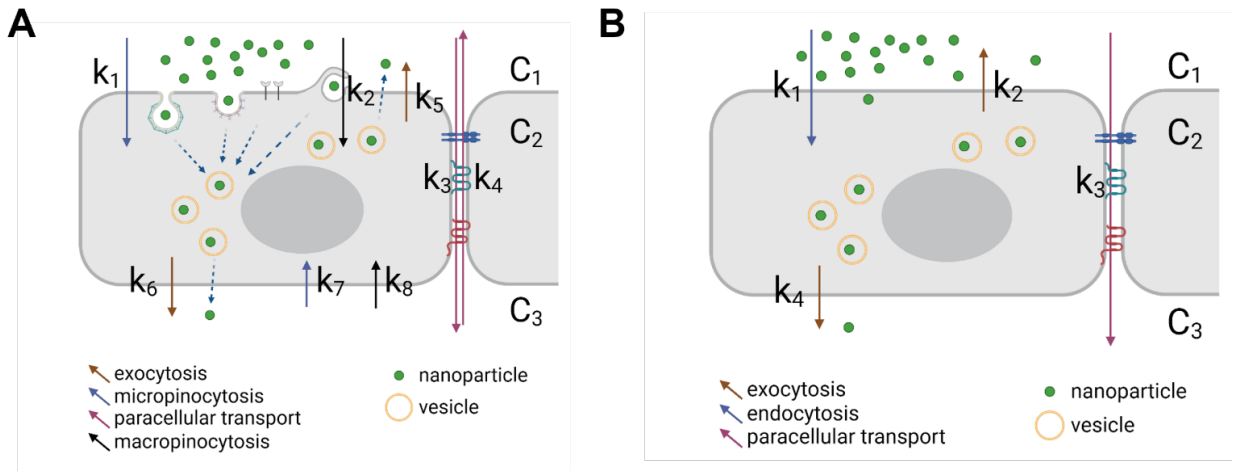

Figure 14 Figure 1: *Cellular mechanisms used to transport nanoparticles across cell barriers such as epithelial surfaces and vessel walls*. **A**) complex transport considering all potential variables and **B**) simplified transport considering only endocytosis, paracellular transport, and exocytosis. Concentrations depict each compartment with C1 = nanoparticle-rich compartment, C2 = intracellular compartment, C3 = nanoparticle-poor compartment. Full arrows and associated k values represent the kinetics of exocytosis (brown), micropinocytosis (blue), macropinocytosis (black), and paracellular transport (pink).

4.2 Methods

4.2.1 Nanoparticle Formulation

Fluorescent carboxyl (COOH)-modified polystyrene (PS) nanoparticles (Thermo Fisher Scientific) were covalently modified with 5 kDa MW methoxy-PEG-amine (NH_2) (Creative PEGworks), as previously described [95]. Nanoparticles with different PEG conformations were generated using previously described methods [153]. Briefly, PS-COOH particles were suspended at 0.1% w/v in 200 mM borate buffer (pH = 8.2). PEG was conjugated to nanoparticles using 7 mM N-Hydroxysulfosuccinimide (NHS) (Sigma) and 0.02 mM 1-Ethyl-3-(3-dimethylaminopropyl) carbodiimide (EDC) (Invitrogen). The reaction was performed on a rotary incubator at room temperature for at least 4 hours. Nanoparticles were collected using 100k MWCO centrifugal filters (Amicon Ultra; Millipore) and washed with deionized (DI) water. Nanoparticles were resuspended at 1% w/v in DI water and stored at 4^{o}C.

4.2.2 Nanoparticle Characterization

Dynamic light scattering (DLS) was used to measure the hydrodynamic diameter and polydispersity index (PDI) of nanoparticles. Phase analysis light scattering (PALS) was used for measuring ζ-potential (NanoBrook Omni). Measurements were performed using a scattering angle of 90^{o} at 25^{o}C. Measurements were based on intensity of reflected light from scattered particles.

4.2.3 PEG Density Characterization

PEG density was determined using a previously published method [97, 153]. Briefly, 5kDa PEG-NH2 (Creative PEGworks) conjugated to fluorescein isothiocyanate (FITC) was conjugated to fluorescent (AlexaFluor®555) 100 nm carboxyl-modified nanoparticles (Creative PEGworks). Using FITC-PEG-NH_2 standards, PEG grafting distance (D) and PEG density were estimated

using the Flory radius of PEG (Rf) based off of fluorescence intensity. The Flory radius of a polymer chain is defined as $Rf \sim \alpha N^{3/5}$, where N is the degree of polymerization, and α is the effective monomer length. An unconstrained 5 kDa PEG chain has an Rf of 5.4 nm and occupies 22.7 nm^2. PEG density and conformation can be correlated to the ratio of Rf/D, with Rf/D < 1-1.5 yielding a mushroom conformation, 1-1.5< Rf/D > 4 yielding a brush conformation, and Rf/D > 4 yielding a dense brush conformation.

4.2.4 Nanoparticle Transport

LEC permeability was assessed using an established in vitro model that recapitulates in vivo lymphatic transport [17]. Briefly, primary human LECs (hLECs, Promocell C-12217) were seeded on 1.0 μm pore size, 12 mm transwell inserts (Falcon) at 200,000 cells/cm2 and cultured in EGM2 (PromoCell) at 37ºC and 5% CO2 for 48 h. Cells were pre-treated with 1 μm/s transmural flow to simulate the interstitial fluid flow experienced in the tissue microenvironment. hLECs were treated with 10 ug/mL nanoparticles in the top compartment and both top and bottom compartment were sampled every 1 h for up to 24 h. Fluorescence intensity was measured using a plate reader (Tecan) and nanoparticles transported was calculated using a standard curve. Transport experiments were performed in EGM2 without growth factors to avoid confounding effects of growth factors on transport mechanisms. To probe transport mechanism, the following transport inhibitors were used: 100 nM Adrenomedullin (Abcam ab276417), 62.5 μM Dynasore (Sigma D7693), or 62.5 μM Amiloride (Sigma A7410). Transport inhibitors were applied 2 hours prior to introduction of nanoparticles. LEC monolayer integrity was confirmed after experiments using immunofluorescence.

4.2.5 Computational Model Solving

Equations 1-3 were generated to model the three-compartment model of nanoparticle transport across LECs (**Figure 1A**). The following assumptions were made to simplify the model 1) Transport between cells is unidirectional along the concentration gradient since [C1] >> [C3] (k4 = 0) and 2) Reuptake of nanoparticles from compartment C3 to C2 is negligible (k7, k8 = 0). Under these assumptions, equations 1-3 become equations 4-6 (**Figure 1B**).

Experimental data of C1 and C3 were used to extrapolate C2, assuming that nanoparticle mass and fluorescence was conserved. This data was normalized to C = C/Ctotal. The normalized concentration over time data was used to estimate k parameters using MatLab 'lsqcurvefit' function. Levenberg–Marquardt, or the damped least-squares method, was used to solve the nonlinear least squares optimization problem:

$$\min_x ||F(x, xdata) - ydata||_2^2 = \min_x \sum_i (F(x, xdata_i) - (ydata_i))^2$$

For parameter estimation, k values were constrained to be positive to match the kinetics outlined in equations 4-6 and **Figure 1B**. In the presence of Adrenomedullin, parameter k3 was set to zero, as the addition of Adrenomedullin prevents paracellular transport.

4.3 Results

4.3.1 Transport Efficiency of Nanoparticles Across LECs can be Fitted to a Three-Compartment Kinetic Model

To be able to fully model the transport kinetics within the three compartments (**Figure 15A),** C1 (top compartment, interstitial tissue where nanoparticles are injected), C2 (intracellular), and C3 (bottom compartment, vessel lumen that leads to the lymph nodes), we first collected data on concentration change over time within C1 and C3 (**Figure 15B**). We formulated 40-150 nm PEGylated nanoparticles [95, 153] from unmodified 103 ± 5 nm and 40 ± 2 nm. Addition of PEG increased nanoparticle diameter to 122 ± 6 nm (partial PEG) and 142 ± 3 nm (dense PEG), and 43 ± 2 nm (partial PEG) and 49 ± 3 nm (dense PEG). Pegylated nanoparticles also displayed a near-neutral ζ – potential. Using these nanoparticles, we found that C1 was reduced to 60-70% of the initial nanoparticle concentration placed in the top well, after which C1 increased again when nanoparticles were exocytosed into the top compartment (**Figure 15B**). We also confirmed that densely PEGylated nanoparticles were transported the most efficiently compared to partially PEGylated nanoparticles, with 5.3 ± 0.2% nanoparticles transported into C3 for densely PEGylated 100 nm nanoparticles, compared to 4.1 ± 0.2% for partially PEGylated nanoparticles (**Figure 15B**). Similarly, 40 nm densely PEGylated nanoparticles had 7.9 ± 0.5% of nanoparticles transported into C3, compared to 5.5 ± 0.2% for the partially PEGylated nanoparticles (**Figure 15B**).

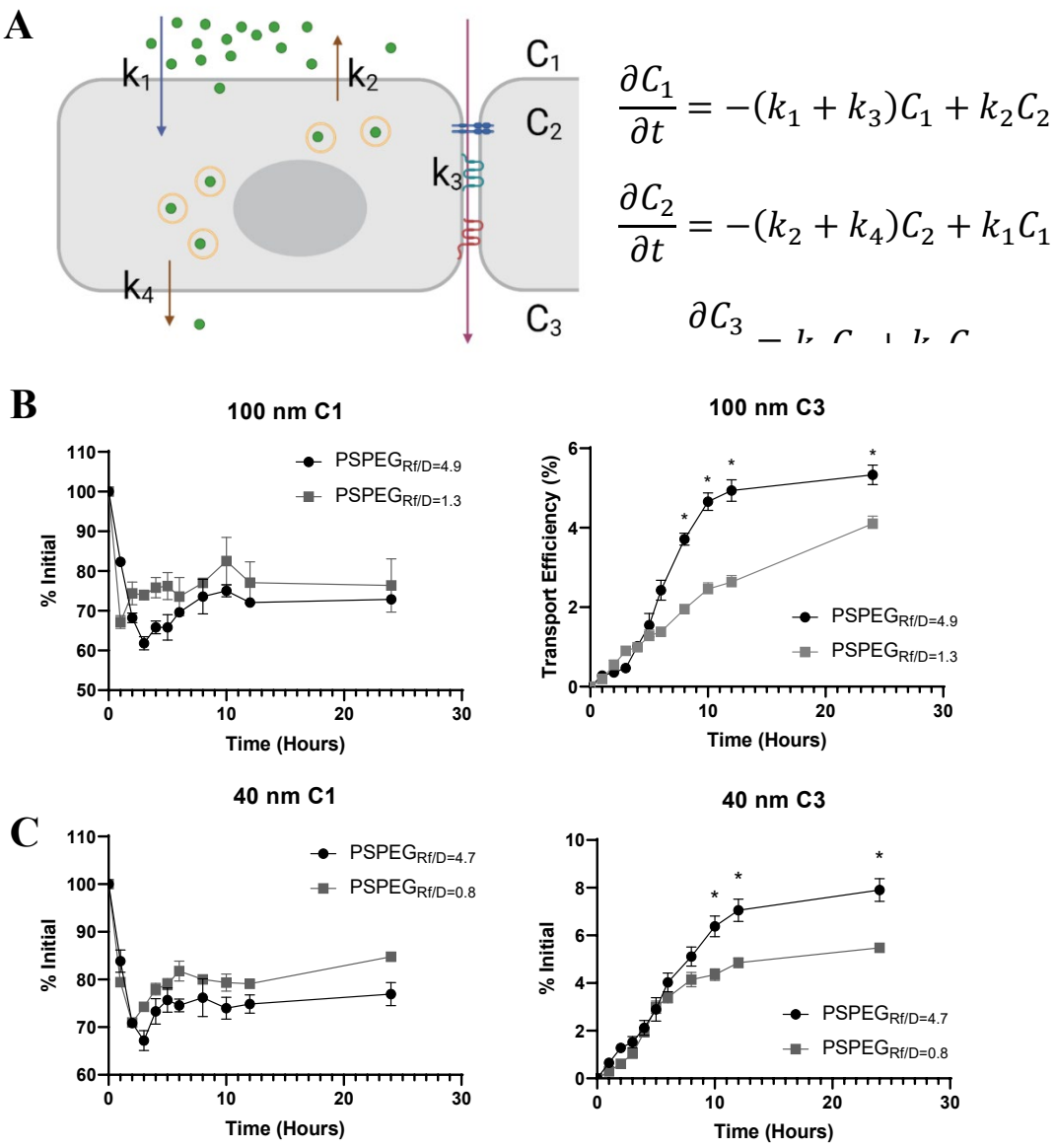

Figure 15 *PEG Coating Improves Transport of 100 and 40 nm NP Across LECs.* A) Schematic of the transport model and associated differential equations. B) Percent of 100 nm fully PEGylated (PSPEGRf/D=4.9) and partially PEGylated NP (PSPEGRf/D=1.3) in the top compartment and transported across LEC monolayer over time. C) Percent of 40 nm NP fully PEGylated (PSPEGRf/D=4.7) and partially PEGylated NP (PSPEGRf/D=0.8) in the top compartment and transported across LEC monolayer over time. Data presented as mean ± SEM (*p<0.05)

estimate the kinetics (k) parameters in the system of differential equations (**Table 2**). Based on these k values, we can see that the initial uptake and release of nanoparticle at the top compartment interface (k1 and k2) is the dominant reaction, indicated by the order of magnitude difference compared to k3 and k4. Another trend to note is that k3, describing paracellular transport, is the smallest parameter. This indicates that cellular mechanisms, including endocytosis and micropinocytosis are driving nanoparticle transport across LEC barriers. Importantly, transport trends with respect to formulation are captured within the model. k4, a key parameter for measuring the transport of nanoparticles into the simulated vessel, increases from 0.13 $\mu g\ mL^{-1}\ hr^{-1}$ for the larger 100 nm $PSPEG_{Rf/D=4.9}$ nanoparticles to 0.26 $\mu g\ mL^{-1}\ hr^{-1}$ for the smaller 40 nm $PSPEG_{Rf/D=4.7}$ nanoparticles.

Rate Constants ($\mu g\ mL^{-1}\ hr^{-1}$)	100 nm $PSPEG_{Rf/D=4.9}$	100 nm $PSPEG_{Rf/D=1.3}$	40 nm $PSPEG_{Rf/D=4.7}$	40 nm $PSPEG_{Rf/D=0.8}$
k1	1.9	1.5	1.5	1.2
k2	3.9	3.5	4.0	3.2
k3	0.013	0.012	0.014	0.011
k4	0.13	0.074	0.26	0.21

Table 2 Calculated K values of system of differential equations describing nanoparticle transport across LECs for different nanoparticle formulations.

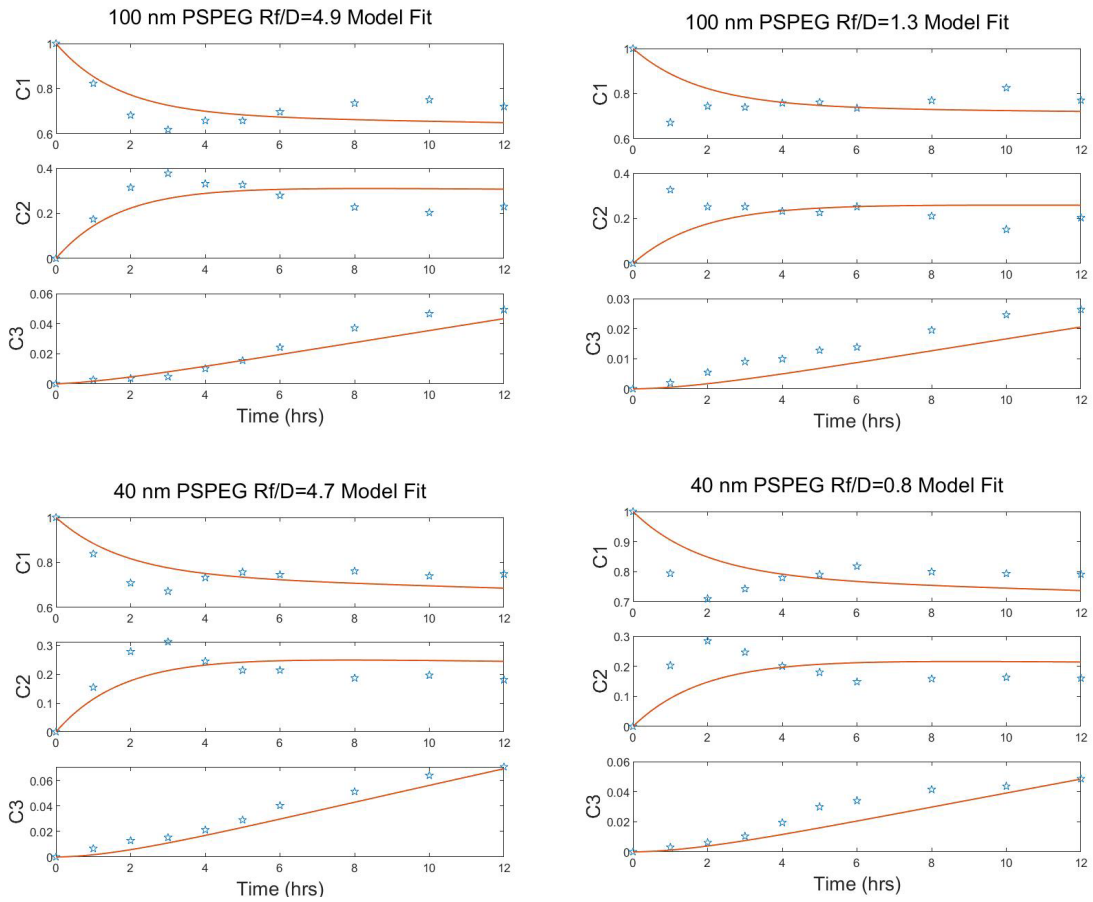

Figure 16 *Nanoparticle Transport Across LECs can be Modeled With our Three Compartment Kinetic Model* Normalized experimental concentration data (stars) fitted against system of differential equations (solid line).

4.3.2 Size and surface chemistry of nanoparticles affect their transport via macropinocytosis across LECs

Next, we investigated how the kinetics changed for different cellular transport mechanisms. Again, we used partially and densely PEGylated, 40 – 150 nm nanoparticles. As in our prior study, we found that 100 nm densely PEGylated nanoparticles were not transported by macropinocytosis but that both paracellular and transcellular transport were involved, indicated by reduced transport upon introduction of transport inhibitors (**Figure 17A**). Interestingly, for partially PEGylated nanoparticles, all transport mechanisms were involved in nanoparticle accumulation in C3 (**Figure 17A**). The introduction of transport inhibitors generally reduced the depletion of nanoparticles from C1: for both 100 nm $PSPEG_{Rf/D=4.9}$ and $PSPEG_{Rf/D=1.3,}$ inhibiting micropinocytosis reduced this phenomenon the greatest, albeit not significantly different (**Figure 17**).

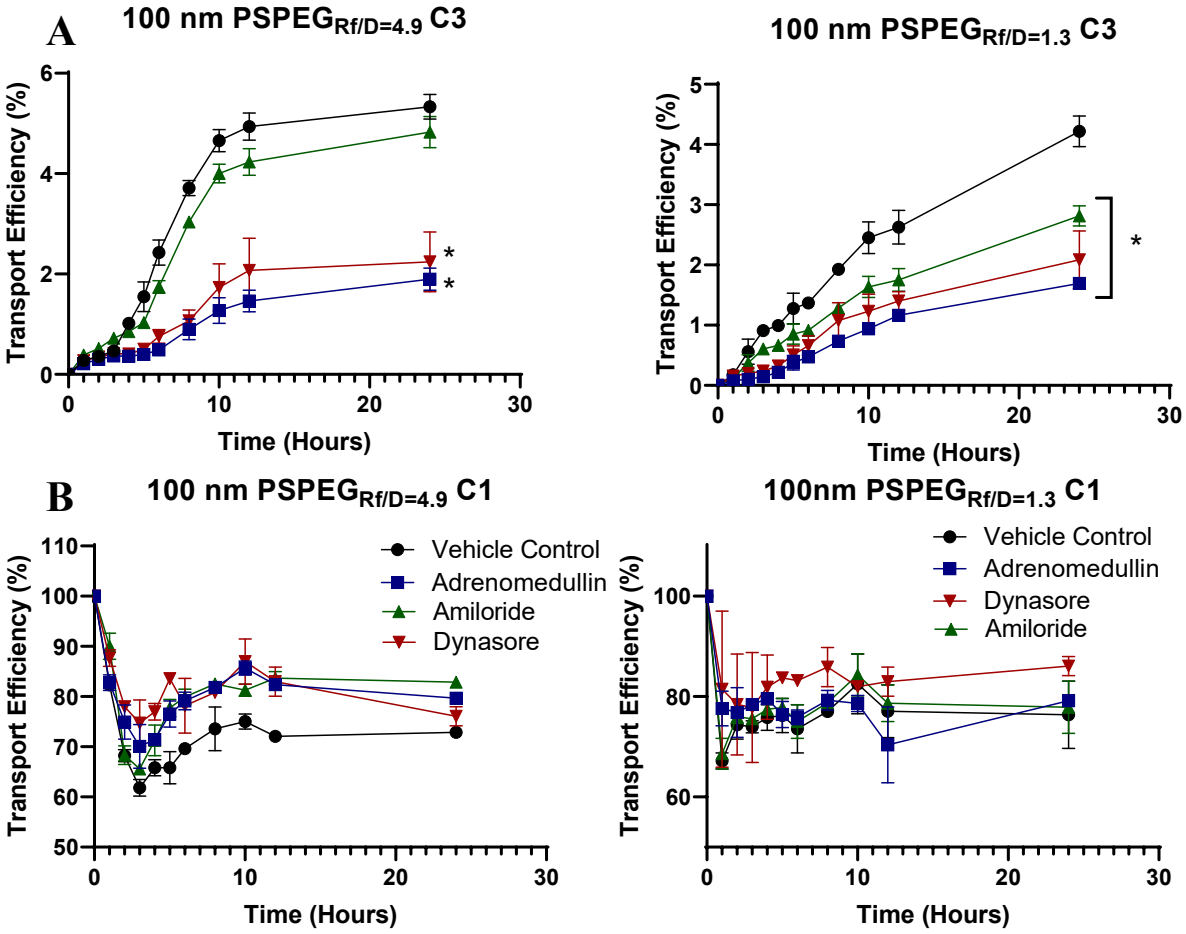

Figure 17 *Kinetic Model Captures Transport Mechanisms Governing NP Transport Across LECs.* Percent transport of 100 nm fully PEGylated (PSPEGRf/D=4.9) and partially PEGylated NP (PSPEGRf/D=1.3) in the (A) bottom (C3) and (B) top (C1) compartments in the presence of transport inhibitors. Data presented as mean ± SEM (*p<0.05) n = 2-4

This transport data including transport inhibitors was then incorporated into our three-compartment kinetic model and fitted to the system of differential equations using a non-linear, least-squares, curve fitting algorithm, resulting in curve fitting (**Figure 17C-D**). Solved parameters k for equations with respect to nanoparticle formulation can be found in **Tables 3-4**. From these k values, we can see trends in the presence of inhibitors similar to the control transport experiments: For both densely and partially PEGylated nanoparticles, k1 and k2 (uptake and re-release of nanoparticles into C1) are larger than k3 and k4 (transcellular and paracellular transport of nanoparticles into C3).

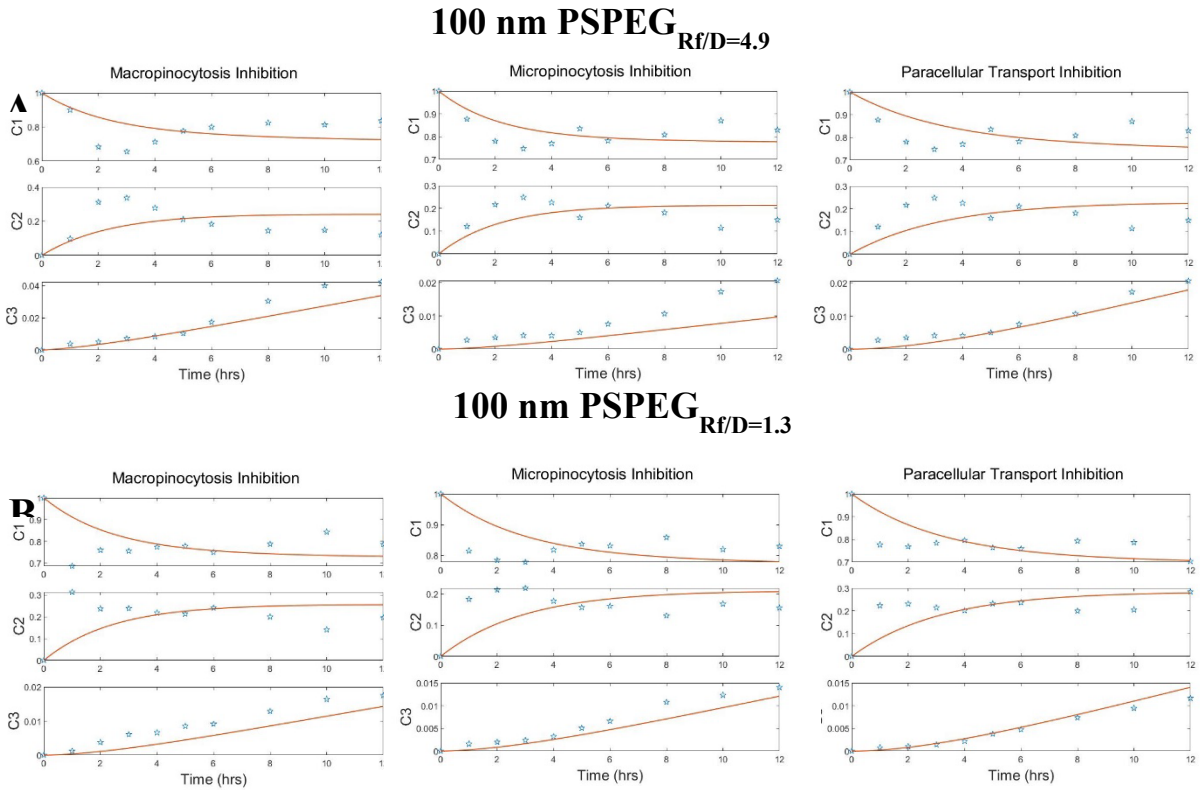

Figure 18 *Kinetic Model Captures Transport Mechanisms Governing NP Transport Across LECs.* Percent transport of 100 nm fully PEGylated (PSPEGRf/D=4.9) and partially PEGylated NP (PSPEGRf/D=1.3) in the presence of transport inhibitors. Normalized experimental concentration data (stars) fitted against system of differential equations (solid line) including different transport inhibitors. A) Fully PEGylated 100 nm Rf/D=4.9 nanoparticles, B) Partially PEGylated Rf/D=1.3 nanoparticles

Our computational model captures how the inclusion of transport inhibitors affects mechanisms used for transport. Removing paracellular transport resulted in an increase in k1 for partially PEGylated nanoparticles. When micropinocytosis was inhibited, k1 dropped from 1.9 to 1.0 μg mL^{-1} hr^{-1} and 1.5 to 0.7 μg mL^{-1} hr^{-1} for densely and partially PEGylated 100 nm nanoparticles, respectively. k3, which represents paracellular transport, in contrast increased nearly 10-fold, suggesting that an increased concentration gradient drives more nanoparticles across LECs via paracellular transport. Even though our experimental data suggests that inhibition of macropinocytosis does not significantly modulate densely PEGylated, 100nm nanoparticle transport across LECs, our computational data shows a reduction in k1 upon treatment with amiloride from 1.9 to 1.2, suggestive of the complex relationship between the regulation of different transcellular transport mechanisms that exist in biological systems.

Table 3 Calculated k values of system of differential equations describing transport of 100 nm PSPEGRf/D=4.9 across LECs in the presence of different transport inhibitors.

Rate Constants	**100 nm $PSPEG_{Rf/D=4.9}$**	**+Amiloride**	**+Dynasore**	**+Adrenomedullin**
k1	0.19	0.12	0.10	0.070
k2	0.39	0.30	0.36	0.22
k3	0.0013	0.002	0.02	0
k4	0.013	0.010	0.0041	0.0088

Rate Constants	**100 nm $PSPEG_{Rf/D=1.3}$**	**+Amiloride**	**+Dynasore**	**+Adrenomedullin**
k1	0.15	0.10	0.07	0.090
k2	0.35	0.28	0.26	0.22
k3	0.00012	0.001	0.02	0
k4	0.0074	0.010	0.0057	0.0055

Table 4 Calculated k values of system of differential equations describing transport of 100 nm PSPEGRf/D=1.3 across LECs in the presence of different transport inhibitors.

4.4 Discussion

In this study we probed how nanoparticle formulation parameters, including size and surface chemistry, influenced both the transport efficiency and transport mechanism into lymphatic vessels. We found that increasing the density of PEG on the surface of nanoparticles improved transport efficiency, with maximal transport efficiency occurring with the smaller, 40 nm densely PEGylated nanoparticles. We also observed that nanoparticle transport mechanism is dependent on formulation, notably that macropinocytosis does not drive transport for the 100 nm fully PEGylated nanoparticles as it does for other formulations. Using these experimental results, we fitted our data into a set of differential equations describing the three-compartment problem including endocytosis, exocytosis, and paracellular transport. This computational framework produced parameters to describe transport kinetics and allow for the quantitative analysis of driving mechanisms of transport and formulation parameters.

Lymphatic vessels exist throughout the entire body and are known for transporting cells, fluid, and particulates from peripheral tissues to the local draining lymph nodes, where the adaptive immune response is formed. Lymphatics are important drug delivery targets as they transport immune modulatory therapies to the lymph nodes and improve vaccine and immunotherapy efficacy [3]. A study from Triacca et al provided some of the preliminary evidence that LECs themselves serve as significant barriers todelivery into lymphatic vessels [17]. Developing the in vitro lymphatic transport model that is also used in this study, they demonstrated that when micropinocytosis was inhibited with Dynasore, transport efficiency of albumin and dextran across the LECs decreased significantly – a clear indication that LECs serve as barriers. We also recently demonstrated first insights on the transport mechanisms involved in the transport of nanoparticles across lymphatic barriers. We found that both paracellular and transcellular transport mechanisms were key in

crossing lymphatic barriers, with LECs relying on clathrin-mediated endocytosis to mediate transport of PEGylated nanoparticles [153]. Our current study is an extension of this work, demonstrating that macropinocytosis, in particular, is affected by both size and surface chemistry. Others have demonstrated that macro- and micropinocytosis are involved in nanoparticle transport across endothelial cells in tumors and the blood brain barrier [120-126]. Rabanel et al demonstrated that nanoparticles coated with 5 kDa PEG were taken up primarily via macropinocytosis pathways in brain endothelial cells [108]. Tehrani et al found that inhibiting micropinocytosis reduced transcytosis across brain endothelial cells by 60% for 5 kDa PEG-coated nanoparticles, while transcytosis of 2 kDa PEG-coated nanoparticles was reduced only by 25% after inhibiting micropinocytosis [107]. These findings suggest that endocytosis drives nanoparticle uptake and that transcytosis pathways may differ with nanoparticle size and different amounts and density of PEG, corroborating the results in this study. Additionally, studies have demonstrated that nanoparticle transport across brain microvascular endothelium can be enhanced by taking advantage of existing receptor- mediated transcytosis, such as that of albumin (clathrin/caveolin-dependent) [124, 127-130].

Computational methods and frameworks to model drug delivery into tissues and across endothelial barriers have been used to study the regulation of nanoparticle transport and to guide nanoparticle design to target tissues of interest. One of the key considerations when applying a computational model to physiological phenomena is deciding what type of model to employ. In our study, we generated a three-compartment model of the lymphatic endothelium and used the Levenberg–Marquardt algorithm for parameter estimation to solve our non-linear least squares parameter optimization problem for our system of ODEs. This algorithm was used as it is more robust than the more common Gauss-Newton algorithm, especially when the data is not well-behaved or the

starting parameters are far from the solution parameters, as is often the case when modeling physiological data. [154] Saqlain et al endeavored to model levodopa concentration in the brains of Alzheimer's patients using a classical system of ODEs and a novel approach using stochastic differential equations[155]. They found that the stochastic model better fit the physiological data. This shift to stochastic modeling has correlated with the emergence of neural network-based and artificial intelligence-based modeling for drug delivery[156]. Lu et al employed a novel neural-ODE system to predict T-DM1 conjugate concentration in patients based on patient characteristics (age, sex, race, height, weight, region) and dosing regimen[157]. They validated the implementation of the neural-ODE system against lightGBM and LSTM methods for predicting pharmacokinetics and found that their neural-ODE system better recapitulated the clinical data compared to traditional models. Cattaneo and Zunino generated a computational model based on fundamental filtration and transport to model the interplay between blood perfusion, fluid exchange with the interstitial volume, mass transport in the capillary bed, and transport through the capillary walls and into the surrounding tissue at the microscale level[158]. In their work, they solved for the transport of small molecule drugs and nanoparticles from capillaries into surrounding tumor spaces. Using this model, they were able to quantitatively demonstrate that using nanoparticle intermediaries for drug delivery was an optimal delivery strategy compared to bolus injection of free drug in the tumor site. Groh et al also employed a computational model to examine drug transport into tumors [151]. In this study they simulated solid tumors, and through the solving of their computational model, were able to identify key pharmacokinetic parameters that govern how far model drugs penetrate model tumors.

In addition to computational modeling of drug delivery on the larger tissue level, studies have also sought to model drug and nanoparticle transport across, and interactions with, cells and cell layers.

Wei-Chun Chou et al developed a pharmacokinetic model to examine gold nanoparticle kinetics in rat models. Through the development of their model, they examined how size affected kinetics[159]. Interestingly, based on their physiological data, they were able to modify a classical pharmacokinetic modeling framework to hypothesize nanoparticle-specific pathways and kinetics with respect to size. While their model focused on uptake and clearance of nanoparticles at the organ scale, formation of their model indicated that classical approaches employed for small molecule pharmacokinetic modeling did not translate to nanoparticle modeling and that administration route-specific data and modeling is needed to improve approaches to modeling nanoparticle pharmacokinetics. A key consideration from their study is that the lymphatics and lymph nodes were not included in their model, highlighting the gap in knowledge regarding nanoparticle pharmacokinetics in these key tissues. A recent paper from Khan et al employed a similar transwell-based model as outlined in our study [152]. They generated a three-compartment model and fitted observed transport data to a system of kinematic equations to solve for the transport coefficients governing their model. This study highlighted how artificial neural networks (ANNs) can be used as a method to statistically model and solve kinematic transport equations similar to the ones set forth in our study. In their model, they observed a steady accumulation of nanoparticle within the intracellular compartment, in contrast to the rapid uptake and release observed in our model. Collectively, these studies demonstrate the utility of computational models and how they can be employed to better understand how the transport of key agents in tissues of interest is regulated. Our work builds on these concepts by using computational methods to examine what mechanisms are driving transport, as well as using these methods to quantitatively describe how formulation parameters can affect transport efficiency.

One of the interesting findings from our study is the nanoparticle uptake and release back into the top well. This phenomenon has been observed in other studies, including one by Georgieva et al, that showed how caveolin-mediated uptake of nanoparticles by endothelial cells peaked at 30 min before release back into the environment [160]. This relatively rapid uptake and release of nanoparticles is similar to what occurred in our study, reinforcing that endocytosis pathways are key when examining nanoparticle transport. Another study from Fiorentino et al observed a similar phenomenon where 20-100 nm PS nanoparticles were rapidly taken up by blood outgrowth endothelial cells and released back into cell culture within four hours. Furthermore, they observed that nanoparticles localized with caveolin and that inhibiting endocytotic pathways with chemical inhibitors, including Dynasore, prevented nanoparticle uptake [161]. This endocytosis-mediated uptake and translocation of nanoparticles is similarly observed in our study, with the administration of the micropinocytosis inhibitor Dynasore decreasing the rapid uptake of nanoparticles seen in untreated controls. Rapid uptake and release of nanoparticles has been observed in a variety of cell types, including epithelial cells, fibroblasts, and macrophages [162-165].

5 Extracellular Cues and Nanoparticle Shape Influence Transport Mechanism and Efficiency Across Lymphatics

5.1 Introduction

Lymphatics exist throughout the body and are appreciated for the transport of materials to the lymph nodes where immune responses are formed. This has caused lymphatic vessels to become potential drug delivery targets to transport immune modulatory therapies to the LNs without requiring direct injections. Delivering immunotherapies, including vaccines, to the LNs has been shown to potentiate their therapeutic effects, particularly crucial as efficacy of many immunotherapies still requires improvement. Recent studies have demonstrated that nanoparticles between 10 - 250 nm in diameter are transported preferentially via lymphatic vessels from peripheral tissues to LNs, highlighting that the transport functions of lymphatics can be taken advantage of for drug delivery [1, 2]. Additionally, studies outlined earlier in this thesis have identified the key nanoparticle surface chemistry required for transport across lymphatics, and the mechanisms governing lymphatic transport: nanoparticles with PEG in a dense brush conformation on the surface of nanoparticles utilize both transcytosis and paracellular transport mechanisms. Interestingly, we have observed that densely PEGylated nanoparticles do not rely on macropinocytosis to cross lymphatic barriers. This change in transport mechanism could be the result of changes in the protein corona formed on nanoparticles in a formulation dependent manner [111, 118, 166]. In addition to protein corona formation, other key physiological phenomena like transmural flow have been shown to affect lymphatic physiology and transport, and needs to be incorporated into our models to better recapitulate in-vivo conditions within our transport model. While we have identified key formulation parameters including size, charge, and surface chemistry that facilitate lymphatic transport, there remains a need to understand how the lymphatic

environment *in-vivo* can affect lymphatic transport, critically, 1) the formation of the protein corona on nanoparticle surface post injection, and 2) the effect that physiological interstitial flow has on lymphatic transport.

When nanoparticles and other foreign materials enter biological environments, the surrounding molecules and proteins quickly adhere onto the surface creating a protein corona. This adsorption has been demonstrated to influence drug delivery applications of nanoparticles. Some studies have demonstrated that the formation of protein corona on the surface of nanoparticles can hinder nanoparticle transport across endothelial and epithelial barriers by blocking nanoparticle interactions with the cell membrane [167, 168]. However, many other studies have indicated that the formation of protein corona on the surface of nanoparticles can improve transport and uptake of nanoparticles across, especially if protein components are ligands for corresponding receptors on cells of interest. This role of the protein corona with regards to improved nanoparticle transport is of special interest with regards to lymphatics. Albumin, one of the most ubiquitous proteins found in the body, and a common component of the protein adsorbed on foreign material, has been utilized to improve lymphatic transport [169, 170].

Another key consideration for drug delivery into lymphatics is the interstitial fluid flow that continuously drives fluid and material into initial lymphatic capillaries, and on through collecting lymphatic vessels into lymph nodes. Indeed, this interstitial flow into lymphatics is considered to be a major contributor to the transport of material into lymphatics [52]. It has also been found that the presence of interstitial flow is key in facilitating cellular transport mechanisms within the lymphatics, suggesting that investigating the transport of nanoparticles in lymphatics under standard conditions does not fully recapitulate the mechanisms present *in-vivo* [17]. When considering the importance of flow for lymphatic drug delivery, an emerging nanoparticle

formulation parameter to consider is shape. Studies have demonstrated that rod-shaped nanoparticles can align with flow and have improved circulating times compared to traditional spherical nanoparticles [171-175]. Another draw of using rod-shaped nanoparticles is that they have been found to better diffuse through extracellular matrix and mucus barriers [176-179]. This further makes rod shaped nanoparticles an attractive candidate for lymphatic delivery as the extracellular matrix is one of the key barriers for entering and traversing the lymphatics after intradermal or intraperitoneal administration of nanoparticles.

In this chapter, we aim to examine the effects of protein corona formation, interstitial flow, and nanoparticle shape on the delivery of nanoparticles into lymphatic vessels, as well as how these parameters effect the transport mechanisms governing transport into the lymphatic vessels. We used a previously established model for lymphatic transport incorporating simulated transmural fluid flow to examine how flow promotes transport in a shape and mechanism dependent manner [17]. To explore the effect of protein corona, we employed polyethylene glycol (PEG) coated nanoparticles that we have previously identified to effectively cross lymphatic barriers and reach lymph nodes and examined how parameters like PEG density effected corona formation and subsequent transport. To generate rod-shaped nanoparticles we employed a previously established stretching method and incorporated them in in-vitro and in-vivo lymphatic models [180].

5.2 Methods

5.2.1 Nanoparticle formulation

Rod shaped nanoparticles were generated using a previously described mechanical stretching method [181]. 20 mL of 5% w/v solution of polyvinyl alcohol (PVA) was mixed using a magnetic stir bar and heated at 130 °C for at least 1 h until fully dissolved. Once dissolved, 100 nm, fluorescent carboxyl-coated polystyrene nanoparticles (ThermoFisher) were mixed into the PVA solution 0.1% w/v. To plasticize the film, 320 µL of glycerol was also added to the PVA/nanoparticle solution. The solution was then poured into a 12 × 12 cm mold and left to dry overnight uncovered. Once the film fully dried, 9 × 5 cm films were cut from the film and submerged in toluene for three hours to liquefy the nanoparticles. The films were loaded on an Arduino-controlled mechanical stretcher and stretched to up to 2 times the size of the marked grid and left to dry overnight. The film was cut along the grid marks and any non-uniformly stretched portions were discarded. The remaining film sections were submerged in isopropanol to remove any residual toluene. After 24 h, the film sections were removed and then put into a 30% isopropanol solution, which was then mixed and heated at 130 °C for an hour until the film had fully dissolved. The dissolved films were centrifuged for 30 min at 26,000×g, and the supernatant was discarded. The pellet was re–suspended in 30% isopropanol at 130 °C and after 1 h, centrifuged at 26,000×g. This process of PVA film dissolution and washing was repeated three times. To separate the rods from the spheres, solutions of stretched nanoparticles were washed at 12,000×g for 100 nm for 20 min. Stretched nanoparticles were stored in DI H_2O.

To PEGylate the nanoparticles, 40 nm, 100 nm, 100 nm stretched, or 200 nm fluorescent carboxyl (COOH)-modified PS nanoparticles (Thermo Fisher Scientific, F8801) were covalently modified with 5 kDa MW methoxy-PEG-amine (NH_2) (Creative PEGworks), as previously described

[95]. Briefly, PS-COOH particles were suspended at 0.1% w/v in 200 mM borate buffer (pH = 8.2). 350 μM PEG was conjugated to nanoparticles using 7 mM N-Hydroxysulfosuccinimide (NHS) (Sigma) and 0.02 mM 1-Ethyl-3-(3-dimethylaminopropyl) carbodiimide (EDC) (Invitrogen). The reaction was allowed to proceed on a rotary incubator at room temperature for at least 4 hours. Nanoparticles were collected using 100k MWCO centrifugal filters (Amicon Ultra; Millipore) and washed with deionized (DI) water. Nanoparticles were resuspended at 1% w/v in DI water and stored at 4°C.

5.2.2 Nanoparticle characterization

Dynamic light scattering (DLS) was used to measure the hydrodynamic diameter and polydispersity index (PDI) of nanoparticles. Phase analysis light scattering (PALS) was used for measuring ζ-potential (NanoBrook Omni). Measurements were performed using a scattering angle of 90° at 25°C. Measurements were based on intensity of reflected light from scattered particles.

5.2.3 Transmission Electron Microscopy

Stretched nanoparticles were diluted 100× in ultrapure H2O and 25 μL was placed on a square of Parafilm. A PELCO® copper mesh grid (400 mesh Cu, Ted Pella) was inverted and placed on this droplet for 30 s. After, the grid was washed 4 times for 30 s by placing on a 25 μL droplet of ultrapure H20. After drying, the grid was imaged using transmission electron microscopy (JEM-2100, 200 kV, JEOL Ltd).

5.2.4 PEG density characterization

PEG density was determined using a previously published method [97]. Briefly, 5kDa PEG-NH2 (Creative PEGworks) conjugated to fluorescein isothiocyanate (FITC) was conjugated to fluorescent (AlexaFluor®555) 100 nm carboxyl-modified nanoparticles. A FITC-PEG-NH_2

standard curve was generated in DI water to calculate the PEG amount on the nanoparticle surface using a plate reader (Tecan Spark Multimode Microplate Reader). From these measurements, PEG grafting distance (D) and PEG density were estimated using the Flory radius of PEG (R_f). The Flory radius of a polymer chain is defined as $R_f \sim \alpha N^{3/5}$, where N is the degree of polymerization, and α is the effective monomer length. An unconstrained 5 kDa PEG chain has a R_f of 5.4 nm and occupies 22.7 nm^2. PEG density and conformation can be correlated to the ratio of R_f/D, with R_f/D < 1-1.5 yielding a mushroom conformation, 1-1.5< R_f/D > 4 yielding a brush conformation, and R_f/D > 4 yielding a dense brush conformation.

5.2.5 Lymphatic transport model

Nanoparticle transport across LECs was assessed using an established in vitro model that recapitulates in vivo lymphatic transport [17]. Briefly, primary human dermal LECs (hLECs, Promocell C-12217) were seeded on 1.0 μm pore size, 12 mm transwell inserts (Falcon) at 200,000 cells/cm^2 and cultured in EGM2 (Lonza) at 37ºC and 5% CO_2 for 48 h. Cells were pretreated with 1 μm/s transmural flow to simulate the tissue microenvironment. For experiments examining the effect of flow on transport, 1 μm/s or 0.5 μm/s flow rates were maintained throughout experiment by generating a fluid head within the transwell as previously described [17]. hLECs were treated with 1% w/v nanoparticles on the apical side and the basolateral compartment was sampled for up to 24 h. Fluorescence intensity was measured using a plate reader (Tecan) and nanoparticles transported was calculated using a standard curve. Transport experiments were performed in EGM2 without growth factors to avoid the confounding effects of growth factors. To probe the transport mechanism the following transport inhibitors were used: 100 nM Adrenomedullin (Abcam ab276417), 62.5 μM Dynasore (Sigma D7693), or 62.5 μM Amiloride (Sigma A7410). Transport inhibitors were applied 2 hours prior

to introduction of nanoparticles. To examine the effect of albumin protein corona formation on lymphatic transport, 100 nm PEGylated nanoparticles were incubated in 10 mg/mL albumin for 30 min. Nanoparticles were collected and separated from protein solution via centrifugation at 17,000 x g for 20 minutes and washing with DI water twice before pellet was collected before being administered to the transport model at 1% w/v.

5.2.6 Immunofluorescence staining

Cells were fixed in 2% PFA for 15 minutes and incubated with mouse anti-human VE-Cadherin (BD Sciences) at 4ºC overnight. Secondary antibodies conjugated to Alexa Fluor® 488 or 647 were used for detection (Thermo Fisher). Slides were mounted using DAPI (4',6-diamidino-2-phenylindole)-containing Vectashield (Vector Laboratories Inc., Burlingame, CA) and imaged using a Zeiss Axio Observer. Image processing was performed using FIJI (NIH).

5.2.7 C57Bl/6J lymphatic delivery model

10 µL of 5 mg/mL, fluorescently-labeled nanoparticles was intradermally administered to female C57Bl/6J mice (8-12 weeks old) in their forelimbs. Fluorescence intensity was measured using IVIS Spectrum Fluorescent & Chemiluminescent Imaging System (Caliper Life Sciences) over a 12h time period. Distance of nanoparticle transport was calculated from centroid of injection site to maximally distant pixel of fluorescence signal using ImageJ. This pixel length was then converted to centimeters. Mice were anesthetized with isoflurane prior to nanoparticle injection and during imaging. Mice were euthanized after the final time point (8 hr). Draining LNs were collected and homogenized to quantify the fluorescence signal from nanoparticles using a plate reader (Tecan). LNs were also fixed in 4% PFA for 6 hours and treated with a sucrose gradient. Tissues were then embedded within OCT (ThermoFisher), sectioned, and stained for FITC-B220 (BioLegend). Slides were mounted using DAPI (4',6-diamidino-2- phenylindole)-containing

Vectashield (Vector Laboratories Inc., Burlingame, CA) and imaged using a Zeiss Axio Observer. Image processing was performed using FIJI (NIH). All procedures were approved by the University of Maryland, College Park IACUC.

5.2.8 Protein Corona Analysis

Nanoparticles were incubated in fetal bovine serum or 10 mg/mL albumin for 30 min. Nanoparticles were collected and separated from protein solution via centrifugation at 17,000 x g for 20 minutes and washing with DI water twice before pellet was collected. The amount of protein on the nanoparticle surface was quantified using Pierce micro BCA assay kit (ThermoFisher). Absorbance at 562 nm was measured using a plate reader (Tecan Spark Multimode Microplate Reader).

5.2.9 Statistics

Group analysis was performed using a 2-way ANOVA, followed by Tukey's post-test. Unpaired Student's t-test was used to examine differences between only two groups. A value of $p < 0.05$ was considered significant (GraphPad). All data is presented as mean ± standard error of the mean (SEM).

5.3 Results

5.3.1 Protein Corona Forms Rapidly on PEGylated Nanoparticles and Improves Transport Across Lymphatics

Shape has been shown to affect how nanoparticles interact with surrounding tissues and cells [172, 174]. In this study we used PEGylated nanoparticles that have been previously shown to improve transport across lymphatic vessels and reach lymph nodes [153]. Using the mechanical stretching technique, we generated rod-shaped nanoparticles. When stretched and PEGylated 100 nm nanoparticles increased in size from 142 nm to 201 nm, making the rod shaped nanoparticles closer in size to the 200 nm PEGylated nanoparticles (198 nm) (**Fig 19A**). When the R_f/D of the nanoparticles was calculated, all formulations and shapes had PEG in dense brush conformation (3.5 – 4.5) (**Fig 19B**). When the surface charge of the fully PEGylated spherical nanoparticles and rod-shaped nanoparticles was measured, they were near neutral (> -5 mV), suggesting dense PEG coverage in conjunction with the R_f/D calculations (**Fig 19C**). PDI of the nanoparticles measured via DLS indicated that the rod-shaped nanoparticles had a slightly non-uniform distribution of sizes with a PDI >0.2. This higher PDI is likely due to the anisotropic shape of the nanoparticles as well as the fact that the stretching process is not completely efficient: imaging via electron microscopy reveals a heterogenous sample containing both rods and spheres. This is likely due to the fact that the rod-shaped nanoparticles are anisotropic and the stretching protocol is not completely efficient (**Fig 19D-E**).

As a preliminary way to understand the formation of the protein corona on the surface of nanoparticles, and how this effects nanoparticle transport into lymphatics, we incubated 40 nm and 100 nm nanoparticles with a dense coating of PEG (full PEG) and sparse coating of PEG (0.1PEG)

in a 10 mg/mL albumin solution and FBS. We found that between formulations, the amount of protein adsorbing to the surface of the nanoparticles remained consistent. In this preliminary experiment, we observed that 40 nm $PSPEG_{Rf/D=0.9}$ nanoparticles having measurably more FBS protein on the surface compared to the fully PEGylated nanoparticles. (**Fig 20A**). We then examined if the addition of protein on the surface of the nanoparticles improved transport across LEC barriers using our transwell based model. Particularly, we examined the role of albumin, an extremely abundant protein that is known to be actively transported into lymphatics and is known to be a major protein corona component. The addition of albumin correlated with an increase in transport efficiency for both PEGylated 100 nm nanoparticles, and non-PEGylated 100 nm polystyrene nanoparticles. Indeed, the pre-incubation of the polystyrene nanoparticles resulted in a significant increase in transport efficiency, becoming comparable to the efficiently transported 100 nm PEGylated nanoparticles (**Fig 20B**). When examining IF images of the LEC model, we see that there is an increase in the polystyrene nanoparticle signal when they are pre-incubated in albumin (**Fig 20C-D**).

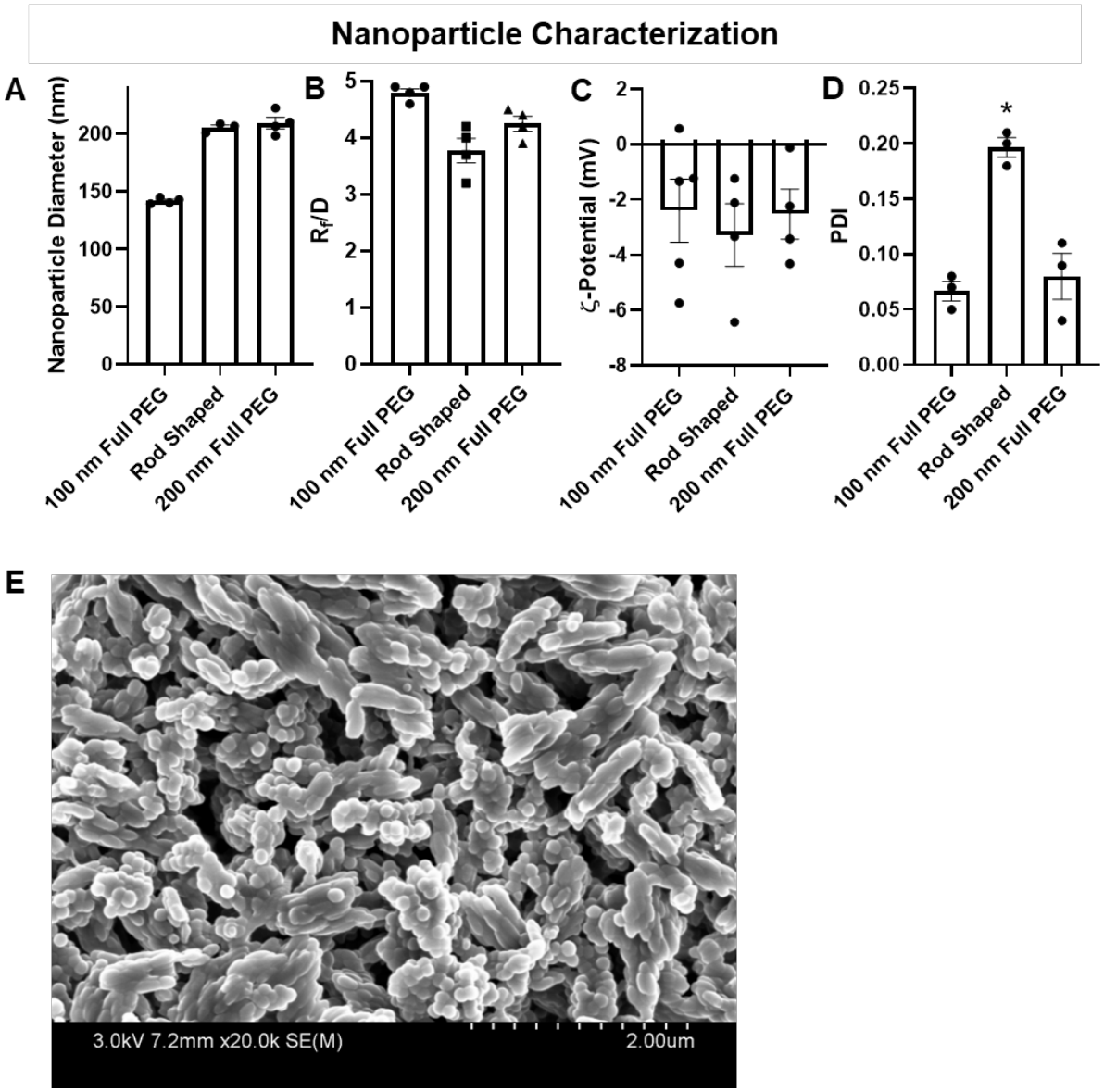

Figure 19 Formulation of PEGylated Rod-Shaped Nanoparticles **A**) Diameter of nanoparticles measured using DLS **B**) Calculated R_f/D of nanoparticles. **C**) Surface charge of nanoparticles measured via PALS **D**) PDI of nanoparticles measured by DLS. E) TEM images of nanoparticles after stretching and PEGylation protocol. Data presented as mean ± SEM (*p<0.05) n = 3-4

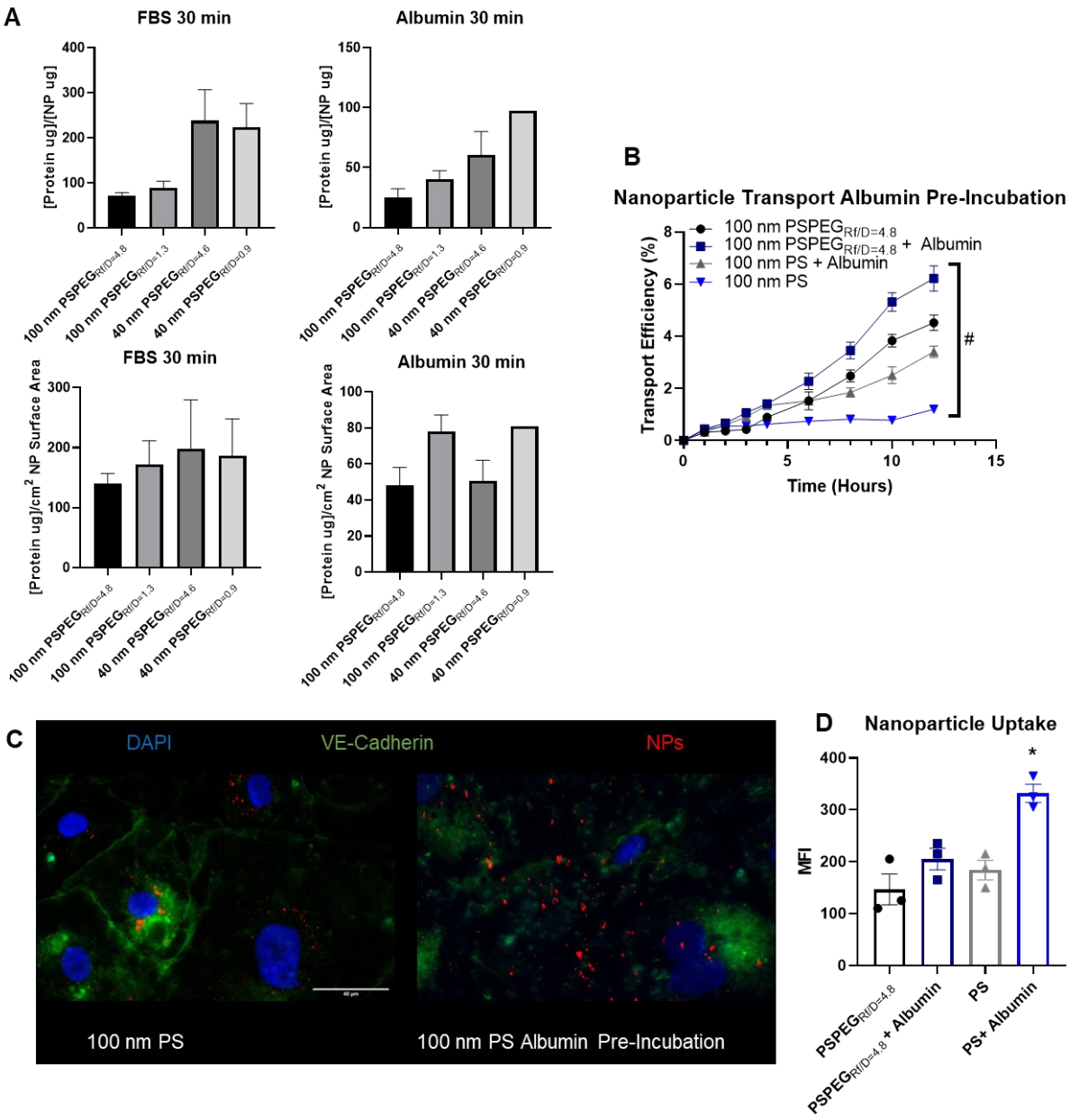

Figure 20 *Albumin Protein Corona on Nanoparticle Improves Nanoparticle Transport Across LECs* **A**) BCA protein quantification of nanoparticles in protein solutions **B**) Transport efficiency of nanoparticles across hLECs pre-incubated in 10 mg/mL albumin **C**) IF images of sectioned lymph nodes with nucleus in blue and nanoparticles in red. **D**) Quantification of IF images. Data presented as mean ± SEM (*p<0.05, #p<0.1) n = 2-4 repeats

5.3.2 Interstitial Fluid Flow Improves Nanoparticle Transport Across Lymphatics

The fully PEGylated $PSPEG_{Rf/D=4.8}$ 100 nm spherical nanoparticles were administered to a previously described in vitro transendothelial transport model of primary human LECs was cultured on the bottom of a collagen-coated transwell (**Fig 21A**) to simulate transport from the interstitium into the lymphatic vessel [17]. When looking at spherical $PSPEG_{Rf/D=4.8}$ nanoparticle transport in the presence of modeled transmural flow, we observed that the presence of any transmural flow increased transport efficiency at least 5 fold after six hours (**Fig 21B**). After IF imaging of the LEC model, we observed that LECs treated with flow trended towards internalized higher amounts of fluorescent nanoparticles (not significant) (**Fig 21C-D**).

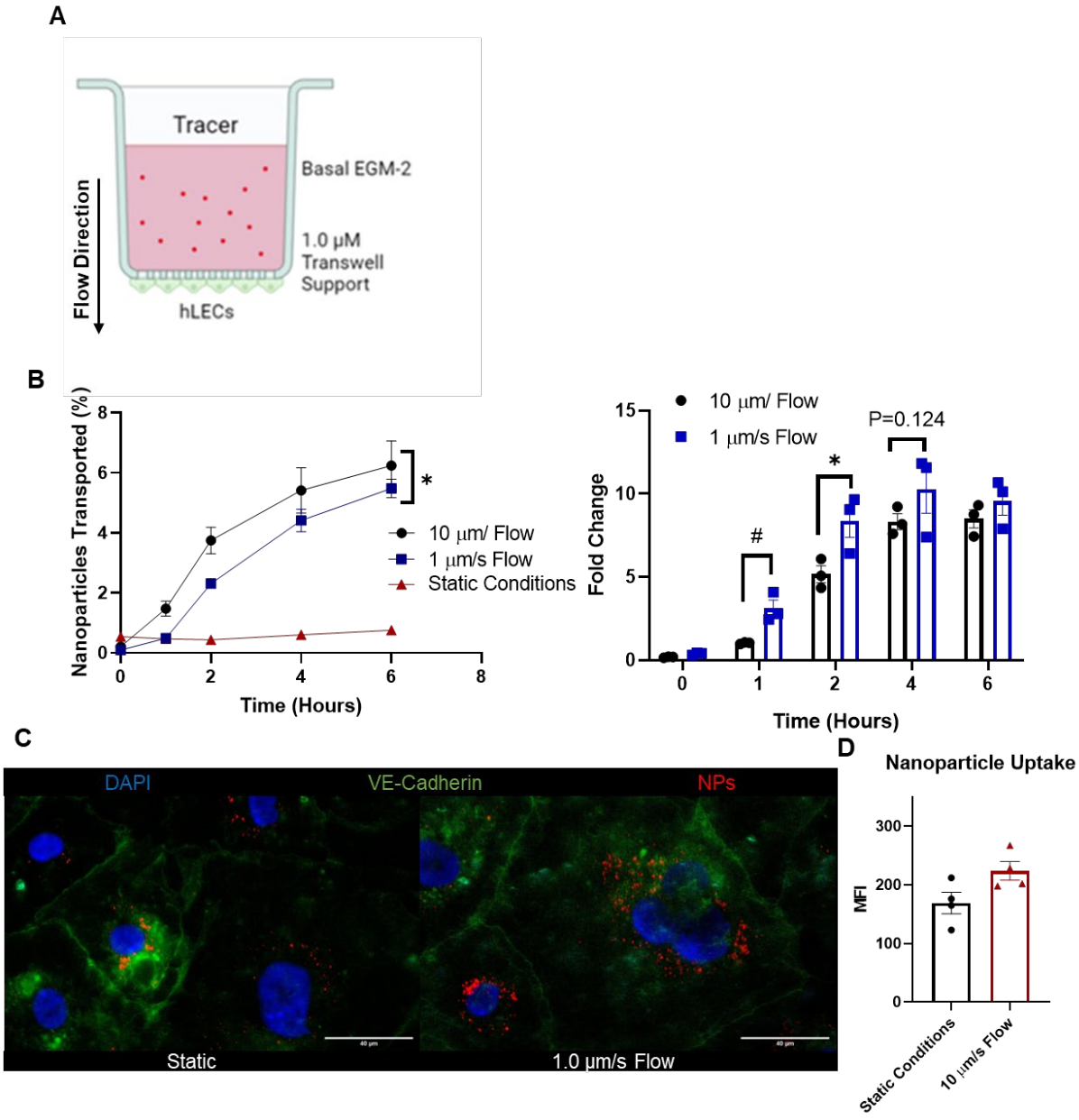

Figure 21 *Interstitial Fluid Flow Improves Nanoparticle Transport Across Lymphatics* **A**) Schematic of lymphatic transport model **B**) Transport efficiency over time of 100 nm fully PEGylated PSPEGRf/D=4.8 nanoparticles across hLECs under 10, 1, and 0 µm/s and fold increase of transport compared to static conditions. **C**) IF images of hLECs with VE-Cadherin stained in green, nucleus in blue, and nanoparticles in red. **D**) MFI of IF images from lymphatic model. Data presented as mean ± SEM (*p<0.05, #p<0.1) n = 3-4

5.3.3 Interstitial Fluid Flow Enhances Rod-Shaped Nanoparticle Transport Across Lymphatics

We then administered the fully PEGylated 100 nm $PSPEG_{Rf/D=4.8}$ spherical nanoparticles, the rod shaped $PSPEG_{Rf/D=4.3}$ nanoparticles, and the 200 nm fully PEGylated $PSPEG_{Rf/D=4.2}$ nanoparticles to our lymphatic transport model to examine how shape effects the transport efficiency across lymphatics. We saw that rod shaped nanoparticles and 200 nm nanoparticles were transported similarly while the 100 nm nanoparticles exhibited significantly higher transport efficiency (**Fig 22A**). We saw that when we inhibited micropinocytosis with Dynasore, and when we inhibited macropinocytosis with amiloride, there was a significant decrease in transport efficiency of rod $PSPEG_{Rf/D=4.3}$ nanoparticles. Importantly, when paracellular transport was inhibited with adrenomedullin, closing the spaces between cells, we observed the greatest decrease in transport efficiency (**Fig 22B**). Simulated transmural flow drives the transport of fluid into lymphatic vessels in vivo and has been shown to effect LEC permeability [17]. We wanted to probe how the presence of physiologically relevant transmural flow affected the transport of rod shaped nanoparticles across lymphatic barriers. Interestingly, we saw that in the presence of model flow, rod shaped nanoparticles were transported up to 6-fold more efficiently compared to static conditions. This is a marked increase compared to the 3-fold increase observed with respect to the spherical nanoparticles in the presence of transmural flow (**Fig 22C**). When the transport mechanisms of rod shaped nanoparticles was observed under flow conditions, we saw similar trends to the static conditions, where inhibition of paracellular transport through the introduction of adrenomedullin caused the greatest reduction in transport efficiency (**Fig 22D**). IF imaging of LEC models indicated that there was intracellular uptake of the rod shaped nanoparticles. Notably, when paracellular transport was inhibited, we observed an increase in nanoparticle signal within the cells (**Fig 22D-E**).

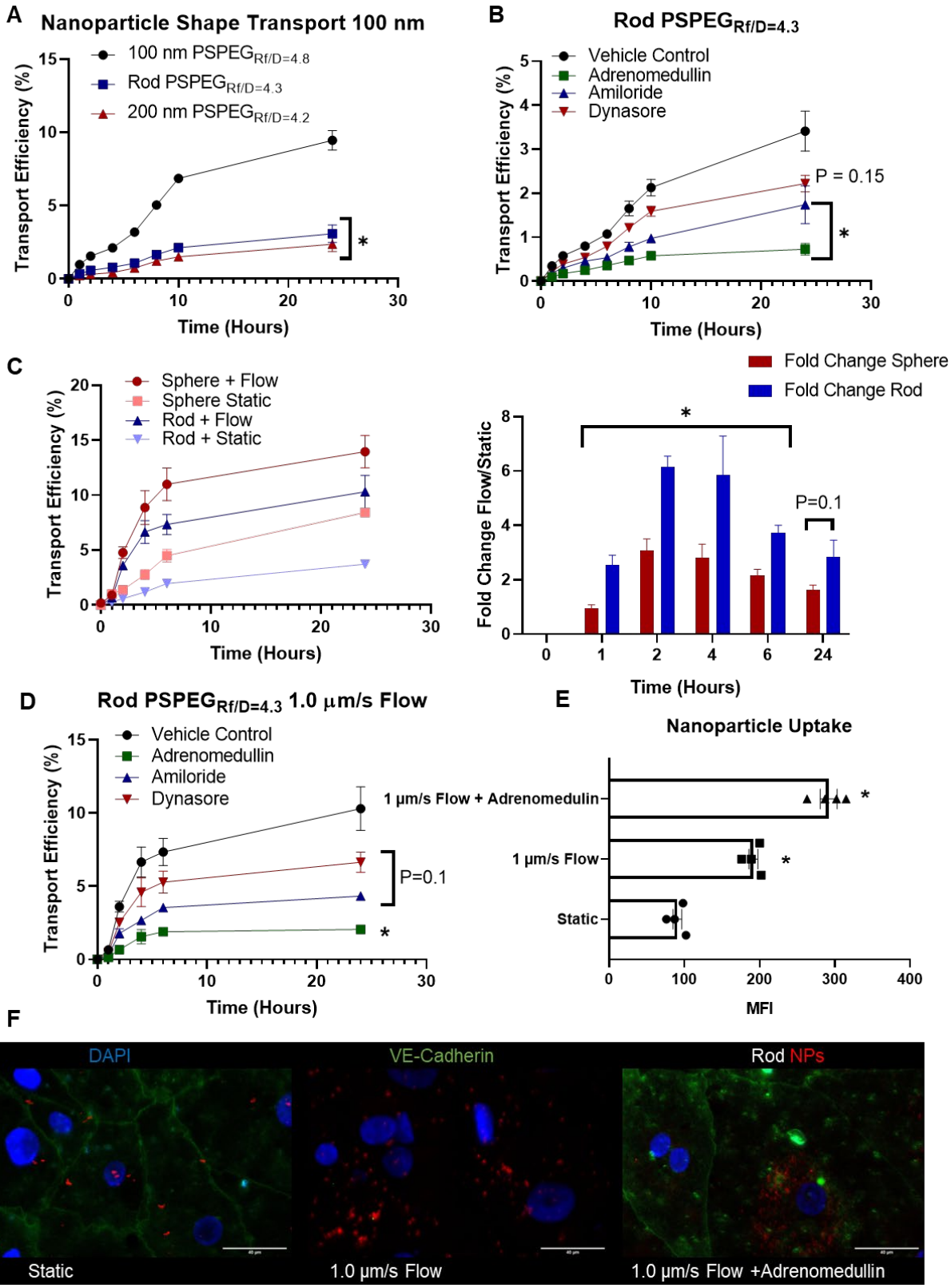
A
Nanoparticle Shape Transport 100 nm
100 nm PSPEG Rf/D=4.8
Rod PSPEG Rf/D=4.3
200 nm PSPEG Rf/D=4.2
Transport Efficiency (%)
Time (Hours)
*
B
Rod PSPEG Rf/D=4.3
Vehicle Control
Adrenomedullin
Amiloride
Dynasore
P = 0.15
*
Transport Efficiency (%)
Time (Hours)
C
Sphere + Flow
Sphere Static
Rod + Flow
Rod + Static
Transport Efficiency (%)
Time (Hours)
Fold Change Sphere
Fold Change Rod
*
P=0.1
Fold Change Flow/Static
Time (Hours)
D
Rod PSPEG Rf/D=4.3 1.0 µm/s Flow
Vehicle Control
Adrenomedullin
Amiloride
Dynasore
P=0.1
*
Transport Efficiency (%)
Time (Hours)
E
Nanoparticle Uptake
1 µm/s Flow + Adrenomedulin
1 µm/s Flow
Static
*
*
MFI
F
DAPI
VE-Cadherin
Rod NPs
Static
1.0 µm/s Flow
1.0 µm/s Flow +Adrenomedullin

Figure 22 *Interstitial Fluid Flow Improves Rod-Shaped Nanoparticle Transport Across Lymphatics* **A**) Transport efficiency of nanoparticles across lymphatic transport model. **B**) Transport efficiency of rod-shaped nanoparticles across lymphatic model in the presence of different transport inhibitors. **C**) Transport efficiency of 100 nm spherical nanoparticles and rod shaped nanoparticles across lymphatic transport model in the presence of flow and fold increase of transport compared to static conditions. **D**) Transport efficiency of rod-shaped nanoparticles across lymphatic model in the presence of different transport inhibitors and interstitial flow. **E**) MFI of IF images from lymphatic model. Data presented as mean **F**) IF images of hLECs with VE-Cadherin stained in green, nucleus in blue, and nanoparticles in red. Data as ± SEM (*p<0.05) n = 3-4

5.3.4 Rod Shaped Nanoparticles Reach Lymph Nodes More Efficiently Compared to similarly Sized Nanoparticles

To confirm our observed transport trends on lymphatic transport *in-vitro* with delivery to lymph nodes, we intradermally injected the spherical 100 nm and 200 nm nanoparticles, as well as the rod shaped nanoparticles. IVIS imaging of the fluorescent nanoparticles indicated that the 100 nm nanoparticles and the rod shaped nanoparticles are present in lymph nodes after 8 hrs (**Fig 23A**). This time frame is indicative of lymphatic vessel mediated transport as opposed to cell migration mediated transport which typically requires over periods over 12 hrs [3]. Lymph nodes were collected after 8 hours and homogenized for fluorescence measurement. We found that the fluorescence signal of the rod shaped nanoparticles was similar to that of the spherical 100 nm nanoparticles, despite the rod nanoparticles being closer in size to the 200 nm spherical nanoparticles (**Fig 23B**). Furthermore, when examining the localization of the rod-shaped nanoparticles in collected lymph nodes, we saw that there seems to be nanoparticle signal in the cortex of the lymph node (**Fig 23C**).

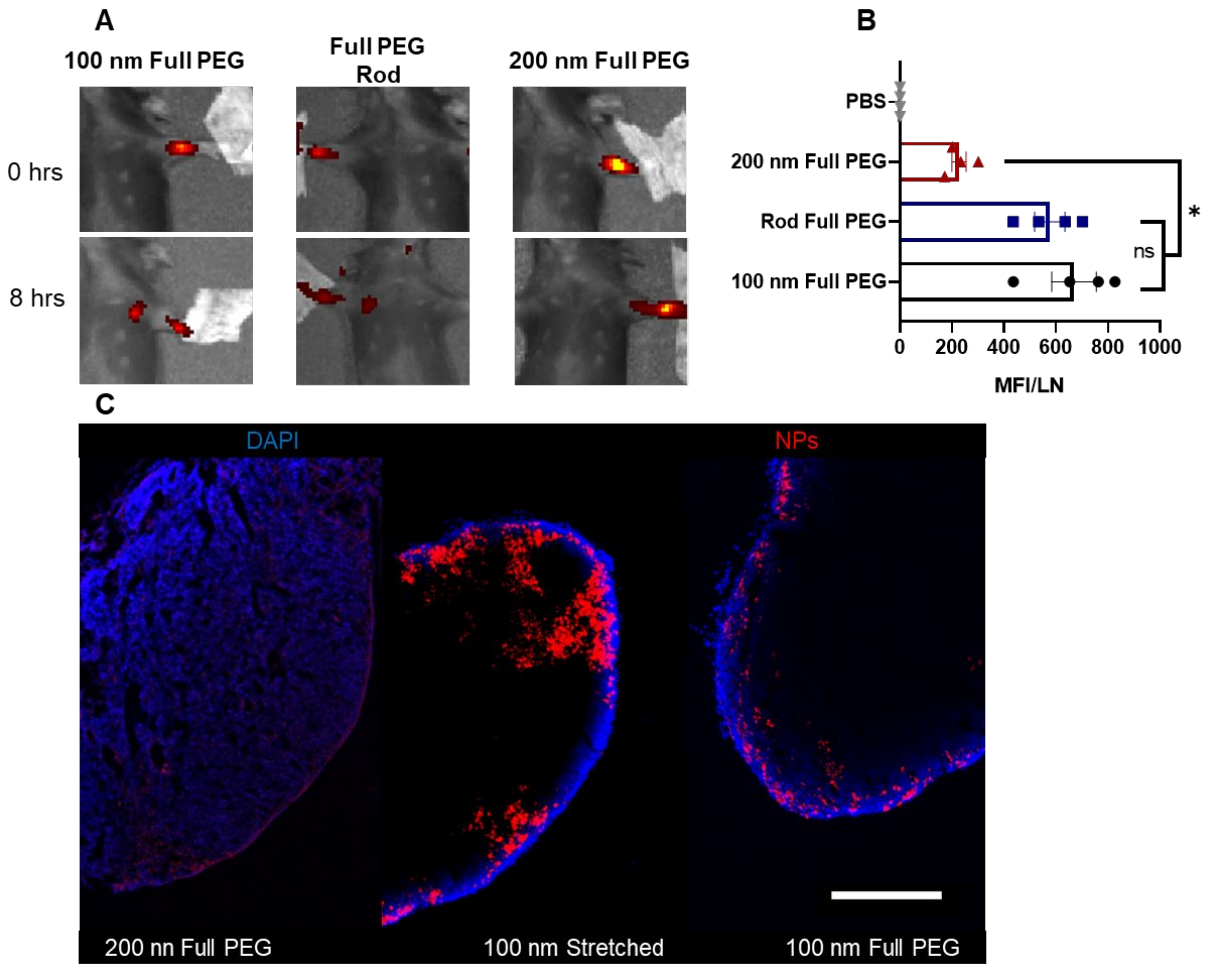

Figure 23 *Rod Shaped Nanoparticles Reach Lymph Nodes More Efficiently Compared to similarly Sized Nanoparticles* **A**) IVIS imaging of C57Bl/6J after intradermal injection at 0h and 8h. **B**) MFI of homogenized lymph nodes at 8h. **C**) IF images of sectioned lymph nodes with nucleus in blue and nanoparticles in red. Data presented as mean ± SEM (*p<0.05) n = 3-4 mice

5.4 Discussion

In this chapter we sought to determine how nanoparticle shape affects transport across lymphatics, and ultimate delivery to lymph nodes. Our key findings from this chapter are as follows: 1) the introduction of simulated transmural flow significantly and rapidly increases the uptake and transport efficiency of nanoparticles across lymphatic barriers, 2) rod shaped nanoparticles in the absence of interstitial flow were transported poorly across lymphatic barriers, but in the presence of flow had transport efficiency comparable to the spherical counterparts, 3) rod shaped nanoparticles were primarily transported paracellularly, 4) rod-shaped nanoparticles had improved lymph node delivery to lymph nodes *in-vivo* compared to similarly sized nanoparticles, and 5) protein corona formation, particularly the presence of albumin, improved nanoparticle transport across LECs.

Nanoparticle shape has recently been shown to be a key characteristic that can improve drug delivery efficiency by improving transport across mucus and extracellular matrices, as well as improving circulation times. In our study, we stretched 100 nm nanoparticles into 200 nm long rods with approximately 40-60 nm diameter narrow axis. When compared to similarly sized 200 nm spherical nanoparticles, the rod-shaped nanoparticles were transported more efficiently across lymphatic barriers and to lymph nodes. This was true especially in the presence of interstitial flow. This could be explained by previous findings indicating that rod shaped nanoparticles can align with flow [172, 182]. Indeed, the Discher group was one of the first to observe that nanoparticle shape was a key factor in improving tumoral administration of nanoparticles [172-174]. This improved delivery of nanoparticles within tissues has been hypothesized by them and other groups to be due to the fact rod-shaped nanoparticles can diffuse effectively through the extracellular matrix thanks to the narrow axis and rod shape allowing the particles to “roll” through the matrix

if the matrix pore size is less than that of the nanoparticle [172, 176, 178, 179, 183]. This improved transport through extracellular matrix is mirrored in our findings where rod shaped nanoparticles reached lymph nodes more effectively than similarly sized spherical nanoparticles. This could also explain our result where we observe improved entry of the nanoparticle into the cortex of lymph nodes after intradermal injection.

Groups have also examined how nanoparticle shape governs the uptake and transport mechanisms used to internalize nanoparticles. Liu et al showed that micropinocytosis and macropinocytosis pathways were employed in the uptake of rod-shaped bio-nanoparticles in epithelial and endothelial cells [184]. Xie et al also examined how nanoparticle shape effects uptake of rod-shaped nanoparticles in macrophages and the mechanisms driving uptake in macrophages. They found that clathrin and caveolin mediated endocytosis drove the uptake of 100 nm rod shaped nanoparticles [185]. Other studies from Dasgupta et al and Xu et al observed similar results where cellular mechanisms drove transport of rod shaped nanoparticles into endothelial an epithelial cells [186, 187]. Collectively, these results on the cellular mechanisms governing rod shaped nanoparticle transport are replicated in the transport mechanism data in this chapter, where inhibition of micropinocytotic and macropinocytotic transport with Dynasore and amiloride, respectively, hindered nanoparticle transport across lymphatics.

Protein corona formation after administration has been shown to be a key factor in nanoparticle drug delivery. In this study, we provide some of the first insights on how this corona formation impacts transport across lymphatics. There exists data indicating that the formation of the protein corona on the surface of nanoparticles is sometimes beneficial, and sometimes harmful for nanoparticle-based drug delivery. Some studies have demonstrated that the formation of protein corona on the surface of nanoparticles can hinder nanoparticle transport across endothelial and

epithelial barriers by blocking nanoparticle interactions with the cell membrane [167, 168]. To combat this, many formulation strategies, including the one outlined in this chapter employ PEG to impart stealth characteristics to nanoparticles. However, studies have shown that the addition of PEG can alter the formation of protein corona on the surface of nanoparticles. Seneca et al demonstrated that even at low PEG density apolipoprotein A1 and clusterin stealth proteins and that high PEG density is required to prevent protein adsorption [188]. Abstiens et al created a library of different nanoparticles with combinations of PEG terminal groups: positively charged amines, negatively charged carboxyl groups, a combination of the two (zwitterionic), or non-charged methoxy groups [189]. They found that amine-coated Nanoparticles presented faster and higher protein absorption, and lower stability in serum. Carboxyl-PEG and methoxy-PEG Nanoparticles showed lower PC assembly. Interestingly, the lowest protein absorption was observed in zwitterionic-PEG Nanoparticles. Partikel et al also demonstrated that protein adsorption on PLGA- and PLGA-PEG-NP didn't depend on NP size within the range of 100 and 200 nm, however, PEGylation led to a significant reduction in protein corona formation [166]. These above results correlate with our findings in this chapter where the charged nanoparticles, hydrophobic PS nanoparticles displayed the most significant protein corona formation compared to the PEGylated nanoparticles. An interesting consequence of this increased protein adsorption on the surface of PS nanoparticles is that when incubated in albumin, the presence of a pre-formed protein corona significantly improves nanoparticles transport efficiency. This increased transport efficiency due to the presence of albumin is a strategy that has been employed extensively by other groups. Notably the Irvine groups has generated numerous lymphatic vessel and lymph node targeting vaccine assemblies employing the innate albumin shuttling of lymphatics [169, 190].

In summary, this chapter indicates that rod shaped nanoparticles could be a promising lymphatic drug delivery platform, and that albumin adsorption on the surface of nanoparticles could improve lymphatic drug delivery. This study is one of the first to examine how lymphatics regulate the transport of rod-shaped nanoparticles and on the delivery of rod-shaped nanoparticles to lymph nodes via lymphatic vessels.

6 Conclusions and Future Directions

Therapeutic treatments targeting the immune system including classic vaccines as well as caner immunotherapies are becoming more and more prevalent. Recently, lymphatic vessels have received significant attention as a potential drug delivery target for immunotherapies. Lymphatics form the body's natural conduit between peripheral tissues and the local draining lymph nodes, where the adaptive immune response is shaped. Delivery of these treatments to the draining lymph nodes, where adaptive immunity is formed, amplifies their efficacy, thus potentially improving their clinical outcomes. Lymph nodes can be indirectly targeted via lymphatic vessels, which exist throughout the entire body and are mainly appreciated for transporting cells, fluid, and particulates from peripheral tissues to the local lymph nodes. The objective of this dissertation was to understand optimum nanoparticle formulation strategies for effective delivery into lymphatic vessels and the understand the mechanisms governing transport of nanoparticles.

Chapter 3: Nanoparticles with Dense Poly(ethylene glycol) Coatings with Near Neutral Charge are Maximally Transported Across Lymphatics and to the Lymph Nodes

In this chapter we introduce a nanoparticle system where we can tune the conformation of polyethylene glycol (PEG) on the surface of nanoparticles to probe how surface chemistry affects entry into lymphatics. Using these tools, we were able to demonstrate that a dense coating of PEG was required for entry into lymphatics and delivery to lymph nodes. In this chapter we also demonstrated that both transcellular and paracellular transport are required for transport into lymphatics, and that the cellular mechanisms of transport are dependent on formulation.

The future directions of this work would be to transition away from using polystyrene nanoparticles to using biocompatible nanoparticles, such as PLGA. Additionally, incorporating a

therapeutic into the nanoparticles would be beneficial to further understand the therapeutic potential of these formulation parameters. Preliminary work from our lab has demonstrated that we are able to generate 50-150 nm densely PEGylated PLGA nanoparticles, indicating that the findings in this chapter with respect to surface chemistry can be applied to more clinically relevant systems. In conjunction to the inclusion of a therapeutic agent, it would be beneficial to introduce these nanoparticles to a disease model. By making loaded nanoparticles a treatment for disease, we can answer the question: how much transport is necessary? Treatment outcome can be observed as a function as delivery efficacy. This application would directly address the link between improved lymphatic delivery to improved therapeutic outcomes. Additionally, it would be important to understand how nanoparticle transport across lymphatics is affected by disease conditions. Indeed, preliminary work published with a collaboration has demonstrated that the presence of external factors like cigarette smoke significantly lowers the barrier function of lymphatic vessels [191].

Chapter 4: Para- and transcellular transport kinetics of nanoparticles across LECs

In this chapter we further examined the kinetics of nanoparticles across LECs. In this chapter we built a three-compartment model and system of differential equations to describe the transport of nanoparticles across lymphatic barriers. This chapter produced some of the first quantitative kinetic values to describe transport across lymphatics relating transport mechanism as well as nanoparticle formulation.

The future directions of this work would be to enhance the current computational model. One potential improvement would be the incorporation of more advanced statistical modeling of the transport data, possibly through machine learning. In a similar approach, incorporation of machine

learning could lend predictive power to the computational model, identifying optimum nanoparticle formulations outside of the parameters that we have experimented on.

Chapter 5: Extracellular Cues and Nanoparticle Shape Influence Transport Mechanism and Efficiency Across Lymphatics

In this chapter we examined how two extracellular phenomena 1) transmural flow across lymphatics, and 2) the adsorption of protein on the surface of nanoparticles in the form of a protein corona affects nanoparticle transport across lymphatics. In this chapter we also introduced the parameter of nanoparticle shape on transport across lymphatics. While much of the experiments in this chapter are preliminary with $n < 3$ for some, are fer interesting trends are emerging. Our key findings from this chapter are as follows: 1) the introduction of transmural flow significantly and rapidly increases the uptake and transport efficiency of nanoparticles across lymphatic barriers, 2) rod shaped nanoparticles in the absence of interstitial flow were transported poorly across lymphatic barriers, but in the presence of flow had transport efficiency comparable to the spherical counterparts, 3) rod shaped nanoparticles were primarily transported paracellularly, 4) rod-shaped nanoparticles had improved lymph node delivery to lymph nodes in-vivo compared to similarly sized nanoparticles, and 5) protein corona formation, particularly the presence of albumin, improved nanoparticle transport across LECs.

The future of this work would be to repeat some of these experiments to gain confidence in the trends. For investigating the protein corona on nanoparticles, a key experiment would be to identify the components of the corona through mass spectrometry and western blot. In terms of nanoparticle shape, work can be done to improve the formulation efficiency of the nanoparticles. Work can also be done to experiment with different shapes in addition to rods, shapes containing points (i.e. stars and triangles), have shown promise in promoting delivery to specific cell populations.

For all three chapters, an exciting future avenue for work would be the incorporation of a disease model to confirm the hypothesis that formulation strategies that are improving nanoparticle transport into lymphatics correlates improve therapeutic potential. Future work in the lab is also dedicated to generating improved models of lymphatics and other target tissues. One example is outlined in the appendix of this thesis where we have been working to develop a mucosal-lymphatic model. Oral administration of therapeutics is an ideal delivery route, and with the large number of lymphoid tissues in the gastrointestinal tract, engineering a nanoparticle carrier that can effectively cross both barriers would be key. In this appendix, I include a study where we worked to characterize the mucus produced by model intestinal epithelial cells and identify cocultures that would be ideal to incorporate into more advanced models including a lymphatic component, microbiota component, or other lymphoid tissue component. Current work in the lab is also striving to engineer a three-dimensional lymphatic vessel, and to engineer in-vitro lymphatic vessels that can recapitulate the initial lymphatics, which function as entry points to the lymphatics in similar manner to blood capillaries, and collecting lymphatics, which are more impermeable, valved, and function as a bulk transporter of fluid to lymph nodes. Notably, initial lymphatics have been observed to have discontinuous junctions, while the collecting junctions have continuous junctions. The continuous junctions of our transwell based model are more like those that would be seen in collecting vessels. As a result, work is being done in the lab to tune LEC culture conditions to promote a more initial lymphatics-like cell.

7 Publications and Conference Presentations

McCright, J., Yarmovsky, J., and Maisel, K., *Para- and transcellular transport kinetics of nanoparticles across LECs.* bioRxiv, 2023: p. **2023**.04.12.536598. (*Under Review*)

Amosu, M.M., **McCright, J**., …Maisel, K., Inhaled CpG increases survival and synergizes with checkpoint inhibition in lymphangioleiomyomatosis. *bioRxiv*, **2023**: p. 2023.02.06.527331. (*Under Review*)

McCright, J., A. Sinha, and K. Maisel, Generating an In Vitro Gut Model with Physiologically Relevant Biophysical Mucus Properties. *Cellular and Molecular Bioengineering*, **2022**. 15(5): p. 479-491.

McCright, J.; Naiknavare, R.; Yarmovsky, J.; Maisel, K. Targeting Lymphatics for Nanoparticle Drug Delivery. *Frontiers in Pharmacology* **2022**, 13

McCright, J.; Skeen, C.; Yarmovsky, J.; Maisel, K. Nanoparticles with dense poly(ethylene glycol) coatings with near neutral charge are maximally transported across lymphatics and to the lymph nodes. *Acta Biomater* **2022**.

Summers, B. D.; Kim, K.; Clement, C. C.; Khan, Z.; Thangaswamy, S.; **McCright, J**.; Maisel, K.; Zamora, S.; Quintero, S.; Racanelli, A. C.; et al. Lung lymphatic thrombosis and dysfunction caused by cigarette smoke exposure precedes emphysema in mice. *Scientific Reports* **2022**, *12*

McCright, J.; Ramirez, A.; Amosu, M.; Sinha, A.; Bogseth, A.; Maisel, K. Targeting the Gut Mucosal Immune system Using Nanomaterials. *Pharmaceutics* **2021**, *13*,

McCright, J. & Maisel, K. Engineering drug delivery systems to overcome mucosal barriers for immunotherapy and vaccination. **Tissue barriers**, 1695476-1695476 (**2019**).

Bae, D.H.;...**McCright, J**;...Reiser, J. Design and Testing of Vector-Producing HEK293T Cells Bearing a Genomic Deletion of the SV40 T Antigen Coding Region. **Molecular Therapy-Methods & Clinical Development** 18, 631-638 (**2020**).

Conferences and Presentations

Engineering Nanoparticles For Improved Lymphatic Targeting
McCright, Jacob; Skeen, Colin; Yarmovsky, Jenny; Maisel, Katharina
University of Maryland, College Park
BMES Fall 2020 (virtual)
Poster

Engineering Nanoparticles For Improved Lymphatic Targeting
McCright, Jacob; Skeen, Colin; Yarmovsky, Jenny; Maisel, Katharina
University of Maryland, College Park
BME Forum Fall 2020
Poster

Engineering nanoparticle surface chemistry to maximize lymph node delivery via lymphatic vessels
McCright, Jacob; Skeen, Colin; Yarmovsky, Jenny; Maisel, Katharina
University of Maryland, College Park
Lymphatic Forum Summer 2021
(virtual)
Podium Talk

Engineering nanoparticle surface chemistry to maximize lymph node delivery via lymphatic vessels
McCright, Jacob; Skeen, Colin; Yarmovsky, Jenny; Maisel, Katharina
University of Maryland, College Park
CRS Summer 2021
virtual
Podium Talk

Engineering Nanoparticles For Improved Lymphatic Targeting
McCright, Jacob; Skeen, Colin; Yarmovsky, Jenny; Maisel, Katharina
University of Maryland, College Park
SFB Annual Meeting, Baltimore, MD, Spring 2022
Podium Talk

Engineering Nanoparticles For Improved Lymphatic Targeting
McCright, Jacob; Skeen, Colin; Yarmovsky, Jenny; Maisel, Katharina
University of Maryland, College Park
Gordon Immunoengineering Conference, Ventura, CA, Summer 2022
Poster presentation

Engineering nanoparticle surface chemistry to maximize lymph node delivery via lymphatic vessels
McCright, Jacob; Skeen, Colin; Yarmovsky, Jenny; Maisel, Katharina
University of Maryland, College Park
BMES Annual Meeting, San Antonio, TX, Fall 2022
Podium Talk

Professional Associations:

Member of the Biomedical Engineering Society (BMES), 2014-2023

Member of the American Heart Association (AHA), 2021-2023

Member of the Society for Biomaterials (SFB), 2021-2023

8 Appendix 1: Generating an in vitro gut model with physiologically relevant biophysical mucus properties

This chapter is reproduced with permission from: McCright, J., Sinha, A. & Maisel, K. Generating an *In Vitro* Gut Model with Physiologically Relevant Biophysical Mucus Properties. *Cel. Mol. Bioeng.* **15**, 479–491 (2022). https://doi.org/10.1007/s12195-022-00740-0

This chapter is being included as an appendix as it outlines some preliminary work in developing a mucosal-lymphatic model that the lab is interested in. Oral administration of therapeutics is an ideal delivery route, and with the large number of lymphoid tissues in the gastrointestinal tract, engineering a nanoparticle carrier that can effectively cross both barriers would be key.

8.1 Introduction

Mucus is the first line of defense to the outside world, covering our lungs, eyes, gastrointestinal tract, and urogenital tract. Mucus is a viscoelastic hydrogel-like network composed of water and mucins that effectively traps pathogens and foreign particulates, preventing them from harming or infecting the underlying epithelial cells. Mucins are high molecular weight glycoproteins, containing hydrophilic and hydrophobic domains that link and form a mesh with pores that can vary considerably between species of origin[192-195] and fall within the range of 100-500 nm [196, 197]. In addition to physically trapping larger materials, the hydrophobic domains and negatively charged glycosylation on mucins entrap positively charged and hydrophobic materials [198]. In the gastrointestinal tract (GI) mucus serves as a lubricant for food, and as a barrier against

pathogens, digestive enzymes and acids, digested food particles, microbial by-products, food-associated toxins. Mucus also serves as the microenvironment for the commensal GI microbiome [199, 200]. Understanding GI mucus structure is particularly important, as it is not only affected by disease, but can also modulate drug absorption – a key area of study to better design orally-delivered medications. However, it is difficult to access human GI tissues and thus access to human mucus samples has been extremely limited. In the last two decades, many *in vitro* models of the GI tract have been developed to both address questions about GI physiology, and to study therapeutic absorption and toxicity to improve drug and drug delivery designs.

The most traditional GI *in vitro* models use Caco-2 cells, an immortalized human colorectal adenocarcinoma cell line. These cells grow into confluent monolayers, differentiate into polarized enterocyte-like cells, and have been used extensively to screen for the permeability and toxicity of drugs[201-203]. Caco-2 Transwell® models have been shown to recapitulate the transport of insulin, calcitonin, and exenatide that is found in *ex vivo* models[204]. However, a main criticism of the use of these Caco-2 models[204] is that, contrary to using the established 21-day culture period typically used to generate Caco-2 models, many reports cultured models for only 3-5 days prior to performing experiments, not allowing for differentiation into more representative GI epithelial cells[205]. Indeed, culturing conditions have been shown to massively affect how Caco-2 cells behave *in vitro*. Caco-2 cell models have been shown to increase in TEER and metabolic gene expression as passage number increases[206]. Also, studies on mannitol permeability across Caco-2 monolayers have demonstrated that permeability declines over culturing time, leveling off after 21 days, suggesting complete differentiation at this point[207]. Caco-2 cell layers have also been effective in demonstrating the toxicity of both new drug formulations, and environmental hazards, such as microplastics[208]. Collectively, Caco-2 Transwell® models have proven to be a

valuable tool to model the absorptive qualities of the GI tract, but they lack the mucus layer that covers the GI epithelium which can modulate transport of materials toward it, thus affecting absorption.

Addition of a mucus layer is crucial to building physiologically relevant GI *in vitro* models[192, 209]. In recent years, a new cell line has emerged, HT29-MTX, that form goblet-like cells which produce mucus. Co-culturing HT29-MTX cells with Caco-2 cells generates GI epithelial models with similar gene expression profiles to GI tissue, and results in a mucus layer on top of the epithelium[210]. Studies have examined how modifying the ratio of HT29-MTX cells to Caco-2 cells can change the properties of the epithelial layer, including the thickness of the mucus produced and the resistance across the GI model. Results of these studies have been relatively variable, generally indicating that the inclusion of HT29-MTX goblet cells results in a reduction of transepithelial resistance (TEER), and an increase in mucus height, measured using microscopy[211]. Mucus layers produced by these models have been found to be 10 – 50 μm in size[212, 213], and these coculture systems have largely been used to study how mucus affects drug and nutrient bioavailability[203]. Interestingly, cocultures with 10-20% HT29-MTX cells better recapitulate iron absorption trends, despite Caco-2 cells being the main contributor of iron transporters, suggesting that the inclusion of goblet-like cells modulates enterocyte physiology[214].

While new GI *in vitro* models now usually include mucus-producing cells, characterization of the mucus in these model systems has been extremely limited. Typically, analysis of mucus from *in vitro* models consists of measuring electrical resistance, MUC2 (the primary mucin found in GI mucus) protein content, mucin gene expression in goblet cells, and imaging[215, 216] [217]. These methods are useful for confirming the presence of mucus; however, they provide relatively little

information about the biophysical properties of the mucus produced by these cultures. The biophysical properties of mucus can affect its functions as a lubricant, mesh-like sieve, and homeostatic environment for the microbiome[218]. One key method to study the biophysical properties of mucus is rheology, but the limited volume of mucus produced by 1 cm^2 or smaller Transwell® models, makes use of traditional rheometers difficult, as these require >100 µL of mucus[219]. Determining microrheology through multiple particle tracking (MPT) is a useful method to gain insight into the micron-level mechanics of mucus and can be performed using the low volumes produced by *in vitro* culture models[220, 221]. MPT has already been used to determine pore sizes in vaginal, GI, and respiratory mucus[222-224]. In this study, we generated a coculture GI epithelial model using Caco-2 enterocyte-like cells and HT29-MTX goblet-like cells. We modified the ratio of the two cell types to simulate physiologically relevant cell numbers throughout the GI tract and determined its effect on the biophysical properties of the mucus within the model. We examined traditional hallmarks including epithelial morphology, TEER, and permeability, provided biophysical analysis of the mucus layer, and compared mucus properties to that of intestinal mucus from two common animal models: mice and pigs.

8.2 Methods

8.2.1 Cell Culture

Caco-2 (p44-48) and HT29-MTX cells (p32-40) were cultured in 75-cm^2 plastic flasks (Nunc EasyFlask Thermo Scientific, Nuclon Delta Surface). Culture medium consisted of Dulbecco's Modified Eagle's Medium with 10% Fetal Bovine Serum (Gibco) for both Caco-2 and HT29-MTX lines. Coculture of Caco-2 and HT29-MTX was performed at the following ratios of Caco-2:HT29-MTX: 1:0, 9:1, 4:1, and 0:1. Cells were seeded at a total density of 375,000 cells/cm^2 in

1.0 μm pore size cell culture inserts (PET, Falcon) in a 12 Well Tissue Culture Plate (Falcon). Cocultures were maintained for 21 days to allow Caco-2 cells to differentiate and develop enterocyte-like features. All cultures were kept at 37°C in 5% CO_2, 95% air atmosphere and regularly checked every other day to change medium. Mucus was washed from cultures using phosphate buffered saline (PBS) weekly. Trans epithelial electrical resistance (TEER) was measured on day 7, 14, and 21 using a millicell ERS-2 voltohmmeter (Millipore Sigma). Viability was assessed through staining with propidium iodide (PI; 81845, Sigma). PI was administered to live cultures after 21 days of culture on 24 well plates (Nunc Thermo Scientific) at a concentration of 30 μM in PBS for 15 minutes in the dark. Cells were stained with propidium iodide and imaged using fluorescence microscopy to identify non-viable cells.

8.2.2 Immunofluorescence Staining

Coculture Transwell© inserts were fixed with 4.0% cold Paraformaldehyde (PFA) in PBS for 15 min. Samples were then washed 3 times with PBS and kept at 4°C. Membrane inserts were cut out and placed cells-up on microscope slides. Samples were permeabilized using 0.1% triton X-100 for 15 minutes. Samples were blocked with 2% FBS in PBS for 30 minutes and then washed with PBS times. Primary antibody (anti-EpCAM, anti-MUC2 abcam) was diluted 1:200 in blocking solution and applied to samples for 2 h at room temperature. Primary antibody was then removed, and the sample was washed twice with PBS containing 0.1% Tween 20 and 3 times with PBS. Secondary antibody and phalloidin-AF555 (Invitrogen) were applied for 2 h at room temperature (Invitrogen). Cover slips were mounted on the samples with Vectashield Antifade Mounting Medium with DAPI and sealed with nail polish prior to imaging. Fluorescence imaging was performed using an Olympus FV300 Laser Scanning Confocal Microscope. Mucus height was determined by measuring the distance the fluorescently labeled mucus layer spanned using ImageJ

(NIH). Briefly, XZ confocal projections stacks were averaged over the Y axis. Mucus ROI was traced and average height was recorded for each confocal image. 6 images were taken from n = 4 samples.

8.2.3 Coculture Permeability

Cocultures were generated on 1.0 μm transwells and cultured for three weeks as described above. On day 21 10 μg/mL fluorescent 150 kDa Dextran, 4 kDa Dextran, or AF647-labeled albumin (Invitrogen) was added to the top well and transport to the bottom well was measured via fluorescence (Tecan Spark microplate reader) hourly for up to 6 h. Fluorescence intensity was quantified using a plate reader and tracer transport was calculated using a standard curve. Effective permeability was estimated using the equation: $\boldsymbol{P_{eff}} = \frac{\boldsymbol{C_{lower}V_{lower}}}{\boldsymbol{tSC_{initial}}}$, where C = concentration, V_{lower} = volume of the bottom compartment, S = surface area, and T = time.

8.2.4 Microrheology

Non-mucoadhesive nanoparticles were generated using previously published methods[95, 224, 225]. Briefly, commercially available fluorescent 100 nm, carboxyl-modified polystyrene nanoparticles (Invitrogen) were coated with 5 kDa polyethylene glycol (PEG, Creative PEGworks) using EDC/NHS chemistry. PEG coating was confirmed using dynamic light scattering (DLS, Brookhaven Scientific). Mucus was collected from the surface of the transwells and 0.5 μL of nanoparticles at 1E-5 w/w%, or 1 μg/mL. All tracking was performed on day 21 of coculturing using an Axio Observer fluorescence microscope. Images were recorded at a frame rate of 30 frames per second. Centroid tracking was performed using automated MatLab software package based on a previously developed method [226]. Briefly, the 2D localization of fluorescent nanoparticles was determined based on an intensity and eccentricity threshold. Trajecotries were

determined by connecting particle centers between serial images. The Mean Squared Displacement (MSD) can be calculated as: $<\Delta r2(\tau)> = <[x(t + \tau) – x(t)]2 + [y(t + \tau) + y(t)]2>$, where τ is the time lag between frames and angle brackets denote the average over the time points of interest. The MSD was then used along with the Stokes-Einstein equation to calculate the viscosity: MSD=4Dt; D=k_B T/6πηr where: D = Diffusivity Constant, k_B = Boltzmann's, Constant, r = Radius of nanoparticle, T = temperature, t = time, and η = Viscosity. Using these equations, we can determine the viscosity of the mucus. Further viscoelastic properties of the mucus was determined using the generalized Stokes-Einstein equation which relates the viscoelastic spectrum [G(s)] to the Laplace transform of $<\Delta r2(\tau)>$, $<\Delta r2(s)>$, with the equation $G(s) = 2kBT/[\pi as<\Delta r2(s)>]$, where kBT is thermal energy, a is particle radius, and s is the complex Laplace frequency[220]. Making the substitution *s* with *i*ω where i is a complex number and ω is frequency, the complex modulus can then be calculated as G*(ω) = G'(ω) + G"(iω). The viscous and elastic moduli, G'' and G' can be calculated using the expression for complex microviscosity, η*(ω) = G*(ω)/ω. The pore size of the mucus hydrogel (ξ) can be estimated based on measured G' as $\xi \approx (kBT/G')1/3$ [227, 228].

For animal studies, female C57Bl/6J mice 8-10 weeks old were purchased from Jackson Labs and allowed to acclimate for up to 14 days. Porcine intestine samples were obtained from Animal Biotech Industries (ABI, Doylestown PA). Animal tissues were harvested and 5 µL of 1.0 µg/mL nanoparticles were added to the mucus covering the epithelial surface, without freezing or washing tissue to preserve mucus integrity. Microrheology was performed as described above. All animal studies were approved by the UMD IACUC.

8.2.5 Statistics

Group analysis was performed using a 2-way ANOVA, followed by Tukey's post-test. Unpaired Student's t-test was used to examine differences between only two groups. A value of $p < 0.05$

was considered significant (GraphPad). All data is presented as mean ± standard error of the mean (SEM). All experiments were performed at least twice with 2-3 technical replicates per condition. Only statistically significant or trending ($p \leq 0.1$) data is indicated in the Figures.

8.3 Results

We sought to generate a model GI epithelium with physiologically relevant mucus by coculturing HT29-MTX mucus producing goblet-like cells with Caco-2 enterocyte-like cells. Caco-2 cells and HT29-MTX cells were seeded at four different ratios: 1:0, 9:1, 4:1, and 0:1 Caco-2:HT29-MTX (CH10:0, CH9:1, CH8:2, CH0:10, respectively), representative of the jejunum and ileum of the small intestine [229]. Cells were cultured for 21 days on a 1.0 um Transwell© insert at confluence to allow differentiation of Caco-2 cells into enterocyte-like phenotype. As expected, Caco-2 cells did not secrete mucus, and no secreted mucus layer was observed (**Figure 1A**) [230]. We found that f-actin is localized to cell membranes, particularly along the apical surface of the epithelial layer, and is most evident in cultures containing Caco-2 cells (**Figure 1A, Sup 1**). As HT29-MTX cells are added, the signal and continuity of the f-actin is reduced, but monolayer integrity is maintained, as no obvious gaps between cells can be observed. We found that the MUC2 secreted mucus layer increases in height as the amount of HT29-MTX cells in the culture is increased (**Figure 1A-B**). The mucus layer height is tallest on the cultures containing only HT29-MTX cells: 175 ± 37 μm, and smaller in the cocultures: 48 ± 13 μm for CH9:1, and 94 ± 10 μm for CH8:2 (**Figure 1B**). It is difficult to differentiate Caco-2 and HT29-MTX cells, since both express mucin and other typical GI epithelial genes/proteins, and thus it is possible that the original 9:1 and 8:2 ratios have changed throughout our culture even though cells are seeded at confluence. However, the changes we see in mucus accumulation, and f-actin signal suggest that even if the original

ratios are not maintained after 21 days, the HT29-MTX cell population is different between the two conditions. Coculture viability was close to 100% for all conditions (**Figure 1C**).

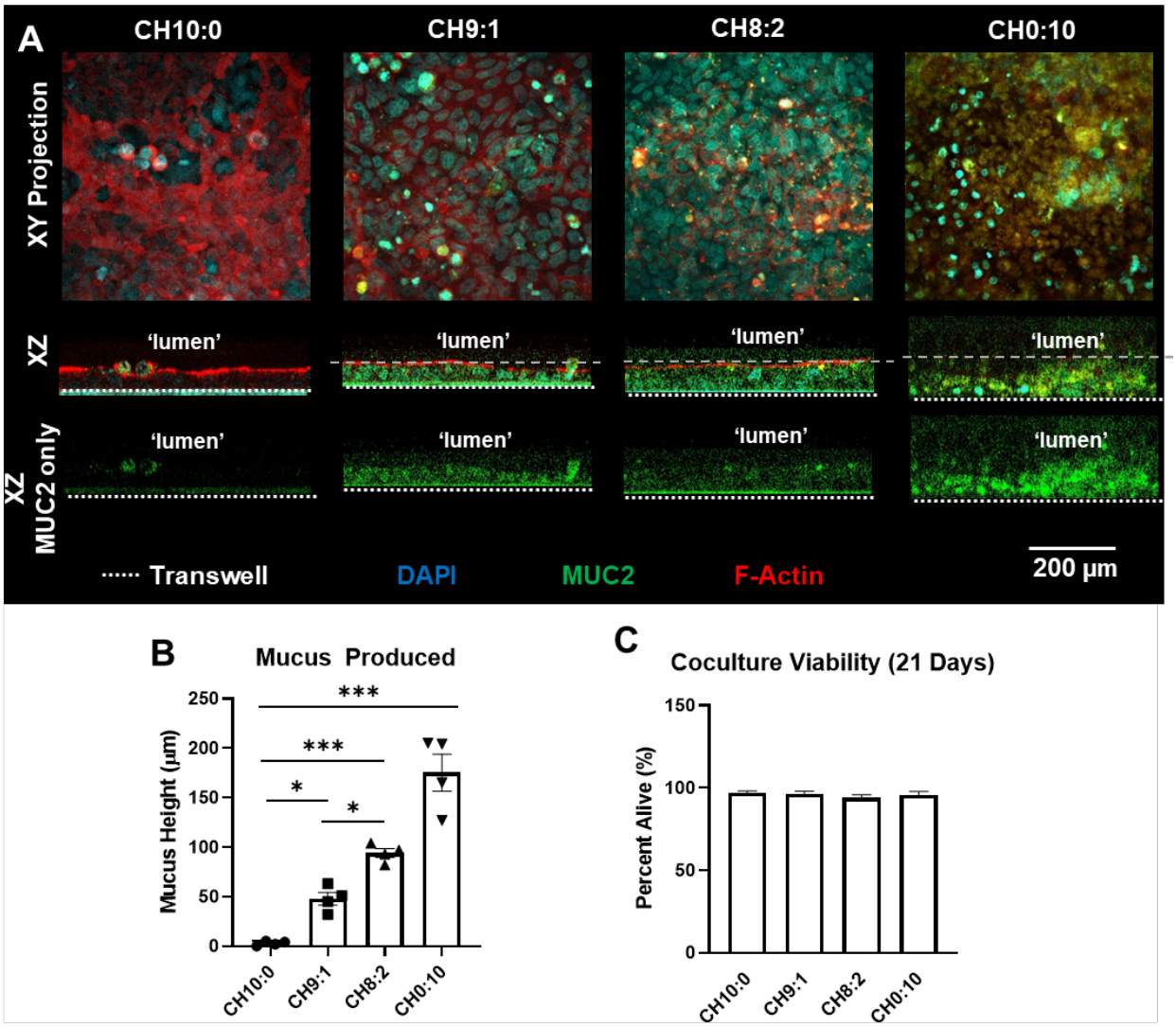

Figure 1 *Morphology and Physiology of GI Co-Culture Models*

A) Immunofluorescence images of different co-culture conditions visualizing cytoskeletal F-actin (Phalloidin, red), mucin (MUC2, green) and nuclei (DAPI, blue). Grey dashed lines indicate representative location from which mucus height was measured and white dashed lines indicate location of the transwell membrane. B) Quantification of mucus head produced. C) Viability of coculture models at maturity (21 days). n = 4 (*P < 0.05, *** P < 0.001) measured using 1-way Anova. Scale bar indicates 200 µm.

After characterizing the morphology of the different GI cocultures, we sought to assess the effect of a mucus layer and HT29-MTX cells on model GI epithelial permeability. We found that TEER increased from 330 ± 30 to 440 ± 110 mV to 510 ± 60 mV for CH10:0 and from 180 ± 20 to 260 ± 30 mV to 230 ± 40 mV for CH0:10 (**Figure 2A**). Both mixed cultures also increased over time, with the CH9:1 culture increasing from 370±10 to 530±30 mV to 570 ± 50 mV and the CH8:2 culture increasing from 420 ± 20 to 550 ± 20 mV to 610 ± 40 mV (**Figure 2A**). We observed an increase in TEER with the addition of HT29-MTX cells to the culture across all time points. We also assessed solute permeability of the coculture model using fluorescent bio-inert 150 kDa dextran, 4 kDa dextran, and albumin, a model protein. Using the 4 kDa dextran tracer, commonly used in studying epithelial permeability, we observed that the HT29-MTX monoculture was the most permeable with 9.1 ± 0.8 % transport. This was significantly higher than the CH9:1 and CH8:2 cocultures where the 4 kDa transport efficiency was 3.5 ±0.2% and 4.0 ± 0.6% respectively. The Caco-2 monoculture was the least permeable to 4 kDa dextran with a transport efficiency of 1.5 ± 0.1% (**Figure 2B)**. The other coculture conditions, CH10:0, CH9:1, and CH8:2, displayed similar transport efficiency, ranging from 2.5 ± 0.1% - 2.5 ± 0.2% after 6 hours. Measuring the trans-epithelial transport of the 150 kDa dextran, we found that the uniform HT29-MTX culture was the most permeable to this larger molecule, with 3.0 ± 0.6% transport efficiency (**Supp 2**). Albumin transport was similar for all Caco-2 containing samples, though there was a trend toward lower permeability of the CH9:1, and the HT29-MTX culture was most permeable with 5.7±3.7% of the albumin transported after 6 h (**Figure 2C**). Our data demonstrate that the effective permeability for 4kDa dextran was the highest for the HT29-MTX monoculture (Figure 2D, Supp 2), and the other cell compositions displayed similar effective permeabilities for the different tracers (**Figure 2D-E, Supp 2**).

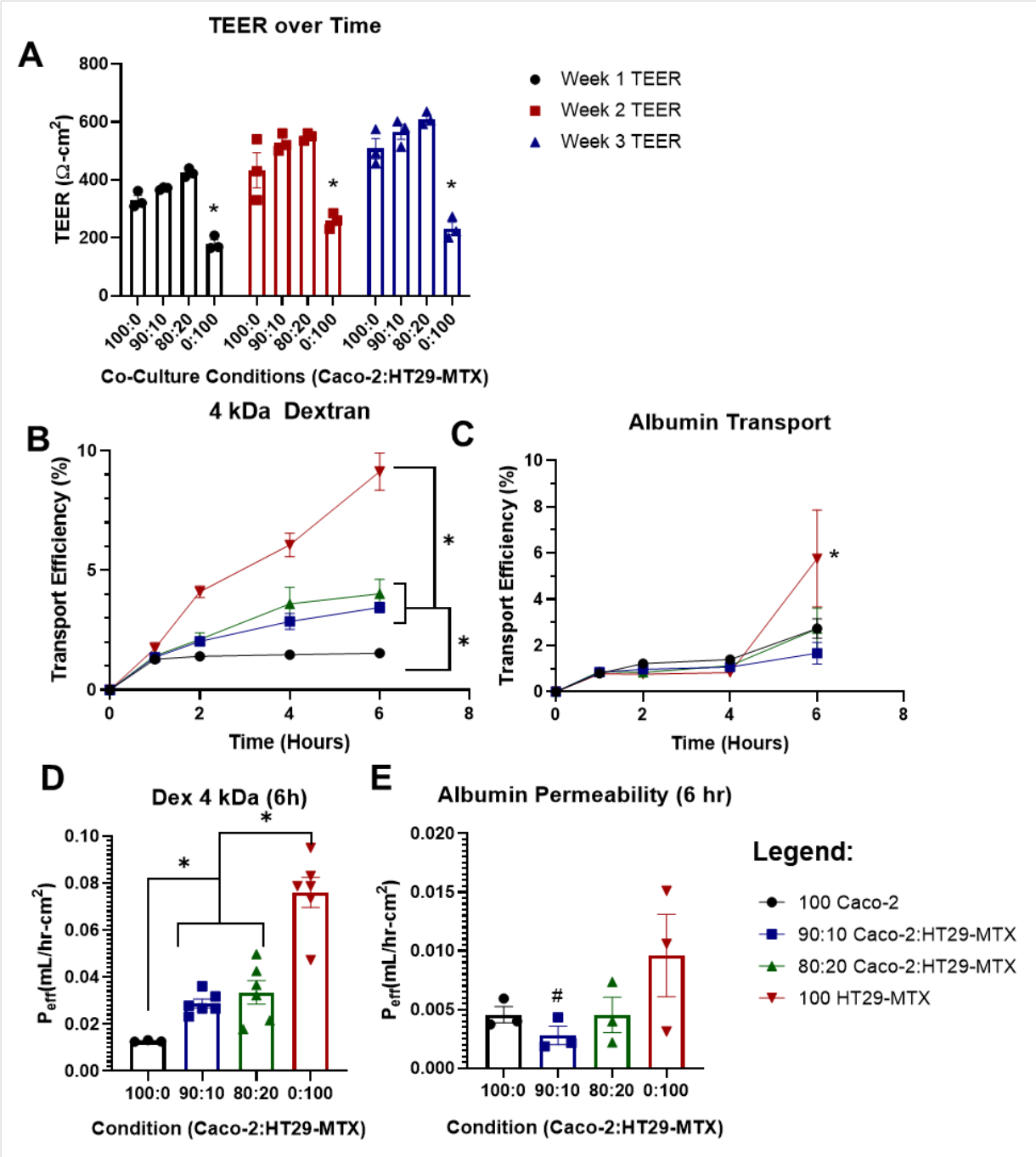

Figure 2 *Permeability of GI Co-Cultures*

A) Trans-Epithelial Electrical Resistance (TEER) of co-cultures over time. B) 4 kDa dextran and C) albumin transport efficiency across the transwell coculture over time after 3 weeks. Calculated permeability of cocultures at 6h to D) 4 kDa Dextran and E) albumin after 3 weeks. n = 3 – 6 (*$p < 0.05$, #$p < 0.1$) measured using 2-way Anova.

Next, we characterized the rheological properties of the mucus layer in our coculture model systems using MPT. As the Caco-2 cell lines do not secrete a mucus layer, we did not measure rheological properties of the CH10:0 coculture model. We found that MSD and diffusivity increased as the ratio of HT29-MTX cells within the culture increased. PEGylated non-mucoadhesive nanoparticles (MPP) displayed a diffusivity of 0.11 ± 0.2 $\mu m/s^2$ in CH9:1 mucus, and 0.12 ± 0.01 $\mu m/s^2$ in CH8:2 mucus. MPPs within mucus samples from goblet-cell monocultures (CH0:10) had a diffusivity of 0.13 ± 0.01 $\mu m/s^2$ (**Figure 3A**), indicating that all cultures had similar diffusivities. We found that the viscosity of the CH9:1 mucus was 0.03 ± 0.01 Pa-s (**Figure 3B**). The mucus of the CH8:2 mucus was ~25% more viscous than CH9:1 mucus, at 0.04 ± 0.01 Pa-s (**Figure 3B**), while CH0:10 mucus was the most viscous at 0.045 ± 0.01 Pa-s ($P<0.2$), though none of these differences were statistically significant (**Figure 3B**). We then extrapolated pore size of the mucus layers and found that there was a relatively large variability. We found that the average pore size was 440 ± 15 nm^2 in the CH9:1 mucus, 610±30 nm^2 in the CH8:2 mucus, and 620 ± 70 nm^2in the CH0:10 mucus, with CH9:1 mucus having a significantly lower pore size than both CH8:2 and CH0:10 (**Figure 3C**). However, pore sizes ranged from 10 to 1200 nm^2 for CH9:1 and 10 to 2800 nm^2 for CH8:2, highlighting the heterogeneity of the produced mucus layer (**Figure 3C**). Finally, we determined the elastic (storage) modulus (G') and plastic (loss) modulus (G''). G' at τ=0.5s was similar at 0.15 ± 0.06 Pa and 0.20 ± 0.12 Pa (ns) for CH9:1 vs. CH8:2, respectively (Figure 3D). The monoculture of HT29-MTX goblet-like cells had the highest elastic modulus of 0.48 ± 0.19 Pa, though due to the high variability this was only a trend when compared to CH9:1 (**Figure 3D**). The plastic modulus and ratio between G'/G" was highest for HT29-MTX monocultures (**Figure 3E-F**). Interestingly, when measuring G''/G' we

saw that the mucus produced by the cocultures behaved elastically (G''/G' < 1), whereas the monoculture of HT29-MTX cells was slightly plastic (G''/G' $\geq$ 1) (**Figure 3F**).

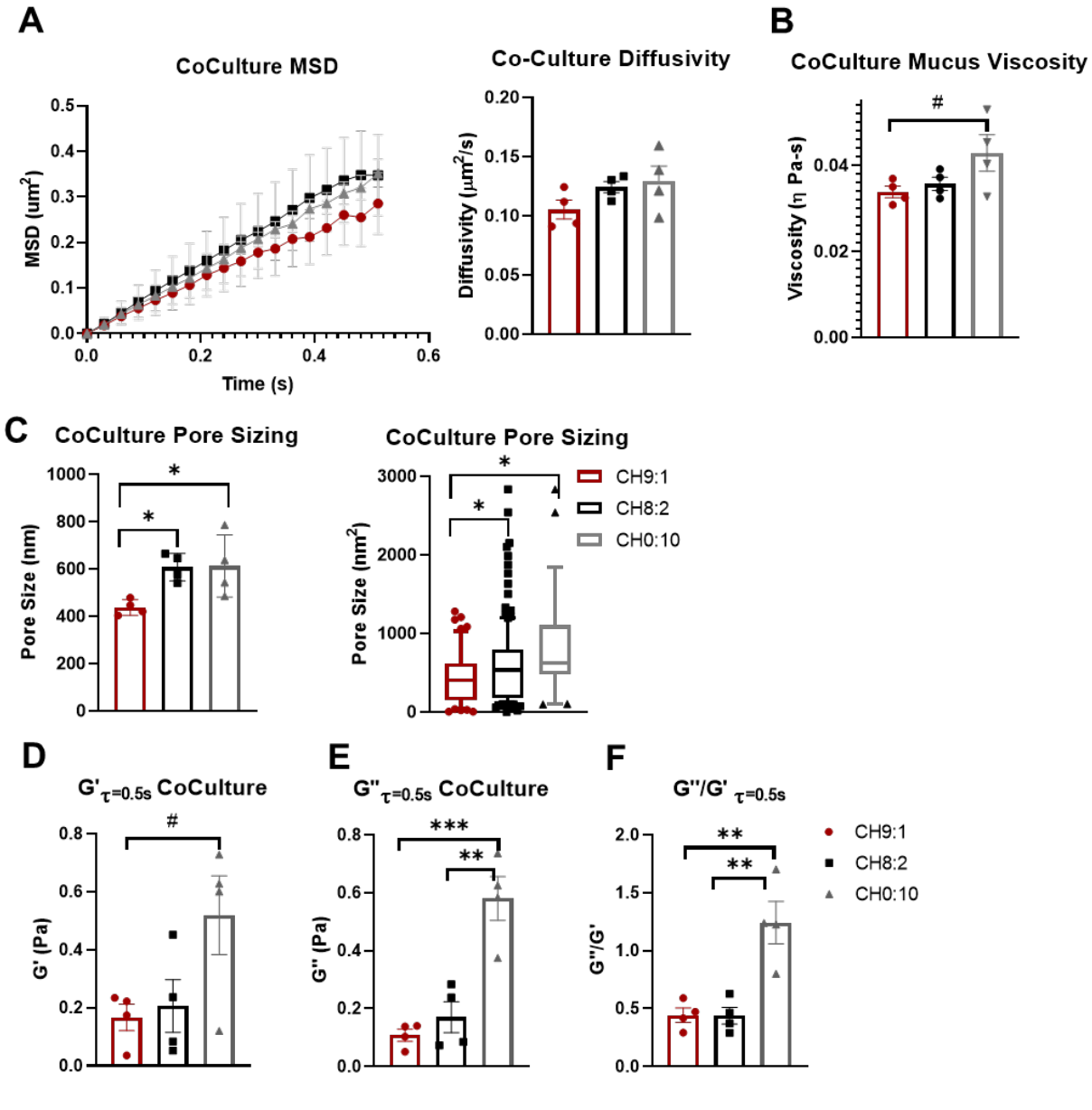

Figure 3 *Material Properties of Mucus Produced by Coculture Models after 3 Weeks*

A) Diffusivity of 100 nm PEGylated nanoparticle in culture-produced mucus samples. B) Microvisocisty, C) pore size D) elastic modulus (G'), E) plastic modulus (G''), and F) G''/G' of mucus produced by cocultures after 3 weeks. n = 4-6 (#P < 0.1; *P < 0.05;) measured using 2-way ANOVA for MSD and 1-way ANOVA otherwise.

To determine if the properties of the mucus produced in our *in vitro* model was representative of *in vivo* mucus, we collected GI mucus from mice and pigs, two animal models commonly used for studying the GI tract. We compared the mucus properties in both the jejunum and ileum of the small intestines. We found that there was a trend toward higher MPP diffusivity within the jejunum when compared to the ileum for both porcine and murine mucus samples (**Figure 4A**). MPP diffusivity was 0.40 ± 0.1 to 0.20 ± 0.1 $\mu m/s^2$ for the porcine samples and 0.30 ± 0.1 to 0.19 ± 0.1 $\mu m/s^2$ for the murine mucus samples. We also found that porcine jejunal mucus had a viscosity of 0.034 ± 0.01 Pa-s, less viscous than porcine ileal mucus, which had a viscosity of 0.087 ± 0.01 Pa-s (**Figure 4B**). The porcine jejunal mucus displayed similar microviscosity measurements to both coculture models 0.036 ± 0.002 Pa-s and 0.034 ± 0.001 Pa-s for CH9:1 and CH8:2, respectively. Murine mucus viscosity was higher in the jejunum compared to porcine jejunum, measuring 0.07±0.02 Pa-s in the murine jejunum, and was similar to porcine ileal mucus, measuring 0.10 ± 0.03 Pa-s in the murine ileum (**Figure 4B, Table 1**). We found that pore size was consistently below 500 nm^2 for all porcine and murine small intestinal mucus samples (**Figure 4C**). Porcine jejunal mucus had a mucus pore measuring 390 ± 50 nm^2, similar to the mucus produced by the CH9:1 coculture model (440 ± 15 nm^2) (**Figure 4C**). Calculating the material properties of the animal mucus, we found that both were elastic in nature, evidenced by the ratio of G''/G' < 1 (**Figure 4D-F**), similar to our coculture in vitro models. Collectively, these results indicate that there are similarities in material properties between the mucus produced by the *in vitro* models and mucus from *in vivo* animals (**Table 1**). Additionally, we identified that the ratio of 90:10 Caco-2 to HT29-MTX cells recapitulated the viscosity, pore size, G' and G" of porcine jejunal mucus (**Table 1**).

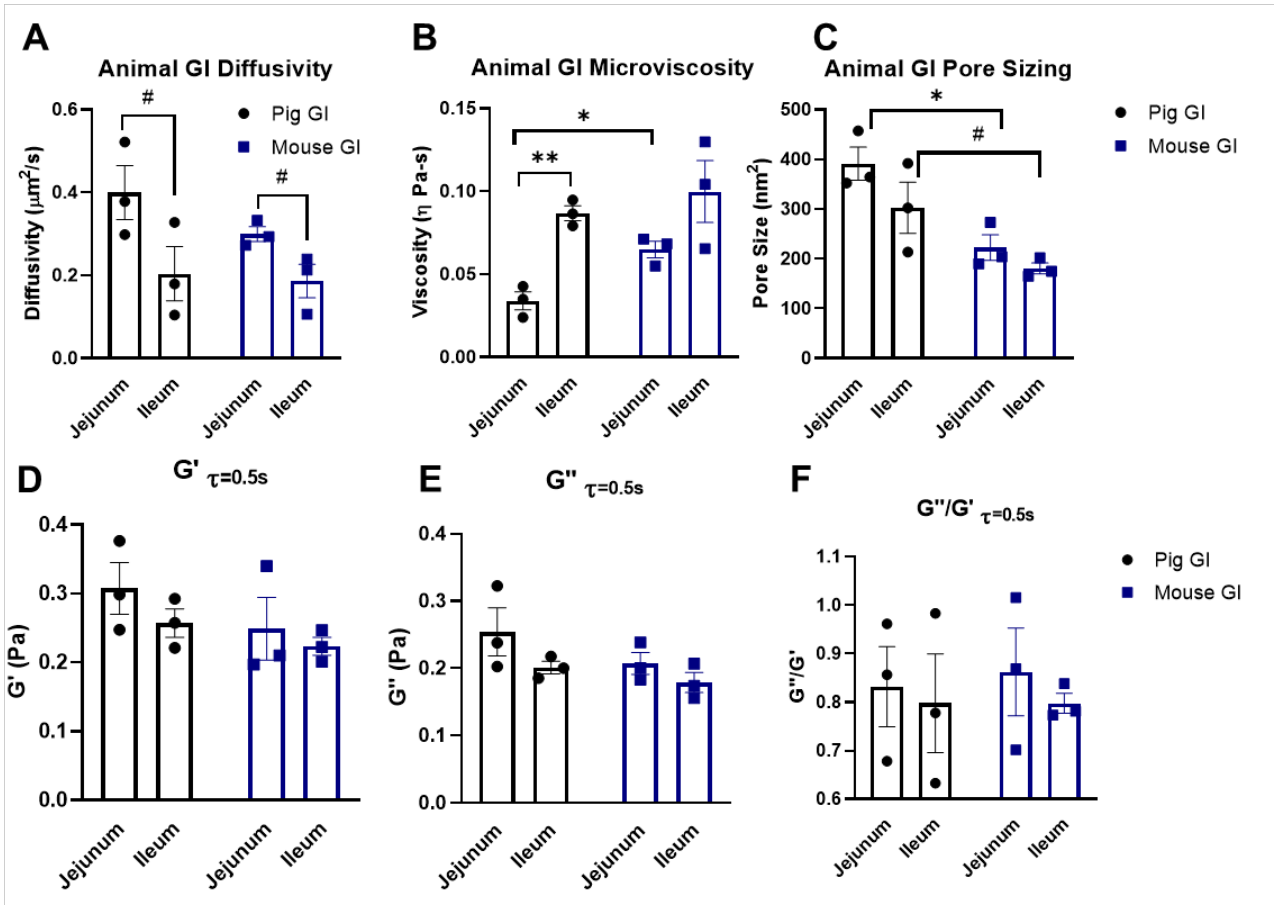

Figure 4 *Material Properties of Mucus from In-Vivo Animal Models*

A) Diffusivity of 100 nm PEGylated nanoparticle in collected mucus samples. B) Calculated microvisocisty of mucus samples. C) Pore size of mucus samples D) elastic modulus (G'), E) plastic modulus (G''), and F) G''/G' of mucus. n = 3 (#: $p = 0.054$; *$p < 0.05$) measured using Student's t-tests.

		Viscosity (Pa-s)	Pore Size (nm^2)	G' (Pa)	G" (Pa)	G'/G"
Caco-2: HT29-MTX	**9:1**	**0.034 ± 0.001 &**	**440 ± 50 &**	**0.16 ± 0.05 &, @, &, @**	**0.11 ± 0.02 &**	**0.44 ± 0.06**
	8:2	**0.036 ± 0.002 &**	**600 ± 40**	**0.21 ± 0.09 &, @, &, @**	**0.17 ± 0.05 &**	**0.44 ± 0.07**
	0:10	**0.043 ± 0.004**	**830 ± 120**	**0.52 ± 0.13**	**0.58 ± 0.07**	**1.24 ± 0.18**
Mouse	**Jejunum (&)**	**0.065 ± 0.009**	**220 ± 30**	**0.25 ± 0.05**	**0.21 ± 0.02**	**0.86 ± 0.09**
	Ileum (@)	**0.100 ± 0.032**	**180 ± 10**	**0.22 ± 0.01**	**0.18 ± 0.02**	**0.8 ± 0.02**
Pig	**Jejunum (&)**	**0.034 ± 0.009**	**390 ± 30**	**0.3 ± 0.04**	**0.25 ± 0.04**	**0.83 ± 0.08**
	Ileum (@)	**0.087 ± 0.008**	**300 ± 50**	**0.26 ± 0.02**	**0.2 ± 0.01**	**0.8 ± 0.1**

Table 1: *Summary of material properties of different co-culture systems compared to pig and mouse mucus.*

Values given as mean ± SEM (n=3-6) measured using 1-way Anova. Symbol (& for jejunum or @ for ileum, mouse – blue, pig – red) indicates that the measured parameter (viscosity, etc) for the coculture model is not statistically different or trending toward a difference compared to the respective animal mucus ($p > 0.1$).

8.4 Discussion

In this work we established an *in vitro* model of the mucus-producing GI epithelium and characterized the permeability of the model as well as the material properties of the mucus produced by the model. We found that increasing the number of HT29-MTX cells within our culture model resulted in more mucus production, as indicated by an increase in mucus height. The addition of HT29-MTX cells, and thus a mucus layer, resulted in an increase in TEER, but did not significantly affect the model's permeability of the albumin and 4 or 150 kDa dextrans compared to Caco2 cells alone. Our microrheological analysis revealed that the mucus became more viscous and contained larger pores as the amount of HT29-MTX cells was increased. Interestingly, we show that the mucus produced by the coculture was distinct from the mucus produced by the HT29-MTX cells alone, as the mucus produced by the cocultures was more viscoelastic than that produced by the monoculture of HT29-MTX cells. The mucus produced by the coculture models was also less viscous than that found in both the porcine and murine GI mucus. In summary, we generated and characterized an *in vitro* model for the GI epithelium that can inform oral drug delivery strategies while providing some of the first analyses of the mucus layer produced by an *in vitro* GI model.

Studies have found that the addition of a mucus layer via coculture of HT29-MTX and Caco-2 cells does not modulate permeability of the *in vitro* model system compared to Caco-2 cells alone[231-233]. Our study confirms these findings: We found that changing the ratio of cells within our culture did not change the permeability of 4 or 150 kDa dextran and albumin. Others have also reported that the addition of HT29-MTX cells does not change the permeability of chemical, macromolecule, or protein tracers in a significant way [231, 233]. However, permeability is increased in monocultures of HT29-MTX cells, likely due to their lack of forming

adequate tight junctions. Similarly, literature suggests that addition of HT29-MTX cells modifies formation of tight junctions between the enterocyte-like cells, which has been observed in numerous other studies using coculture ratios ranging from 70:30 – 90:10 Caco-2 to HT29 cells, and occurs because the goblet-like cells do not adequately form tight junctions themselves[211, 234, 235]. Despite this, other groups found that changing the ratios of the cell types did not alter the TEER values measured[235, 236]. This is contrary to what we have observed, where the introduction of HT29-MTX cells seems to have increased the TEER of our models. This inconsistency may be caused by the thicker mucus layer in our system, which may alter the TEER readings. Despite the differing trends in TEER as a result of the addition of HT29-MTX cells, TEER values for cocultures range from 300-900 Ω-cm^2, which is consistent with our models. Another consideration for models utilizing differing ratios of Caco-2 and HT29-MTX cells is that due to the challenge of definitively identifying them through imaging, it can be difficult to establish that the original ratio of cells are maintained due to different proliferation rates. Overall, our system recapitulates the permeability and mucus production of previously developed *in vitro* model systems.

Mucus height changes throughout the different parts of the GI tract, which is unsurprising since the jejunum, ileum, and colon have distinct functions – food digestion/absorption in the small intestine and water/ion absorption in the colon. The duodenum has the thickest mucus layer, measuring up to 500 microns[218], likely to prevent the incoming gastric juices and digestive enzymes from reaching the epithelial surface too quickly. In the jejunum, mucus thickness is only 150-300 microns, likely to aid in food absorption, while the mucus layer in the ileum can measure up to 500 microns in thickness [212]. These values are much greater than those recreated in classic *in vitro* models using 70:30 – 90:10 ratio of Caco-2 to HT29-MTX coculture models of the GI

tract, where mucus thickness mostly resembles that of the firmly adherent mucus layer, ranging from 15 – 30 microns in the small intestine[194, 213, 215, 237]. Navabi et al completed a thorough study where they examined a combination of Caco-2 and HT29-MTX ratios and strains, and the effect of mechanical stimulus on mucus production. The mucus layer produced by their models was consistently thinner than that of our model[237]. Our model system had mucus of 40 – 80 microns, suggesting that our system includes a thicker mucus layer than previously reported systems, which may make it more physiologically representative. Further optimization to enhance the height of the mucus layer *in vitro* may be needed to build truly representative *in vitro* model systems.

In addition to mucus height, the material properties of the mucus change along the different parts of the intestine. Studies in mice have suggested that mouse colonic mucus has an average pore size close to 200 nm, as 200 nm, non-mucoadhesive nanoparticles had reduced diffusivity in the mucus layer[224]. Mouse small intestinal mucus, on the other hand, had a larger pore size ranging between 200 – 500 nm, as 200 nm nanoparticles freely diffused with the mucus gel, while 500 nm nanoparticles did not[223]. Studies using reconstituted porcine-derived mucin have estimated that the pore size of small intestinal mucus lies between 100 – 200 nm in size[238]. This has been corroborated by Yildiz et al. who observed a 20-fold decrease in particle diffusivity when nanoparticle diameter was increased from 100 nm to 500 nm, suggesting that the pore sizes within porcine mucus lie between 100 – 500 nm[239]. A confounding factor in many of these studies is that the reliance on mucus hydrogels generated from purified and heavily processed gastric mucins, instead of small and large intestinal mucins, which can lead to gels that do not necessarily recapitulate the mucin seen *in vivo*[240]. Indeed, electron micrographs of *ex vivo* mucus highlight the heterogeneity of mucus pore sizes *in vivo* and provide a visual estimation of pore size closer to

500 nm diameter[241]. One group demonstrated that microparticles of 0.5 – 2 μm^3 were able to diffuse through murine ileal mucus samples, suggesting that mucus pore sizes could be as large as 2 μm^2 [242]. Our data shows that coculture in vitro models produce mucus with pore sizes more in line with that of estimated electron microscopy images of human mucus, a range of 50 - 300 nm in diameter[232]. Mucus pore size measurements have continued to result in seemingly conflicting data, which can largely be contributed to the myriad factors that can influence mucus permeability, including local concentrations of mucins and other macromolecules, fluid flow, presence of food materials, and diet. Collectively, these studies have suggested that pore sizes in mucus are extremely heterogeneous, which is recapitulated in our coculture models.

Mucus viscosity is key in maintaining barrier properties and is typically a function of pore size, with a tighter mesh network resulting in more viscous mucus. We found that the mucus from our cocultures had a viscosity of 0.03 - 0.04 Pa-s. This viscosity was below the reported ranges of 0.06 - 0.10 Pa-s in pig mucus, as measured via macrorheology[243]. However, differences in macro- and microrheology are common in other tissues as well. A similar study examining mucus barrier properties within different regions of the mucus layer corroborated our measurements of mucus microviscosity. Using MPT, they found that *ex vivo*, unmodified, jejunal porcine mucus had a microviscosity in the range of 0.01-0.05 Pa-s, and remained relatively similar at different depths of the mucus layer[219, 223, 244]. Despite these studies, how viscosity and pore sizes vary along the small intestinal tract is still largely understudied. Comparisons between small intestine mucus and colonic mucus suggest that viscosity of mucus increases as the GI tract progresses. Indeed, a study by Swidsinski et al. indirectly measured this gradient in mucus through analysis of the microbiome components within different regions of the GI tract[245]. Using agarose gel of different viscosities, they demonstrated that bacterial shape correlated with an environmental

viscosity best suited for survival and mobility. Through this, they hypothesized that the shape of bacteria in specific regions of the GI tract can predict the material properties of that region. Using this strategy, they further hypothesized that mucus viscosity increases from proximal to distal regions of the intestines. This trend is corroborated by our findings where our *ex vivo* microrheological measurements of porcine and mouse mucus indicate that viscosity increases from the jejunum to the ileum.

With inflammatory diseases at the forefront of *in vitro* modeling using Caco-2 and HT29-MTX cultures, many groups are also experimenting with adding immune cells into GI models. This is typically achieved through the addition of Raji B cells, microfold (M) cells, as well as THP-1-derived macrophages[246, 247]. Ude et al. incorporated Raji B cells within a Caco-2-based model of the GI tract to generate models sensitive to copper oxide pollutants[248]. Kerneis et al. added lymphocytes from Peyer's patches to a Caco-2 GI model. Within the model, these lymphocytes behaved like M cells, transporting inert nanoparticles and bacteria[249]. Beterams et al. recently developed a triple coculture model consisting of THP-1-derived macrophages, T84 epithelial cells, and LS-174T goblet cells[250]. They found that the inclusion of immune cells resulted in an increase in mucus height from 60 to 80 μm, compared to a coculture with no macrophages, suggesting that inclusion of immune cells is crucial to create a more physiologically representative mucus height. The group further introduced model microbiota which induced pro-inflammatory cytokine production. While these studies highlight the promise of modeling both microbiota and disease interactions *in vitro*, a key next step for these models will be to include the microbiota within a mucus gel in these models. This is incredibly challenging as most microbiota require anaerobic conditions, while epithelial cultures require oxygen. However, generating mucus

models with physiologically relevant material properties could facilitate the incorporation of microbiota and allow them to behave as they would *in vivo*.

In this study we demonstrated how coculture of enterocyte and goblet-like cells within a GI model resulted in physiologically relevant recapitulation of intestinal mucus properties. We found that increasing the number of goblet cells resulted in a more resistant monolayer, while also producing mucus that was more viscous with larger pores. Being able to accurately recapitulate both epithelium and mucus microenvironment is key for engineering oral therapeutics which must cross this barrier, as well as studying microbiome interactions with its physiologically relevant microenvironment. Future GI *in vitro* models should consider the material properties of the mucus produced, as features like pore size dictate microbiome health as well as drug delivery. Models can include additions such as immune cells and microbes to provide more physiologically relevant model systems.

9 References

1. Nakamura, T., et al., *The Effect of Size and Charge of Lipid Nanoparticles Prepared by Microfluidic Mixing on Their Lymph Node Transitivity and Distribution.* Molecular Pharmaceutics, 2020. **17**(3): p. 944-953.
2. Reddy, S.T., et al., *In vivo targeting of dendritic cells in lymph nodes with poly(propylene sulfide) nanoparticles.* Journal of Controlled Release, 2006. **112**(1): p. 26-34.
3. Maisel, K., et al., *Exploiting lymphatic vessels for immunomodulation: Rationale, opportunities, and challenges.* Advanced drug delivery reviews, 2017. **114**: p. 43-59.
4. Aspelund, A., et al., *Lymphatic System in Cardiovascular Medicine.* Circ Res, 2016. **118**(3): p. 515-30.
5. Scallan, J., V.H. Huxley, and R.J. Korthuis, *Integrated Systems Physiology: from Molecule to Function to Disease*, in *Capillary Fluid Exchange: Regulation, Functions, and Pathology*. 2010, Morgan & Claypool Life Sciences

Copyright © 2010 by Morgan & Claypool Life Sciences.: San Rafael (CA).

6. Baluk, P., et al., *Functionally specialized junctions between endothelial cells of lymphatic vessels.* J Exp Med, 2007. **204**(10): p. 2349-62.
7. Trzewik, J., et al., *Evidence for a second valve system in lymphatics: endothelial microvalves.* Faseb j, 2001. **15**(10): p. 1711-7.
8. Ikomi, F., et al., *Interstitial fluid, plasma protein, colloid, and leukocyte uptake into initial lymphatics.* Journal of Applied Physiology, 1996. **81**(5): p. 2060-2067.
9. Schulte-Merker, S., A. Sabine, and T.V. Petrova, *Lymphatic vascular morphogenesis in development, physiology, and disease.* J Cell Biol, 2011. **193**(4): p. 607-18.
10. Pflicke, H. and M. Sixt, *Preformed portals facilitate dendritic cell entry into afferent lymphatic vessels.* Journal of Experimental Medicine, 2009. **206**(13): p. 2925-2935.
11. Liu, J., et al., *Dendritic cell migration in inflammation and immunity.* Cellular & Molecular Immunology, 2021. **18**(11): p. 2461-2471.
12. Lucas, E.D. and B.A.J. Tamburini, *Lymph Node Lymphatic Endothelial Cell Expansion and Contraction and the Programming of the Immune Response.* Frontiers in Immunology, 2019. **10**.
13. Comerford, I., et al., *A myriad of functions and complex regulation of the CCR7/CCL19/CCL21 chemokine axis in the adaptive immune system.* Cytokine Growth Factor Rev, 2013. **24**(3): p. 269-83.
14. Haig, D.M., J. Hopkins, and H.R. Miller, *Local immune responses in afferent and efferent lymph.* Immunology, 1999. **96**(2): p. 155-163.
15. Geng, X., et al., *Multiple mouse models of primary lymphedema exhibit distinct defects in lymphovenous valve development.* Developmental biology, 2016. **409**(1): p. 218-233.
16. Breslin, J.W., et al., *Lymphatic Vessel Network Structure and Physiology.* Compr Physiol, 2018. **9**(1): p. 207-299.

17. Triacca, V., et al., *Transcellular Pathways in Lymphatic Endothelial Cells Regulate Changes in Solute Transport by Fluid Stress.* Circulation research, 2017. **120**(9): p. 1440-1452.

18. Sabine, A., et al., *FOXC2 and fluid shear stress stabilize postnatal lymphatic vasculature.* J Clin Invest, 2015. **125**(10): p. 3861-77.

19. Schwager, S. and M. Detmar, *Inflammation and Lymphatic Function.* Frontiers in Immunology, 2019. **10**.

20. Cromer, W.E., et al., *The effects of inflammatory cytokines on lymphatic endothelial barrier function.* Angiogenesis, 2014. **17**(2): p. 395-406.

21. Rahbar, E., et al., *Lymph transport in rat mesenteric lymphatics experiencing edemagenic stress.* Microcirculation, 2014. **21**(5): p. 359-67.

22. Zhang, F., et al., *Lymphatic Endothelial Cell Junctions: Molecular Regulation in Physiology and Diseases.* Frontiers in Physiology, 2020. **11**.

23. Dejana, E., et al., *Organization and signaling of endothelial cell-to-cell junctions in various regions of the blood and lymphatic vascular trees.* Cell Tissue Res, 2009. **335**(1): p. 17-25.

24. Schwartz, L.H., et al., *Prevalence and Importance of Small Hepatic Lesions Found at CT in Patients with Cancer.* Radiology, 1999. **210**(1): p. 71-74.

25. Yao, L.C., et al., *Plasticity of button-like junctions in the endothelium of airway lymphatics in development and inflammation.* Am J Pathol, 2012. **180**(6): p. 2561-75.

26. Yasumasa Kakei and Masaya Akashi and Takashi Shigeta and Takumi Hasegawa and Takahide, K., *Alteration of cell-cell junctions in cultured human lymphatic endothelial cells with inflammatory cytokine stimulation.* Lymphatic research and biology, 2014. **12 3**: p. 136-43.

27. Swartz, M.A., *The physiology of the lymphatic system.* Adv Drug Deliv Rev, 2001. **50**(1-2): p. 3-20.

28. Miteva, D.O., et al., *Transmural flow modulates cell and fluid transport functions of lymphatic endothelium.* Circ Res, 2010. **106**(5): p. 920-31.

29. Hematti, H. and R.J. Mehran, *Anatomy of the thoracic duct.* Thorac Surg Clin, 2011. **21**(2): p. 229-38, ix.

30. Casley-Smith, J.R., *The importance of the lymphatic system.* Angiology, 1985. **36**(3): p. 201-2.

31. Rockson, S.G., *Lymphedema.* Am J Med, 2001. **110**(4): p. 288-95.

32. Gupta, A. and J.A. Moore, *Lymphedema.* JAMA Oncology, 2018. **4**(5): p. 755-755.

33. Velanovich, V. and W. Szymanski, *Quality of life of breast cancer patients with lymphedema.* Am J Surg, 1999. **177**(3): p. 184-7; discussion 188.

34. Kobayashi, H., et al., *Delivery of gadolinium-labeled nanoparticles to the sentinel lymph node: comparison of the sentinel node visualization and estimations of intra-nodal*

gadolinium concentration by the magnetic resonance imaging. Journal of controlled release : official journal of the Controlled Release Society, 2006. **111**(3): p. 343-351.

35. Srinivasan, S., F.O. Vannberg, and J.B. Dixon, *Lymphatic transport of exosomes as a rapid route of information dissemination to the lymph node.* Scientific Reports, 2016. **6**(1): p. 24436.

36. Reddy, S.T., et al., *Exploiting lymphatic transport and complement activation in nanoparticle vaccines.* Nature Biotechnology, 2007. **25**(10): p. 1159-1164.

37. McCright, J., et al., *Dense poly(ethylene glycol) coatings maximize nanoparticle transport across lymphatic endothelial cells.* bioRxiv, 2020: p. 2020.08.01.232249.

38. Varypataki, E.M., et al., *Synthetic long peptide-based vaccine formulations for induction of cell mediated immunity: A comparative study of cationic liposomes and PLGA nanoparticles.* Journal of controlled release : official journal of the Controlled Release Society, 2016. **226**: p. 98-106.

39. Nishimoto, Y., et al., *Carboxyl-, sulfonyl-, and phosphate-terminal dendrimers as a nanoplatform with lymph node targeting.* International Journal of Pharmaceutics, 2020. **576**: p. 119021.

40. Rohner, N.A. and S.N. Thomas, *Flexible Macromolecule versus Rigid Particle Retention in the Injected Skin and Accumulation in Draining Lymph Nodes Are Differentially Influenced by Hydrodynamic Size.* ACS Biomaterials Science & Engineering, 2017. **3**(2): p. 153-159.

41. Kaminskas, L.M., et al., *PEGylation of polylysine dendrimers improves absorption and lymphatic targeting following SC administration in rats.* Journal of Controlled Release, 2009. **140**(2): p. 108-116.

42. Moghimi, S.M., et al., *Surface engineered nanospheres with enhanced drainage into lymphatics and uptake by macrophages of the regional lymph nodes.* FEBS Lett, 1994. **344**(1): p. 25-30.

43. De Koker, S., et al., *Engineering Polymer Hydrogel Nanoparticles for Lymph Node-Targeted Delivery.* Angewandte Chemie International Edition, 2016. **55**(4): p. 1334-1339.

44. Rao, D.A., et al., *Biodegradable PLGA based nanoparticles for sustained regional lymphatic drug delivery.* Journal of pharmaceutical sciences, 2010. **99**(4): p. 2018-2031.

45. Zhuang, Y., et al., *PEGylated cationic liposomes robustly augment vaccine-induced immune responses: Role of lymphatic trafficking and biodistribution.* J Control Release, 2012. **159**(1): p. 135-42.

46. Zeng, Q., et al., *Cationic micelle delivery of Trp2 peptide for efficient lymphatic draining and enhanced cytotoxic T-lymphocyte responses.* Journal of Controlled Release, 2015. **200**: p. 1-12.

47. Roozendaal, R., R.E. Mebius, and G. Kraal.

48. Schudel, A., et al., *Programmable multistage drug delivery to lymph nodes.* Nature Nanotechnology, 2020. **15**(6): p. 491-499.

49. Kim, J., P.A. Archer, and S.N. Thomas, *Innovations in lymph node targeting nanocarriers.* Seminars in Immunology, 2021. **56**: p. 101534.

50. Cooper, A.D., *Hepatic uptake of chylomicron remnants.* J Lipid Res, 1997. **38**(11): p. 2173-92.

51. Chaudhary, S., et al., *Recent approaches of lipid-based delivery system for lymphatic targeting via oral route.* J Drug Target, 2014. **22**(10): p. 871-82.

52. Trevaskis, N.L., L.M. Kaminskas, and C.J.H. Porter, *From sewer to saviour — targeting the lymphatic system to promote drug exposure and activity.* Nature Reviews Drug Discovery, 2015. **14**(11): p. 781-803.

53. Lee, G., et al., *Intestinal delivery in a long-chain fatty acid formulation enables lymphatic transport and systemic exposure of orlistat.* International Journal of Pharmaceutics, 2021. **596**: p. 120247.

54. Lee, G., et al., *Lymphatic Uptake of Liposomes after Intraperitoneal Administration Primarily Occurs via the Diaphragmatic Lymphatics and is Dependent on Liposome Surface Properties.* Molecular Pharmaceutics, 2019. **16**(12): p. 4987-4999.

55. Kochappan, R., et al., *Targeted delivery of mycophenolic acid to the mesenteric lymph node using a triglyceride mimetic prodrug approach enhances gut-specific immunomodulation in mice.* Journal of Controlled Release, 2021. **332**: p. 636-651.

56. Au - Trevaskis, N.L., et al., *The Mesenteric Lymph Duct Cannulated Rat Model: Application to the Assessment of Intestinal Lymphatic Drug Transport.* JoVE, 2015(97): p. e52389.

57. Gracia, G., et al., *High-Density Lipoprotein Composition Influences Lymphatic Transport after Subcutaneous Administration.* Molecular Pharmaceutics, 2020. **17**(8): p. 2938-2951.

58. Dahan, A., E.M. Zimmermann, and S. Ben-Shabat, *Modern prodrug design for targeted oral drug delivery.* Molecules (Basel, Switzerland), 2014. **19**(10): p. 16489-16505.

59. Mao, Y., et al., *Chylomicron-pretended nano-bio self-assembling vehicle to promote lymphatic transport and GALTs target of oral drugs.* Biomaterials, 2019. **188**: p. 173-186.

60. Kim, K.S., et al., *Oral Nanoparticles Exhibit Specific High-Efficiency Intestinal Uptake and Lymphatic Transport.* ACS nano, 2018. **12**(9): p. 8893-8900.

61. Kim, K.S., Y.S. Youn, and Y.H. Bae, *Immune-triggered cancer treatment by intestinal lymphatic delivery of docetaxel-loaded nanoparticle.* Journal of Controlled Release, 2019. **311-312**: p. 85-95.

62. Suzuki, K., K.S. Kim, and Y.H. Bae, *Long-term oral administration of Exendin-4 to control type 2 diabetes in a rat model.* Journal of controlled release : official journal of the Controlled Release Society, 2019. **294**: p. 259-267.

63. Baek, J.S. and C.W. Cho, *Surface modification of solid lipid nanoparticles for oral delivery of curcumin: Improvement of bioavailability through enhanced cellular uptake, and lymphatic uptake.* Eur J Pharm Biopharm, 2017. **117**: p. 132-140.

64. Nykänen, A.I., et al., *Targeting Lymphatic Vessel Activation and CCL21 Production by Vascular Endothelial Growth Factor Receptor-3 Inhibition Has Novel Immunomodulatory and Antiarteriosclerotic Effects in Cardiac Allografts.* Circulation, 2010. **121**(12): p. 1413-1422.

65. Kriehuber, E., et al., *Isolation and characterization of dermal lymphatic and blood endothelial cells reveal stable and functionally specialized cell lineages.* The Journal of experimental medicine, 2001. **194**(6): p. 797-808.

66. Hampton, H.R. and T. Chtanova, *Lymphatic Migration of Immune Cells.* Frontiers in immunology, 2019. **10**: p. 1168-1168.

67. Ivanov, S., et al., *CCR7 and IRF4-dependent dendritic cells regulate lymphatic collecting vessel permeability.* J Clin Invest, 2016. **126**(4): p. 1581-91.

68. Rigby, D.A., et al., *Neutrophils rapidly transit inflamed lymphatic vessel endothelium via integrin-dependent proteolysis and lipoxin-induced junctional retraction.* Journal of leukocyte biology, 2015. **98**(6): p. 897-912.

69. Tecchio, C., A. Micheletti, and M.A. Cassatella, *Neutrophil-derived cytokines: facts beyond expression.* Frontiers in immunology, 2014. **5**: p. 508.

70. Gorlino, C.V., et al., *Neutrophils exhibit differential requirements for homing molecules in their lymphatic and blood trafficking into draining lymph nodes.* The Journal of Immunology, 2014. **193**(4): p. 1966-1974.

71. Garnier, L., A.-O. Gkountidi, and S. Hugues, *Tumor-Associated Lymphatic Vessel Features and Immunomodulatory Functions.* Frontiers in Immunology, 2019. **10**.

72. Lukacs-Kornek, V., et al., *Regulated release of nitric oxide by nonhematopoietic stroma controls expansion of the activated T cell pool in lymph nodes.* Nature immunology, 2011. **12**(11): p. 1096-1104.

73. Tamburini, B.A., M.A. Burchill, and R.M. Kedl, *Antigen capture and archiving by lymphatic endothelial cells following vaccination or viral infection.* Nat Commun, 2014. **5**: p. 3989.

74. Witmer, A.N., et al., *VEGFR-3 in adult angiogenesis.* J Pathol, 2001. **195**(4): p. 490-7.

75. Brezovakova, V. and S. Jadhav, *Identification of Lyve-1 positive macrophages as resident cells in meninges of rats.* Journal of Comparative Neurology, 2020. **528**(12): p. 2021-2032.

76. Mouta Carreira, C., et al., *LYVE-1 is not restricted to the lymph vessels: expression in normal liver blood sinusoids and down-regulation in human liver cancer and cirrhosis.* Cancer Res, 2001. **61**(22): p. 8079-84.

77. Gordon, E.J., N.W. Gale, and N.L. Harvey, *Expression of the hyaluronan receptor LYVE-1 is not restricted to the lymphatic vasculature; LYVE-1 is also expressed on embryonic blood vessels.* Developmental Dynamics, 2008. **237**(7): p. 1901-1909.

78. Guo, Q., et al., *Mouse lymphatic endothelial cell targeted probes: anti-LYVE-1 antibody-based magnetic nanoparticles.* International journal of nanomedicine, 2013. **8**: p. 2273-2284.

79. Dashkevich, A., et al., *Ischemia-Reperfusion Injury Enhances Lymphatic Endothelial VEGFR3 and Rejection in Cardiac Allografts.* Am J Transplant, 2016. **16**(4): p. 1160-72.

80. Su, J.L., et al., *The role of the VEGF-C/VEGFR-3 axis in cancer progression.* British Journal of Cancer, 2007. **96**(4): p. 541-545.

81. Maisel, K., et al., *Pro-lymphangiogenic VEGFR-3 signaling modulates memory T cell responses in allergic airway inflammation.* Mucosal Immunology, 2021. **14**(1): p. 144-151.

82. Yeh, Y.-W., et al., *Targeting the VEGF-C/VEGFR3 axis suppresses Slug-mediated cancer metastasis and stemness via inhibition of KRAS/YAP1 signaling.* Oncotarget, 2017. **8**(3): p. 5603-5618.

83. Fankhauser, M., et al., *Tumor lymphangiogenesis promotes T cell infiltration and potentiates immunotherapy in melanoma.* Sci Transl Med, 2017. **9**(407).

84. Wiig, H. and M.A. Swartz, *Interstitial fluid and lymph formation and transport: physiological regulation and roles in inflammation and cancer.* Physiol Rev, 2012. **92**(3): p. 1005-60.

85. Manolova, V., et al., *Nanoparticles target distinct dendritic cell populations according to their size.* European Journal of Immunology, 2008. **38**(5): p. 1404-1413.

86. Moghimi, S.M., A.C. Hunter, and J.C. Murray, *Long-circulating and target-specific nanoparticles: theory to practice.* Pharmacol Rev, 2001. **53**(2): p. 283-318.

87. Jung Soo Suk and Qingguo Xu and Namho Kim and Justin Hanes and Laura, M.E., *PEGylation as a strategy for improving nanoparticle-based drug and gene delivery.* Advanced Drug Delivery Reviews, 2016. **99**: p. 28-51.

88. Alexis, F., et al., *Factors affecting the clearance and biodistribution of polymeric nanoparticles.* Mol Pharm, 2008. **5**(4): p. 505-15.

89. Gessner, A., et al., *Nanoparticles with decreasing surface hydrophobicities: influence on plasma protein adsorption.* Int J Pharm, 2000. **196**(2): p. 245-9.

90. Walkey, C.D., et al., *Nanoparticle size and surface chemistry determine serum protein adsorption and macrophage uptake.* J Am Chem Soc, 2012. **134**(4): p. 2139-47.

91. Otsuka, H., Y. Nagasaki, and K. Kataoka, *PEGylated nanoparticles for biological and pharmaceutical applications.* Advanced Drug Delivery Reviews, 2003. **55**(3): p. 403-419.

92. Jokerst, J.V., et al., *Nanoparticle PEGylation for imaging and therapy.* Nanomedicine (London, England), 2011. **6**(4): p. 715-728.

93. Xu, Q., et al., *Impact of Surface Polyethylene Glycol (PEG) Density on Biodegradable Nanoparticle Transport in Mucus ex Vivo and Distribution in Vivo.* ACS nano, 2015. **9**(9): p. 9217-9227.

94. Xu, Q., et al., *Scalable method to produce biodegradable nanoparticles that rapidly penetrate human mucus.* J Control Release, 2013. **170**(2): p. 279-86.

95. Nance, E.A., et al., *A dense poly(ethylene glycol) coating improves penetration of large polymeric nanoparticles within brain tissue.* Science translational medicine, 2012. **4**(149): p. 149ra119-149ra119.

96. Dancy, J.G., et al., *Non-specific binding and steric hindrance thresholds for penetration of particulate drug carriers within tumor tissue.* Journal of controlled release : official journal of the Controlled Release Society, 2016. **238**: p. 139-148.

97. Kelley, W.J., et al., *PEGylation of model drug carriers enhances phagocytosis by primary human neutrophils.* Acta biomaterialia, 2018. **79**: p. 283-293.

98. Shameli, K., et al., *Synthesis and Characterization of Polyethylene Glycol Mediated Silver Nanoparticles by the Green Method.* International Journal of Molecular Sciences, 2012. **13**(6).

99. Wu, H., et al., *Synthesis and characterization of cellulose nanocrystal-graft-poly(d-lactide) and its nanocomposite with poly(l-lactide).* Polymer, 2016. **103**: p. 365-375.

100. Hirosue, S., et al., *Steady-state antigen scavenging, cross-presentation, and CD8+ T cell priming: a new role for lymphatic endothelial cells.* J Immunol, 2014. **192**(11): p. 5002-11.

101. Xu, Q., et al., *Impact of Surface Polyethylene Glycol (PEG) Density on Biodegradable Nanoparticle Transport in Mucus ex Vivo and Distribution in Vivo.* ACS Nano, 2015. **9**(9): p. 9217-27.

102. Kou, L., et al., *The endocytosis and intracellular fate of nanomedicines: Implication for rational design.* Asian Journal of Pharmaceutical Sciences, 2013. **8**(1): p. 1-10.

103. Guo, P., et al., *ICAM-1-Targeted, Lcn2 siRNA-Encapsulating Liposomes are Potent Anti-angiogenic Agents for Triple Negative Breast Cancer.* Theranostics, 2016. **6**(1): p. 1-13.

104. Sari, E., et al., *ICAM-1 targeted catalase encapsulated PLGA-b-PEG nanoparticles against vascular oxidative stress.* J Microencapsul, 2015. **32**(7): p. 687-98.

105. Del Amo, L., et al., *Surface Functionalization of PLGA Nanoparticles to Increase Transport across the BBB for Alzheimer's Disease.* Applied Sciences, 2021. **11**(9).

106. Lin, Q., P. Fathi, and X. Chen, *Nanoparticle delivery in vivo: A fresh look from intravital imaging.* EBioMedicine, 2020. **59**.

107. Tehrani, S.F., et al., *Length of surface PEG modulates nanocarrier transcytosis across brain vascular endothelial cells.* Nanomedicine: Nanotechnology, Biology and Medicine, 2019. **16**: p. 185-194.

108. Rabanel, J.-M., et al., *Transport of PEGylated-PLA nanoparticles across a blood brain barrier model, entry into neuronal cells and in vivo brain bioavailability.* Journal of Controlled Release, 2020. **328**: p. 679-695.

109. Kim, M., et al., *Engineered ionizable lipid nanoparticles for targeted delivery of RNA therapeutics into different types of cells in the liver.* Sci Adv, 2021. **7**(9).

110. Williams, R.M., et al., *Mesoscale Nanoparticles Selectively Target the Renal Proximal Tubule Epithelium.* Nano Letters, 2015. **15**(4): p. 2358-2364.

111. Zhou, H., et al., *Dense and Dynamic Polyethylene Glycol Shells Cloak Nanoparticles from Uptake by Liver Endothelial Cells for Long Blood Circulation.* ACS nano, 2018. **12**(10): p. 10130-10141.

112. Du, X.J., et al., *Regulating the surface poly(ethylene glycol) density of polymeric nanoparticles and evaluating its role in drug delivery in vivo.* Biomaterials, 2015. **69**: p. 1-11.

113. Li, Y., M. Kröger, and W.K. Liu, *Endocytosis of PEGylated nanoparticles accompanied by structural and free energy changes of the grafted polyethylene glycol.* Biomaterials, 2014. **35**(30): p. 8467-8478.

114. Li, M., et al., *Brush Conformation of Polyethylene Glycol Determines the Stealth Effect of Nanocarriers in the Low Protein Adsorption Regime.* Nano Letters, 2021. **21**(4): p. 1591-1598.

115. Perry, J.L., et al., *PEGylated PRINT nanoparticles: the impact of PEG density on protein binding, macrophage association, biodistribution, and pharmacokinetics.* Nano Lett, 2012. **12**(10): p. 5304-10.

116. Yang, Q., et al., *Evading Immune Cell Uptake and Clearance Requires PEG Grafting at Densities Substantially Exceeding the Minimum for Brush Conformation.* Molecular Pharmaceutics, 2014. **11**(4): p. 1250-1258.

117. Ait Bachir, Z., et al., *Effects of PEG surface density and chain length on the pharmacokinetics and biodistribution of methotrexate-loaded chitosan nanoparticles.* Int J Nanomedicine, 2018. **13**: p. 5657-5671.

118. Pozzi, D., et al., *Effect of polyethyleneglycol (PEG) chain length on the bio-nano-interactions between PEGylated lipid nanoparticles and biological fluids: from nanostructure to uptake in cancer cells.* Nanoscale, 2014. **6**(5): p. 2782-92.

119. Sims, L.B., et al., *Enhanced uptake and transport of PLGA-modified nanoparticles in cervical cancer.* Journal of nanobiotechnology, 2016. **14**: p. 33-33.

120. Aguilera, G., et al., *Carboxymethyl cellulose coated magnetic nanoparticles transport across a human lung microvascular endothelial cell model of the blood–brain barrier.* Nanoscale Advances, 2019. **1**(2): p. 671-685.

121. Ahn, S.I., et al., *Microengineered human blood–brain barrier platform for understanding nanoparticle transport mechanisms.* Nature Communications, 2020. **11**(1): p. 175.

122. Chattopadhyay, N., et al., *Solid lipid nanoparticles enhance the delivery of the HIV protease inhibitor, atazanavir, by a human brain endothelial cell line.* Pharm Res, 2008. **25**(10): p. 2262-71.

123. Francia, V., A. Aliyandi, and A. Salvati, *Effect of the development of a cell barrier on nanoparticle uptake in endothelial cells.* Nanoscale, 2018. **10**(35): p. 16645-16656.

124. Kim, H.R., et al., *Low-density lipoprotein receptor-mediated endocytosis of PEGylated nanoparticles in rat brain endothelial cells.* Cell Mol Life Sci, 2007. **64**(3): p. 356-64.

125. Moghimi, S.M. and D. Simberg, *Nanoparticle transport pathways into tumors.* Journal of Nanoparticle Research, 2018. **20**(6): p. 169.

126. Skotland, T. and K. Sandvig, *Transport of nanoparticles across the endothelial cell layer.* Nano Today, 2021. **36**: p. 101029.

127. Kreuter, J., *Mechanism of polymeric nanoparticle-based drug transport across the blood-brain barrier (BBB).* J Microencapsul, 2013. **30**(1): p. 49-54.

128. Wang, Z., et al., *Size and Dynamics of Caveolae Studied Using Nanoparticles in Living Endothelial Cells.* ACS Nano, 2009. **3**(12): p. 4110-4116.

129. Wang, Z., et al., *Delivery of nanoparticle: complexed drugs across the vascular endothelial barrier via caveolae.* IUBMB Life, 2011. **63**(8): p. 659-67.

130. Ye, D., et al., *Nanoparticle accumulation and transcytosis in brain endothelial cell layers.* Nanoscale, 2013. **5**(22): p. 11153-11165.

131. Thorne, R.G. and C. Nicholson, *In vivo diffusion analysis with quantum dots and dextrans predicts the width of brain extracellular space.* Proceedings of the National Academy of Sciences, 2006. **103**(14): p. 5567.

132. Stylianopoulos, T., et al., *Diffusion of particles in the extracellular matrix: the effect of repulsive electrostatic interactions.* Biophysical journal, 2010. **99**(5): p. 1342-1349.

133. Lieleg, O., R.M. Baumgärtel, and A.R. Bausch, *Selective filtering of particles by the extracellular matrix: an electrostatic bandpass.* Biophysical journal, 2009. **97**(6): p. 1569-1577.

134. Le Goas, M., et al., *How Do Surface Properties of Nanoparticles Influence Their Diffusion in the Extracellular Matrix? A Model Study in Matrigel Using Polymer-Grafted Nanoparticles.* Langmuir, 2020. **36**(35): p. 10460-10470.

135. Hansing, J., et al., *Nanoparticle filtering in charged hydrogels: Effects of particle size, charge asymmetry and salt concentration.* The European Physical Journal E, 2016. **39**(5): p. 53.

136. Mattix, B., et al., *EFFECTS OF POLYMERIC NANOPARTICLE SURFACE PROPERTIES ON INTERACTION WITH BRAIN TUMOR ENVIRONMENT.* Nano LIFE, 2013. **3**(4): p. 1343003-1343003.

137. Tomasetti, L., et al., *Influence of PEGylation on nanoparticle mobility in different models of the extracellular matrix.* Eur J Pharm Biopharm, 2016. **108**: p. 145-155.

138. Labouta, H.I., et al., *Surface-grafted polyethylene glycol conformation impacts the transport of PEG-functionalized liposomes through a tumour extracellular matrix model.* RSC Advances, 2018. **8**(14): p. 7697-7708.

139. Mdzinarashvili, T., et al., *Stability of drug delivery PLGA nanoparticles: Calorimertric approach.* Drug Delivery, 2011: p. 189-205.

140. Mudshinge, S.R., et al., *Nanoparticles: Emerging carriers for drug delivery.* Saudi Pharm J, 2011. **19**(3): p. 129-41.

141. Friedman, A.D., S.E. Claypool, and R. Liu, *The smart targeting of nanoparticles.* Curr Pharm Des, 2013. **19**(35): p. 6315-29.

142. Kamaly, N., et al., *Degradable Controlled-Release Polymers and Polymeric Nanoparticles: Mechanisms of Controlling Drug Release.* Chemical Reviews, 2016. **116**(4): p. 2602-2663.

143. Ghaffarian, R. and S. Muro, *Models and methods to evaluate transport of drug delivery systems across cellular barriers.* J Vis Exp, 2013(80): p. e50638.

144. Triacca, V., et al., *Transcellular Pathways in Lymphatic Endothelial Cells Regulate Changes in Solute Transport by Fluid Stress.* Circ Res, 2017. **120**(9): p. 1440-1452.

145. McCright, J., et al., *Nanoparticles with dense poly(ethylene glycol) coatings with near neutral charge are maximally transported across lymphatics and to the lymph nodes.* Acta Biomaterialia, 2022. **145**: p. 146-158.

146. Tian, F., et al., *Computer simulation studies on the interactions between nanoparticles and cell membrane.* Science China Chemistry, 2014. **57**(12): p. 1662-1671.

147. Lin, X., Y. Li, and G. Ning, *Nanoparticle's Size Effect on Its Translocation Across a Lipid Bilayer: A Molecular Dynamics Simulation.* Journal of Computational and Theoretical Nanoscience, 2010. **7**: p. 269-276.

148. Jayasinghe, M.K., et al., *The Role of in silico Research in Developing Nanoparticle-Based Therapeutics.* Front Digit Health, 2022. **4**: p. 838590.

149. Liu, Y., S. Shah, and J. Tan, *Computational Modeling of Nanoparticle Targeted Drug Delivery.* Reviews in Nanoscience and Nanotechnology, 2012. **1**: p. 66-83.

150. Ramezanpour, M., et al., *Computational and experimental approaches for investigating nanoparticle-based drug delivery systems.* Biochimica et Biophysica Acta (BBA) - Biomembranes, 2016. **1858**(7, Part B): p. 1688-1709.

151. Groh, C.M., et al., *Mathematical and computational models of drug transport in tumours.* Journal of The Royal Society Interface, 2014. **11**(94): p. 20131173.

152. Khan, A.I., et al., *Quantification of kinetic rate constants for transcytosis of polymeric nanoparticle through blood-brain barrier.* Biochimica et Biophysica Acta (BBA) - General Subjects, 2018. **1862**(12): p. 2779-2787.

153. McCright, J., et al., *Nanoparticles with dense poly(ethylene glycol) coatings with near neutral charge are maximally transported across lymphatics and to the lymph nodes.* Acta Biomater, 2022.

154. Levenberg, K., *A method for the solution of certain non-linear problems in least squares.* Quarterly of Applied Mathematics, 1944. **2**(2): p. 164-168.

155. Saqlain, M., et al., *Investigating Stochastic Differential Equations Modelling for Levodopa Infusion in Patients with Parkinson's Disease.* Eur J Drug Metab Pharmacokinet, 2020. **45**(1): p. 41-49.

156. Chou, W.-C. and Z. Lin, *Machine learning and artificial intelligence in physiologically based pharmacokinetic modeling.* Toxicological Sciences, 2023. **191**(1): p. 1-14.

157. Lu, J., et al., *Neural-ODE for pharmacokinetics modeling and its advantage to alternative machine learning models in predicting new dosing regimens.* iScience, 2021. **24**(7): p. 102804.

158. Cattaneo, L. and P. Zunino, *A computational model of drug delivery through microcirculation to compare different tumor treatments.* Int J Numer Method Biomed Eng, 2014. **30**(11): p. 1347-71.

159. Chou, W.-C., et al., *Development of a multi-route physiologically based pharmacokinetic (PBPK) model for nanomaterials: a comparison between a traditional versus a new route-specific approach using gold nanoparticles in rats.* Particle and Fibre Toxicology, 2022. **19**(1): p. 47.

160. Georgieva, J.V., et al., *Surface Characteristics of Nanoparticles Determine Their Intracellular Fate in and Processing by Human Blood–Brain Barrier Endothelial Cells In Vitro.* Molecular Therapy, 2011. **19**(2): p. 318-325.

161. Fiorentino, I., et al., *Energy independent uptake and release of polystyrene nanoparticles in primary mammalian cell cultures.* Experimental Cell Research, 2015. **330**(2): p. 240-247.

162. Firdessa, R., T.A. Oelschlaeger, and H. Moll, *Identification of multiple cellular uptake pathways of polystyrene nanoparticles and factors affecting the uptake: Relevance for drug delivery systems.* European Journal of Cell Biology, 2014. **93**(8): p. 323-337.

163. Fazlollahi, F., et al., *Polystyrene nanoparticle trafficking across MDCK-II.* Nanomedicine: Nanotechnology, Biology and Medicine, 2011. **7**(5): p. 588-594.

164. Yacobi, N.R., et al., *Mechanisms of Alveolar Epithelial Translocation of a Defined Population of Nanoparticles.* American Journal of Respiratory Cell and Molecular Biology, 2010. **42**(5): p. 604-614.

165. Rappoport, J., et al., *Cellular entry of nanoparticles via serum sensitive clathrin-mediated endocytosis, and plasma membrane permeabilization.* International Journal of Nanomedicine, 2012: p. 2045.

166. Partikel, K., et al., *Effect of nanoparticle size and PEGylation on the protein corona of PLGA nanoparticles.* European Journal of Pharmaceutics and Biopharmaceutics, 2019. **141**: p. 70-80.

167. Peng, Q., et al., *Digestive enzyme corona formed in the gastrointestinal tract and its impact on epithelial cell uptake of nanoparticles.* Biomacromolecules, 2019. **20**(4): p. 1789-1797.

168. Lesniak, A., et al., *Nanoparticle adhesion to the cell membrane and its effect on nanoparticle uptake efficiency.* Journal of the American Chemical Society, 2013. **135**(4): p. 1438-1444.

169. Liu, H., et al., *Structure-based programming of lymph-node targeting in molecular vaccines.* Nature, 2014. **507**(7493): p. 519-522.

170. Abdallah, M., et al., *Lymphatic targeting by albumin-hitchhiking: Applications and optimisation.* Journal of Controlled Release, 2020. **327**: p. 117-128.

171. Wang, Y., et al., *Shape-Controlled Paclitaxel Nanoparticles with Multiple Morphologies: Rod-Shaped, Worm-Like, Spherical, and Fingerprint-Like.* Molecular Pharmaceutics, 2014. **11**(10): p. 3766-3771.

172. Geng, Y., et al., *Shape effects of filaments versus spherical particles in flow and drug delivery.* Nature Nanotechnology, 2007. **2**(4): p. 249-255.

173. Dalhaimer, P., et al., *Targeted Worm Micelles.* Biomacromolecules, 2004. **5**(5): p. 1714-1719.

174. Christian, D.A., et al., *Flexible filaments for in vivo imaging and delivery: persistent circulation of filomicelles opens the dosage window for sustained tumor shrinkage.* Molecular pharmaceutics, 2009. **6**(5): p. 1343-1352.

175. Simone, E.A., T.D. Dziubla, and V.R. Muzykantov, *Polymeric carriers: role of geometry in drug delivery.* Expert Opinion on Drug Delivery, 2008. **5**(12): p. 1283-1300.

176. Lee, B.J., et al., *Shaping nanoparticle diffusion through biological barriers to drug delivery.* JCIS Open, 2021. **4**: p. 100025.

177. Lee, K.L., et al., *Shape matters: the diffusion rates of TMV rods and CPMV icosahedrons in a spheroid model of extracellular matrix are distinct.* Biomaterials science, 2013. **1**(6): p. 581-588.

178. Yu, M., et al., *Rotation-facilitated rapid transport of nanorods in mucosal tissues.* Nano letters, 2016. **16**(11): p. 7176-7182.

179. Zhao, Y., et al., *A comparison between sphere and rod nanoparticles regarding their in vivo biological behavior and pharmacokinetics.* Scientific reports, 2017. **7**(1): p. 1-11.

180. Champion, J.A., Y.K. Katare, and S. Mitragotri, *Making polymeric micro- and nanoparticles of complex shapes.* Proceedings of the National Academy of Sciences, 2007. **104**(29): p. 11901.

181. Champion, J.A., Y.K. Katare, and S. Mitragotri, *Making polymeric micro-and nanoparticles of complex shapes.* Proceedings of the National Academy of Sciences, 2007. **104**(29): p. 11901-11904.

182. Salamon, P., et al., *Rheological and flow birefringence studies of rod-shaped pigment nanoparticle dispersions.* Journal of Molecular Liquids, 2020. **313**: p. 113401.

183. Wang, J., et al., *Diffusion of rod-like nanoparticles in non-adhesive and adhesive porous polymeric gels.* Journal of the Mechanics and Physics of Solids, 2018. **112**: p. 431-457.

184. Liu, X., et al., *Size Dependent Cellular Uptake of Rod-like Bionanoparticles with Different Aspect Ratios.* Scientific Reports, 2016. **6**(1): p. 24567.

185. Xie, X., et al., *The Effect of shape on Cellular Uptake of Gold Nanoparticles in the forms of Stars, Rods, and Triangles.* Scientific Reports, 2017. **7**(1): p. 3827.

186. Xu, Z.P., et al., *Subcellular compartment targeting of layered double hydroxide nanoparticles.* Journal of Controlled Release, 2008. **130**(1): p. 86-94.

187. Dasgupta, S., T. Auth, and G. Gompper, *Shape and orientation matter for the cellular uptake of nonspherical particles.* Nano letters, 2014. **14**(2): p. 687-693.

188. Seneca, S., et al., *How low can you go? low densities of Poly (ethylene glycol) surfactants attract stealth proteins.* Macromolecular Bioscience, 2018. **18**(9): p. 1800075.

189. Abstiens, K., et al., *Interaction of functionalized nanoparticles with serum proteins and its impact on colloidal stability and cargo leaching.* Soft Matter, 2019. **15**(4): p. 709-720.

190. Rakhra, K., et al., *Exploiting albumin as a mucosal vaccine chaperone for robust generation of lung-resident memory T cells.* Science immunology, 2021. **6**(57): p. eabd8003.

191. Summers, B.D., et al., *Lung lymphatic thrombosis and dysfunction caused by cigarette smoke exposure precedes emphysema in mice.* Scientific Reports, 2022. **12**(1): p. 5012.

192. Cornick, S., A. Tawiah, and K. Chadee, *Roles and regulation of the mucus barrier in the gut.* Tissue barriers, 2015. **3**(1-2): p. e982426-e982426.

193. Bansil, R. and B.S. Turner, *The biology of mucus: Composition, synthesis and organization.* Advanced drug delivery reviews, 2018. **124**: p. 3-15.

194. Johansson, M.E., et al., *The inner of the two Muc2 mucin-dependent mucus layers in colon is devoid of bacteria.* Proceedings of the national academy of sciences, 2008. **105**(39): p. 15064-15069.

195. Johansson, M.E. and G.C. Hansson, *Immunological aspects of intestinal mucus and mucins.* Nature Reviews Immunology, 2016. **16**(10): p. 639-649.

196. Leal, J., H.D.C. Smyth, and D. Ghosh, *Physicochemical properties of mucus and their impact on transmucosal drug delivery.* International journal of pharmaceutics, 2017. **532**(1): p. 555-572.

197. Forstner, J., *Intestinal mucins in health and disease.* Digestion, 1978. **17**(3): p. 234-263.

198. Cone, R.A., *Barrier properties of mucus.* Advanced Drug Delivery Reviews, 2009. **61**(2): p. 75-85.

199. Hansson, G.C., *Mucins and the microbiome.* Annual review of biochemistry, 2020. **89**: p. 769-793.

200. Paone, P. and P.D. Cani, *Mucus barrier, mucins and gut microbiota: the expected slimy partners?* Gut, 2020. **69**(12): p. 2232.

201. Engle, M.J., G.S. Goetz, and D.H. Alpers, *Caco-2 cells express a combination of colonocyte and enterocyte phenotypes.* J Cell Physiol, 1998. **174**(3): p. 362-9.

202. Artursson, P. and J. Karlsson, *Correlation between oral drug absorption in humans and apparent drug permeability coefficients in human intestinal epithelial (Caco-2) cells.* Biochem Biophys Res Commun, 1991. **175**(3): p. 880-5.

203. Artursson, P., K. Palm, and K. Luthman, *Caco-2 monolayers in experimental and theoretical predictions of drug transport.* Adv Drug Deliv Rev, 2001. **46**(1-3): p. 27-43.

204. Gupta, V., N. Doshi, and S. Mitragotri, *Permeation of insulin, calcitonin and exenatide across Caco-2 monolayers: measurement using a rapid, 3-day system.* PloS one, 2013. **8**(2): p. e57136-e57136.

205. Lea, T., *Caco-2 Cell Line*, in *The Impact of Food Bioactives on Health: in vitro and ex vivo models*, K. Verhoeckx, et al., Editors. 2015, Springer International Publishing: Cham. p. 103-111.

206. Briske-Anderson, M.J., J.W. Finley, and S.M. Newman, *The influence of culture time and passage number on the morphological and physiological development of Caco-2 cells.* Proc Soc Exp Biol Med, 1997. **214**(3): p. 248-57.

207. Yee, S., *In vitro permeability across Caco-2 cells (colonic) can predict in vivo (small intestinal) absorption in man--fact or myth.* Pharm Res, 1997. **14**(6): p. 763-6.

208. Wu, S., et al., *Effects of polystyrene microbeads on cytotoxicity and transcriptomic profiles in human Caco-2 cells.* Environ Toxicol, 2020. **35**(4): p. 495-506.

209. Camilleri, M., *Leaky gut: mechanisms, measurement and clinical implications in humans.* Gut, 2019. **68**(8): p. 1516-1526.

210. Pontier, C., et al., *HT29-MTX and Caco-2/TC7 monolayers as predictive models for human intestinal absorption: role of the mucus layer.* J Pharm Sci, 2001. **90**(10): p. 1608-19.

211. Ferraretto, A., et al., *Morphofunctional properties of a differentiated Caco2/HT-29 co-culture as an in vitro model of human intestinal epithelium.* Biosci Rep, 2018. **38**(2).

212. Atuma, C., et al., *The adherent gastrointestinal mucus gel layer: thickness and physical state in vivo.* American journal of physiology. Gastrointestinal and liver physiology, 2001. **280**(5): p. G922-G929.

213. Johansson, M.E.V., J.M.H. Larsson, and G.C. Hansson, *The two mucus layers of colon are organized by the MUC2 mucin, whereas the outer layer is a legislator of host–microbial interactions.* Proceedings of the National Academy of Sciences, 2011. **108**(Supplement 1): p. 4659.

214. Mahler, G.J., M.L. Shuler, and R.P. Glahn, *Characterization of Caco-2 and HT29-MTX cocultures in an in vitro digestion/cell culture model used to predict iron bioavailability.* J Nutr Biochem, 2009. **20**(7): p. 494-502.

215. Atuma, C., et al., *The adherent gastrointestinal mucus gel layer: thickness and physical state in vivo.* American Journal of Physiology-Gastrointestinal and Liver Physiology, 2001. **280**(5): p. G922-G929.

216. Camilleri, M., *Leaky gut: mechanisms, measurement and clinical implications in humans.* Gut, 2019. **68**(8): p. 1516.

217. Engevik, A.C., *Using Microfluidics to Model Mucus.* Cellular and Molecular Gastroenterology and Hepatology, 2020. **9**(3): p. 551-552.

218. Cone, R.A., *Chapter 4 - Mucus*, in *Mucosal Immunology (Third Edition)*, J. Mestecky, et al., Editors. 2005, Academic Press: Burlington. p. 49-72.

219. Howard, R.L., et al., *Biochemical and rheological analysis of human colonic culture mucus reveals similarity to gut mucus.* Biophysical Journal, 2021. **120**(23): p. 5384-5394.

220. Mason, T.G., *Estimating the viscoelastic moduli of complex fluids using the generalized Stokes–Einstein equation.* Rheologica acta, 2000. **39**(4): p. 371-378.

221. Hill, D.B., et al., *A biophysical basis for mucus solids concentration as a candidate biomarker for airways disease.* PloS one, 2014. **9**(2): p. e87681.

222. Duncan, G.A., et al., *Microstructural alterations of sputum in cystic fibrosis lung disease.* JCI Insight, 2016. **1**(18).

223. Ensign, L.M., et al., *Ex vivo characterization of particle transport in mucus secretions coating freshly excised mucosal tissues.* Mol Pharm, 2013. **10**(6): p. 2176-82.

224. Maisel, K., et al., *Nanoparticles coated with high molecular weight PEG penetrate mucus and provide uniform vaginal and colorectal distribution in vivo.* Nanomedicine (London, England), 2016. **11**(11): p. 1337-1343.

225. Lai, S.K., Y.-Y. Wang, and J. Hanes, *Mucus-penetrating nanoparticles for drug and gene delivery to mucosal tissues.* Advanced Drug Delivery Reviews, 2009. **61**(2): p. 158-171.

226. Crocker, J.C. and D.G. Grier, *Methods of digital video microscopy for colloidal studies.* Journal of colloid and interface science, 1996. **179**(1): p. 298-310.

227. Duncan, G.A., et al., *Microstructural alterations of sputum in cystic fibrosis lung disease.* JCI insight, 2016. **1**(18): p. e88198-e88198.

228. Mason, T.G. and D.A. Weitz, *Optical measurements of frequency-dependent linear viscoelastic moduli of complex fluids.* Physical review letters, 1995. **74**(7): p. 1250.

229. Karam, S.M., *Lineage commitment and maturation of epithelial cells in the gut.* Front Biosci, 1999. **4**: p. D286-98.

230. Aksoy, N., A. Corfield, and J. Sheehan, *Preliminary study pointing out a significant alteration in the biochemical composition of MUC2 in colorectal mucinous carcinoma.* Clinical biochemistry, 2000. **33**: p. 167-73.

231. Lock, J.Y., T.L. Carlson, and R.L. Carrier, *Mucus models to evaluate the diffusion of drugs and particles.* Adv Drug Deliv Rev, 2018. **124**: p. 34-49.

232. Lock, J., et al., *Acute Exposure to Commonly Ingested Emulsifiers Alters Intestinal Mucus Structure and Transport Properties.* Scientific Reports, 2018. **8**.

233. Pan, F., et al., *Optimization of Caco-2 and HT29 co-culture in vitro cell models for permeability studies.* Int J Food Sci Nutr, 2015. **66**(6): p. 680-5.

234. Srinivasan, B., et al., *TEER measurement techniques for in vitro barrier model systems.* Journal of laboratory automation, 2015. **20**(2): p. 107-126.

235. Chen, X.M., I. Elisia, and D.D. Kitts, *Defining conditions for the co-culture of Caco-2 and HT29-MTX cells using Taguchi design.* J Pharmacol Toxicol Methods, 2010. **61**(3): p. 334-42.

236. Gagnon, M., et al., *Comparison of the Caco-2, HT-29 and the mucus-secreting HT29-MTX intestinal cell models to investigate Salmonella adhesion and invasion.* J Microbiol Methods, 2013. **94**(3): p. 274-9.

237. Navabi, N., M.A. McGuckin, and S.K. Lindén, *Gastrointestinal cell lines form polarized epithelia with an adherent mucus layer when cultured in semi-wet interfaces with mechanical stimulation.* PLoS One, 2013. **8**(7): p. e68761.

238. Georgiades, P., et al., *Particle tracking microrheology of purified gastrointestinal mucins.* Biopolymers, 2014. **101**(4): p. 366-377.

239. Yildiz, H.M., et al., *Size selectivity of intestinal mucus to diffusing particulates is dependent on surface chemistry and exposure to lipids.* Journal of drug targeting, 2015. **23**(7-8): p. 768-774.

240. Krupa, L., et al., *Comparing the permeability of human and porcine small intestinal mucus for particle transport studies.* Scientific Reports, 2020. **10**(1): p. 20290.

241. Bajka, B.H., et al., *The influence of small intestinal mucus structure on particle transport ex vivo.* Colloids and Surfaces B: Biointerfaces, 2015. **135**: p. 73-80.

242. Ermund, A., et al., *Mucus properties and goblet cell quantification in mouse, rat and human ileal Peyer's patches.* PloS one, 2013. **8**(12): p. e83688.

243. Lai, S.K., et al., *Micro- and macrorheology of mucus.* Advanced drug delivery reviews, 2009. **61**(2): p. 86-100.

244. Macierzanka, A., A.R. Mackie, and L. Krupa, *Permeability of the small intestinal mucus for physiologically relevant studies: Impact of mucus location and ex vivo treatment.* Scientific Reports, 2019. **9**(1): p. 17516.

245. Swidsinski, A., et al., *Reduced Mass and Diversity of the Colonic Microbiome in Patients with Multiple Sclerosis and Their Improvement with Ketogenic Diet.* Frontiers in Microbiology, 2017. **8**.

246. Araújo, F. and B. Sarmento, *Towards the characterization of an in vitro triple co-culture intestine cell model for permeability studies.* Int J Pharm, 2013. **458**(1): p. 128-34.

247. Lozoya-Agullo, I., et al., *Usefulness of Caco-2/HT29-MTX and Caco-2/HT29-MTX/Raji B Coculture Models To Predict Intestinal and Colonic Permeability Compared to Caco-2 Monoculture.* Mol Pharm, 2017. **14**(4): p. 1264-1270.

248. Ude, V.C., et al., *Using 3D gastrointestinal tract in vitro models with microfold cells and mucus secreting ability to assess the hazard of copper oxide nanomaterials.* Journal of Nanobiotechnology, 2019. **17**(1): p. 70.

249. Kernéis, S., et al., *Conversion by Peyer's Patch Lymphocytes of Human Enterocytes into M Cells that Transport Bacteria.* Science, 1997. **277**(5328): p. 949-952.

250. Beterams, A., et al., *Versatile human in vitro triple coculture model coincubated with adhered gut microbes reproducibly mimics pro-inflammatory host-microbe interactions in the colon.* The FASEB Journal, 2021. **35**(12): p. e21992.